

From solution to device: processing approaches to boost the photovoltaic performance of organic solar cells

By

Adrian Velazquez Osorio

A thesis submitted in partial fulfillment of the requirements for the degree of

Master of Science

Department of Chemistry

University of Alberta

© Adrian Velazquez Osorio, 2021

Abstract

The world's growing energy consumption and increasingly visible effects of climate change originated in continued dependence on fossil fuels has strengthened the push to develop cleaner and renewable sources of energy. Solar photovoltaic cells are at the forefront of an ongoing energy transition and a new generation of solar technology based on organic semiconductor materials – organic solar cells – is capturing the attention of researchers because of their unique properties.

Organic solar cells are photovoltaic devices that convert radiation into electricity using carbon-abundant materials. They can be manufactured to be flexible, semi-transparent, lightweight, and inexpensively produced on a large scale by roll-to-roll processes.

In this thesis work, a brief introduction on possible applications and operating principles of organic solar cells provides the background to the area. Chapter 1 describes the heart of the organic solar cell, the photoactive layer known as the bulk heterojunction, and the basics of the mechanisms behind photon harvesting via exciton generation, dissociation, and collection. The main photovoltaic metrics used to characterize these devices are also discussed.

Chapter 2 provides an overview of approaches used in the design of donor and acceptor materials and mentions how computer-driven optimization is emerging as an experimental paradigm to navigate the vast variable space involved in making the bulk heterojunction. The core section of this chapter focuses on approaches to improve solution processability of PM6:BTP-BO-4Cl OPV cells. Special emphasis is given to the application of methanol-based solvent annealing treatments and their role in inducing film dewetting of the PEDOT:PSS layer.

Chapter 3 continues this focus on optimization of the bulk heterojunction by discussing the application of microwave annealing of a ZR1:BTP-BO-4Cl composition. A brief critical overview on the application of microwave annealing to increase photovoltaic performance of organic solar cells is presented. Later, evaluation of different microwave annealing setups is examined.

Acknowledgements

One of the greatest privileges so far in my scientific career has been to work under the supervision of Dr. Jillian Buriak. I would like to express my deepest gratitude and appreciation for her mentorship, keen scientific feedback, encouragement, trust, and faith placed in me during my time in her lab. From her I learned that scientific research is more than instrumentation and chemical reactions - it has a human component - with live people putting their best effort and stepping out of their comfort zones to make our collective human experience better. I am grateful for the interest in my personal growth and career that Dr. Buriak has shown. By her example, I received an integral education that taught me what it means to be a great researcher.

I would also like to express my sincerest gratitude to my fellow Buriak research group members whose incredible talent and personality enriched me. I would like to extend special thanks to those colleagues who directly helped me to navigate this research project, Dr. Erik Lubber, Brian Olsen, and Tate Hauger for offering me their tremendous scientific insights and support in the experimental aspects of my work and to Aaron Kirkey and Dr. Bing Cao for being encyclopedias of knowledge and for teaching me the trade of making solar cells. Special thanks also go to Dr. Peter Kalisvaart, Jasper Woodard, Dr. Sayed Nagy, and Dr. Hao Wang for our conversations and friendship. A special thanks also goes to Kelli Lubber for her cheerful and invaluable help in navigating administrative and purchasing aspects of my project.

I would also like to gratefully acknowledge the Alberta Technical University of Munich International Graduate School for Hybrid Functional Materials program (ATUMS) and the Future Energy Systems for their generous funding. To the University of Alberta and the Chemistry Department – thank you for the amazing experiences you've given me and for the opportunities for personal growth.

Special thanks go to my good friend Brett Turner for our study sessions, scientific discussions, and for being a source of encouragement.

Finally, to my mother, thank you for cheering me on and for your unwavering support during these years of graduate work. You are a profound inspiration for my life and your example has been wind beneath my wings.

Contents

Abstract	ii
Acknowledgements	iii
List of tables	vi
List of figures.....	vii
List of abbreviations.....	xv
Chapter 1	
A brief introduction to organic photovoltaic solar cells (OPVs)	1
1.1 The global energy landscape and photovoltaic solar cell technology.....	1
1.2 Organic photovoltaic solar cells	4
1.3 Basic OPV theoretical concepts.....	5
1.3.1 Operating principles of OPVs and the bulk heterojunction	7
1.4 Photovoltaic metrics.....	11
Chapter 2	
The effect of solvent annealing on the PM6:BTP-BO-4Cl bulk heterojunction	15
2.1 A brief on optimization approaches for high efficiency OPV bulk heterojunctions	15
2.1.1 The design of high efficiency bulk heterojunctions.....	15
2.1.2 Post-deposition treatments to promote phase-segregation and solution processability of the bulk heterojunction	20
2.2 Chapter results overview	23
2.3 Approaches to improve reproducibility of PM6:BTP-BO-4Cl solar cells.....	24
2.4 Methanol treatment of the PM6:BTP-BO-4Cl bulk heterojunction	30
2.4.1 Application of methanol treatments to improve the PEDOT:PSS layer	43
Chapter 3	
Microwave annealing of OPV bulk heterojunctions.....	48

3.2	Chapter results overview	58
3.3	Rational optimization of a microwave annealing setup	58
3.3.1	Evaluation of different microwave annealing configurations	59
3.3.2	Type I configuration	64
3.3.3	Type II configuration	71
3.3.3	Type III configuration.....	72
3.4	Optimization of P3HT:PC ₆₁ BM organic photovoltaic solar cells	75
3.5	Type IV configuration.....	79
3.5.1	ZR1:BTP-BO:4Cl optimization.....	84
3.6	Chapter summary	95
3.7	Gallery of Infamy.....	96
	Materials section	97
	References	101

List of tables

Table 2-I: State of the art donor:acceptor compositions and corresponding photovoltaic metrics, reproduced with permission from Elsevier Science & Technology Journals [1]

Table 2-II: Effect of increased dissolution time and temperature on the performance of PM6:BTP-BO-4Cl solar cells

Table 2-III: Comparability of experimental results to those reported in the literature

Table 2-IV: Effect of PFN-Br/MeOH and MeOH treatment on thermally- treated and untreated PM6:BTP-BO-4Cl solar cells

Table 2-V: Effect of PFN-Br/MeOH soaking time on the performance of PM6:BTP-BO-4Cl solar cells

Table 2-VI: Atomic force micrographs of best performing PM6:BTP-BO-4Cl samples after subjected to thermal drying, soaking in PFN-Br/MeOH for 1 min, and soaking for 8 min.

Table 3-I: Individual device performance of a DRCN5T:IT-4F chip annealed using a Type I configuration

Table 3-II: Extended microwave annealing of P3HT:PC₆₁BM

Table 3-III: Reference controls for P3HT:PC₆₁BM solar cells

Table 3-IV: Performance evaluation for microwave-annealed P3HT:PC₆₁BM solar cells

Table 3-V: Performance evaluation for hotplate annealed P3HT:PC₆₁BM solar cells

Table 3-VI: Individual device performance of a ZR1:BTP-BO-4Cl solar cell MW-annealed for 15 s

Table 3-VII: Atomic force micrographs of unannealed, microwave-annealed, and hotplate-annealed ZR1:BTP-BO-4Cl OPV samples

Table 3-VIII: Individual device performance for an outlier ZR1:BTP-BO-4Cl batch

Table 3-IX: Averaged ZR1:BTP-BO-4Cl performance results as a function of annealing treatment

Table 3-X: Reference unannealed, microwaved, and hotplate annealed ZR1:BTP-BO-4Cl OPV cells with uncertainties

Table 3-XI: Maximum device performance achieved for the different reference treatments (ZR1:BTP-BO-4Cl OPV cells)

List of figures

Fig. 1.1: 2020 distribution of global primary energy consumption by source. Retrieved from OurWorldInData.org on October 2, 2021. CC-BY license [2].

Fig. 1.2: Map of solar irradiation on terrestrial Earth. Reprinted with permission from G2V Optics [2].

Fig. 1.3: Evolution of power conversion efficiency of different types of photovoltaic cells as published on the NREL website on October 8, 2021. This plot is courtesy of the National Renewable Energy Laboratory, Golden, CO. [3].

Fig. 1.4: a) Washable and flexible OPV solar cell for clothing integration, reproduced with permission from Springer Nature BV [4]. b) OPV solar overlays for building integration, reproduced with permission from John Wiley & Sons [5]. c) Roll-to-roll printing for mass deployment, reproduced with permission from Elsevier Science & Technology Journals [6].

Fig. 1.5: a) Layer schematic of a conventional architecture OPV chip containing 5 solar cells. b) A sample OPV chip manufactured in our group for research purposes.

Fig. 1.6: Different types of active layer geometries. Reproduced with permission from John Wiley & Sons [7].

Fig. 1.7: Schematic of the processes involved in converting radiation to electrical energy in the bulk heterojunction of an OPV cell. Reproduced with permission from Elsevier Science & Technology Journals [8].

Fig. 1.8) Schematic of the exciton dissociation processes from intermediate charge transfer states in the bulk heterojunction in an OPV cell. Reproduced with permission from Elsevier Science & Technology Journals [9].

Fig. 1.9: a) Representation of electron-hole pairs in organic molecular units. Reproduced with permission from Springer Nature BV [10].

Fig. 1.10: Flatband energy level diagram aligned at the vacuum level for different materials used in this thesis work. Values for HOMO and LUMO levels were obtained from the following references: ITO, PEDOT:PSS, and PFN-Br [11], PM6 and BTP-BO-4Cl [12], ZR1[13], Mg and Al [14].

- Fig. 1.11: a) Picture of a high-precision LED solar simulator manufactured by G2V Optics and b) solar spectral profile on earth. Reproduced with permission from G2V Optics [2].
- Fig. 1.12: a) Idealized characteristic J-V curve of an OPV cell. b) Equivalent photodiode circuit representation of an OPV cell. Abbreviation definitions: J_{sc} refers to short circuit current density; R_s to series resistance; R_{sh} to shunt resistance; V applied bias voltage, J current density. MP refers to a “maximum point”. Reproduced with permission from Royal Society of Chemistry [15].
- Fig. 2.1: Molecular structures, absorbance spectra, and energy levels of donor:acceptor compositions reported in state of the art OPV cells. a) A maximum device efficiency of 18.2% was reported for the D18:Y6 composition [16]. b) A maximum device efficiency of 17.0% was reported for PM6:Y6 composition [17]. Figure reproduced with permission from Elsevier Science & Technology Journals [16], and with permission from Springer Nature BV [17].
- Fig. 2.2: The process workflow of the ADA self-run platform. Reproduced with permission from Royal Society of Chemistry [18].
- Fig. 2.3: a) Illustration of the interdependence of parameters involved in the optimization of a bulk heterojunction film. b, c) Illustrations of a large-area roll-to-roll OPV system where the ratio of donor:acceptor and film thickness is optimized by machine learning algorithms from in-situ measured data; d) Machine-learning map constructed to illustrate regions of chemical and photovoltaic interest. b-d) reproduced with permission from Royal Society of Chemistry [19].
- Fig. 2.4: Schematic of a conventional spin-coating process: a) droplets of a bulk heterojunction solution are deposited on the substrate, b) the sample is spun so that centrifugal forces flatten and spread the solution over the substrate, most of the solution is flung off the sample, c) airflow causes most of the solvent to evaporate, leaving behind a thin plasticized film. Image remains the copyright of Ossila. Taken with permission from Ossila.com [20].
- Fig. 2.5: Representation of the morphological evolution of a UU07:PCBM bulk heterojunction subjected to solvent vapor annealing for different times and the impact that different domain formations have on exciton recombination. Reproduced with permission from John Wiley & Sons. [21].

Fig. 2.6: Analytical transmission electron microscopy visualization of crystallization of donor and acceptor domains of a PBDB-T:ITIC bulk heterojunction induced by the application of thermal annealing (a, b) or DIO (f, g). Crystallinity is observed by the formation molecular structures arranged in the shape of parallel rows. Scale in a) is 100 nm and scales in b-e) are 10 nm. Reproduced with permission from John Wiley & Sons [22].

Fig. 2.7: a) Molecular structure of the PM6 donor. b) Molecular structure of the BTP-BO-4Cl acceptor. c) Flowchart of action lines taken to improve dissolution of PM6:BTP-BO-4Cl blend and quality of deposited thin film.

Fig. 2.8 Visual appearance of vials used to qualitatively assess the dissolution of 1 mg of PM6 in 1mL of solvent at room temperature. This picture was taken after 1 min of gentle tapping on the vial. The vial on the left contained chloroform and the vial on the right contained toluene, corresponding to best and worst observed dissolution, respectively, as was observed from the size and number of undissolved specks or clumps of material sticking to the walls of the vial.

Fig. 2.9: Visual appearance of PM6:BTP-BO-4Cl OPV substrates. a) Image of BHJ layer spin-coated on a glass/ITO/PEDOT:PSS substrate as taken by a cellphone camera, and corresponding b-d) reflectance-mode optical microscopy close-ups where film defects caused by “specks” of undissolved of PM6 polymer are shown.

Fig. 2.10: Improved PM6:BTP-BO-4Cl film deposition after overnight dissolution at 120 °C. a) Image of BHJ layer spin-coated on a glass/ITO/PEDOT:PSS substrate as taken by a cellphone camera, and corresponding reflectance-mode optical microscopy close-up.

Fig. 2.11: a) Image of a functional PM6:BTP-BO-4Cl chip with 5 devices (solar cells). The L-shaped contact seen in a) was deposited to facilitate the connection of the cell’s common anode to the corresponding electrical probe in the holder. b) Multi-device testing holder. c) OPV chip placed in the holder for characterization in a solar simulator.

Fig. 2.12: Visual appearance of two glass/ITO/PEDOT:PSS/PM6:BTP-BO-4Cl samples (no thermal treatment) after spin-coating deposition of PFN-Br from a methanol solution.

Fig. 2.13: XRD diffractograms showing no apparent change in crystallographic structure between OPV samples thermally- treated and untreated.

Fig. 2.14: Image of the group’s computer-controlled solvent vapor annealing system. A full schematic and detailed explanation of its components is reported by Jin et al. [23]

Fig. 2.15: In-situ images of the film evolution of two PM6:BTP-BO-4Cl OPV chips during methanol solvent vapor annealing (the area shown corresponds to a section of roughly 3 mm by 3 mm and was captured by a digital camera coupled to a microscope focusing; the area of the OPV chip was roughly 13 mm x 15 mm; the initial thickness of the BHJ film was approximately 108 nm, the thickness of the PEDOT:PSS layer was 30 nm; solvent ratio was 98%, approximate annealing time was 30 min). a-f) Correspond to surface texture evolution of one OPV chip in a chronological order matching the order of the alphabet. e-f) correspond to the chronological film evolution of a second sample.

Fig. 2.16: Soaking setup for static solvent annealing. A sample was placed on the spin-coater chuck, covered with a solution and spun-dry after a certain amount of humidification time had passed.

Fig. 2.17: Effect of PFN-Br/MeOH soaking time on PCE of vacuum-dried PM6:BTP-BO-4Cl solar cells. Blue squares correspond to OPV samples subjected to soaking and the red square corresponds to an untreated sample. Error bars correspond to performance values one standard deviation away from the average.

Fig. 2.18: Effect of PFN-Br/MeOH soaking on various solar parameters, a) on power conversion efficiency, b) on short-circuit current, c) on fill factor, d) on open-circuit voltage, e) on shunt resistance, f) on series resistance. Blue squares correspond to averaged response of soaked solar cells and red squares correspond to as-spun cells. Error bars correspond to performance values one standard deviation away from the average.

Fig. 2.19: Reflectance-mode optical microscopy images of PM6:BTP-BO-4Cl OPV cells subjected to methanol soaking treatment for different times. Images a-c) correspond to different magnified views of an as-spun OPV cell where no texturing spontaneously occurs. d-f) Images correspond to an OPV cell soaked in PFN-Br/MeOH for 10 s, in this case, fine texturization features begin to form. Images g-i) correspond to an OPV cell soaked in PFN-Br/MeOH for 8 min, in this case, texturization becomes severe.

Fig. 2.20: XPS depth profiling of PM6:BTP-BO-4Cl OPV samples. The ratio of F:Cl in the donor and acceptor material, respectively, was used to track possible migration of these materials towards the ITO anode. No PFN-Br was used in this test, the samples were instead prepared as-spun and flushed with methanol.

Fig. 2-21: Image of a Voronoi polygon pattern.

Fig. 2-22: Core-shell structure of PEDOT:PSS. Reproduced with permission from Royal Society of Chemistry [24].

Fig. 2-22: Copolymer microstructure of the PEDOT:PSS system forms a core-shell arrangement. The application of a solvent like methanol on a PEDOT:PSS film can cause the separation of PEDOT from PSS, resulting in PEDOT rich domains (blue) and PSS-rich domains (gray) which create pathways for electronic transport (hole transport) through the conductive PEDOT domains. Reproduced and adapted with permission from CC BY 4.0 open access license [25].

Fig. 2-23: Alemu et al. reported that a methanol immersion treatment caused serrated lines to appear in PEDOT:PSS films, as shown in their SEM micrographs. The right micrograph shows a pristine PEDOT:PSS film and the left micrograph corresponds to film that had been immersed in methanol. Reproduced with permission from Royal Society of Chemistry [26].

Figure 3.1: a) Ionic conduction motion of a negative charge in response to an external electric field and b) dipolar polarization of a water molecule.

Figure 3.2: A microwave system custom-designed to reduce standing wave hot-spots. Reproduced with permission from IEEE [27].

Fig. 3.3: a) A roll-to-roll assembly system. To the left is shown a ZnO slot-die deposition module, on the center a P3HT:PCBM deposition module, and on the right a PEDOT:PSS deposition module. Meters-long flexible films can be quickly manufactured using this system. Reproduced with permission from Royal Society of Chemistry [28]. b) Molecular structure of the P3HT donor, c) Molecular structure of the PC₆₁BM acceptor.

Fig. 3.4 Molecular structure of ZR1 donor (right) and of BTP-BO-4Cl acceptor (left).

Fig. 3.5: a) Position of Teflon vessel and crucible in the microwave (upper lid removed for insertion of in-situ thermometer probe). b) Three initial microwave annealing configurations used during screening calibration experiments. Type I: the OPV chip is placed on the Teflon base upright and the thermometer probe is in contact with the BHJ, Type II: The OPV chip is placed upside down with the BHJ making contact with a Si heating element while the probe is in contact with the glass side of the chip, Type III: a pair of silicon heating elements are placed on the top and on the bottom of the OPV chip

forming a sandwich structure, the chip itself is placed upside down and the thermal probe is in contact with the uppermost heating element.

Fig. 3.6: Thermal profile of the microwave cavity. The highest microwave antinode was located at the center of the cavity; hence, the Teflon vessel was placed in that position to take advantage of the constructive interference.

Fig. 3.7: Thermal profile of the cavity after the introduction of the Teflon vessel and SiC crucible. The cooler central region of the thermogram likely occurred because Teflon has a high degree of transparency to microwaves, therefore little microwave absorption took place in that position.

Fig. 3.8: Forced cooling setup. A N₂ exhaust line was placed over the Teflon vessel for rapid cooling of substrates and a fan was used to cool down the SiC crucible.

Fig. 3.9: Calibration ramp of microwave annealing time vs maximum substrate temperature. Multiple substrate configurations (glass/ITO, glass/ITO/PEDOT:PSS, glass/ITO/PEDOT:PSS/BHJ, glass/ITO/ZnO/BHJ layer structures) were used to confirm that neither the number or content of the layers caused a thermal response discernably different from simple glass/ITO controls.

Fig. 3.10: Consecutive heating and cooling cycles of a P3HT:PCBM solar cell, microwave (MW) annealing time was fixed at 56 s at a medium power setting (microwave option PWR 6).

Fig. 3.11: Continuous microwave annealing of two P3HT:PCBM OPV chips. Convergence temperature is denoted by the blue lines. Target convergence temperature in this screening was 60 °C and was set by varying the SiC mass. Variance from target temperature was roughly ± 7 °C.

Fig. 3.12: Non-uniform color profile of solar cells prepared from a glass/ITO/PEDOT:PSS/P3HT:PCBM layer structure. a) Single P3HT:PCBM chip and b) double chip setup in the “instant” mode. Non-uniform coloration caused by microwave annealing became significant at higher temperatures or longer annealing times. c) Appearance of reference solvent vapor- and hotplate- annealed P3HT:PCBM chips.

Fig. 3.13: Solar cells prepared from a glass/ITO/PEDOT:PSS/P3HT:PCBM layer structure. Continuous mode annealing of P3HT:PCBM chips for extended times, a) using a static configuration and b) using a rotating configuration.

- Fig. 3.14: Solar cells prepared from a glass/ITO/PEDOT:PSS/DRCN5T:IT-4F/Al/Mg layer structure. Side by side images of an instant mode (Type I configuration) microwave-annealed OPV chip before and after metal contact deposit. Individual devices are labeled in white.
- Fig. 3.15: Solar cell corresponds to a glass/ITO/PEDOT:PSS/P3HT:PCBM layer structure. Microwave edge defects persisted in the Type II configuration.
- Fig. 3.16: Comparison of the visual appearance of three P3HT:PCBM OPV samples microwave-annealed using a Type I and a refined Type III configuration. Discoloration corresponding to hotspots is considerably reduced by the introduction of Si heating elements above and below the substrate. Note that small areas of non-uniform heating were still present on the borders for samples prepared using the Type III setup; however, those imperfections did not greatly impact device quality.
- Fig. 3.17: Temperature calibration of a continuous mode Type IV treatment. Target “convergence” temperature was set at the P3HT:PCBM optimized value of 150 °C. Multiple adjustments to the SiC mass in the control crucible were made to achieve it. A magnified view of the microwave duty cycle profile is shown in the inset.
- Fig. 3.18: Type-IV microwave annealing configuration. Here, the OPV cell is flipped so the glass substrate faces upwards. A moderate nitrogen gas flow is allowed to flush oxygen inside the funnel for 2 minutes prior to annealing to reduce the possibility of oxidation of the BHJ. Afterwards, the gas line is carefully disconnected, and the microwave door is closed to perform the annealing treatment.
- Fig. 3.19: a) Thermograph of a Si heating element showing a region of intense heating on one edge, likely corresponding to the position of antinodes in the microwave cavity (taken approximately after 30 s of microwave exposure). b) Visual inspection of the heating element immediately after microwaving.
- Fig. 3.20: Thermographs of solar cell and heating element taken a) immediately after microwaving and b) after several minutes of cooling. The physical location of the solar cell is marked by a black square and was always placed at the center of the wafer during the entire project.
- Fig. 3.21: Calibration curve of microwave time vs temperature for the Type IV configuration, taken by measuring the temperature various glass/ITO substrates.

Fig. 3.22: Cracking effect of PFN-Br/MeOH on the active layer if the electron transport layer is spin coated after thermal annealing.

Fig. 3.23: Effect of microwave time on power conversion efficiency for different batches of individual ZR1:BTP-BO-4Cl solar cells (different colors represent different batches). The individual data points in this graph correspond to the averaged *PCE* of multiple devices in the OPV chip. Error bars correspond to performance values one standard deviation away from the average.

Fig. 3.24: Effect of microwave time on power conversion efficiency for ZR1:BTP-BO-4Cl solar cells. The data points correspond to averaged results of multiple solar cells annealed under the same conditions. Error bars correspond to performance values one standard deviation away from the average.

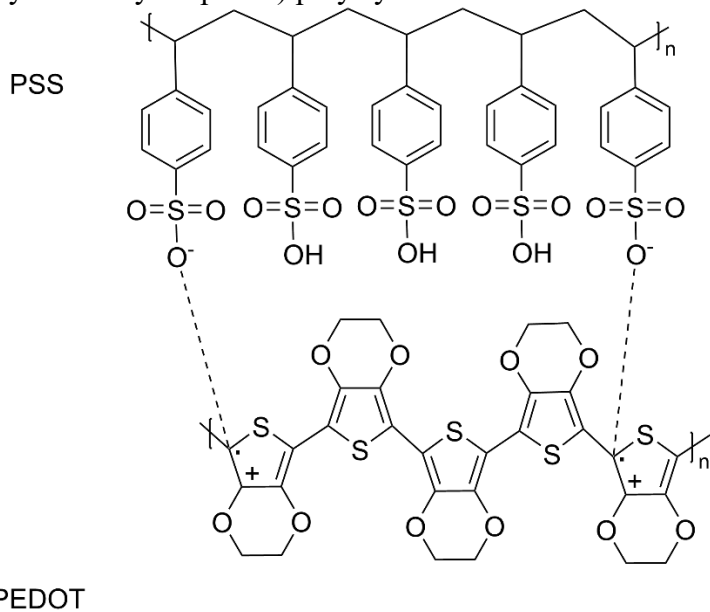
Fig. 3.25: Effect of microwave annealing time on various solar parameters, a) on power conversion efficiency, b) on short-circuit current, c) on fill factor, d) on open-circuit voltage, e) on shunt resistance, f) on series resistance. Blue squares correspond to averaged response of microwaved solar cells, green squares correspond to unannealed cells, and red to hotplate annealed cells. Error bars correspond to performance values one standard deviation away from the average.

List of abbreviations

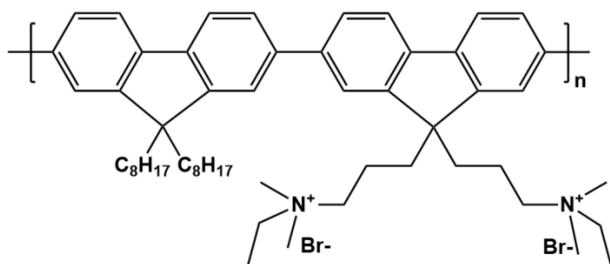
OPV	organic photovoltaic cell
OSC	organic solar cell
BHJ	bulk heterojunction
PCE	power conversion efficiency
FF	fill factor
V_{oc}	open-circuit voltage
J_{sc}	short circuit current density
R_s	series resistance
R_{sh}	shunt resistance
mg	milligram
mL	milliliter
cm	centimeter
mm	millimeter
mW	milliwatt
v/v	volume by volume
w/w	weight by weight
tot. conc.	total concentration
SVA	solvent vapor annealing
TA	thermal annealing
mw	microwave
mw-TA	microwave thermal annealing
hp-TA	hotplate thermal annealing
rpm	revolution per minute
atm	atmosphere
AFM	Atomic force microscopy
XPS	X-ray photoelectron spectroscopy
XRD	X-ray diffraction
RMS	root mean square
No.	Number
Ref.	Reference
ITO	Indium Tin Oxide

Abbreviations of chemical compounds

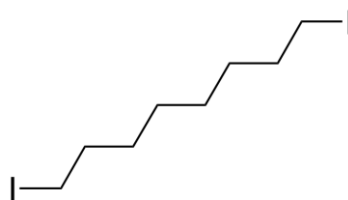
PEDOT:PSS Poly(3,4-ethylenedioxythiophene) polystyrene sulfonate



PFN-Br Poly(9,9-bis(3'-(N,N-dimethyl)-N-ethylammonium-propyl)-2,7-fluorene)-alt-2,7-(9,9-dioctylfluorene))dibromide

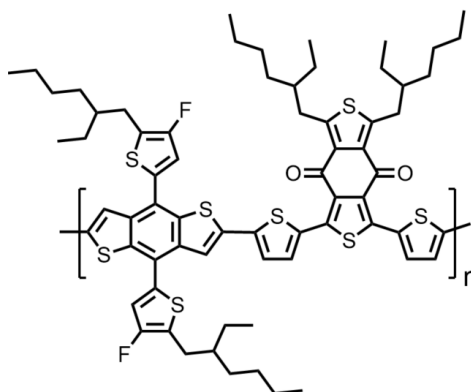


DIO Octamethylene diiodide



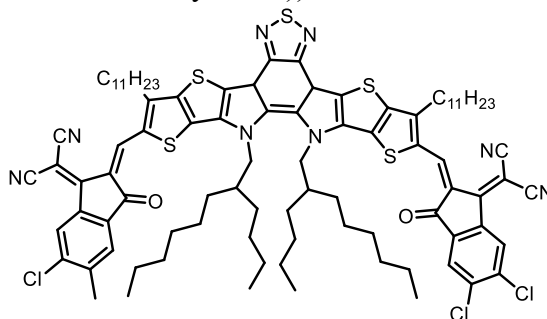
PM6

Poly[(2,6-(4,8-bis(5-(2-ethylhexyl-3-fluoro)thiophen-2-yl)-benzo[1,2-b:4,5-b']
dithiophene))-alt-(5,5-(1',3'-di-2-thienyl-5',7'-bis(2-ethylhexyl)benzo
[1',2'-c:4',5'-c']dithiophene-4,8-dione)]



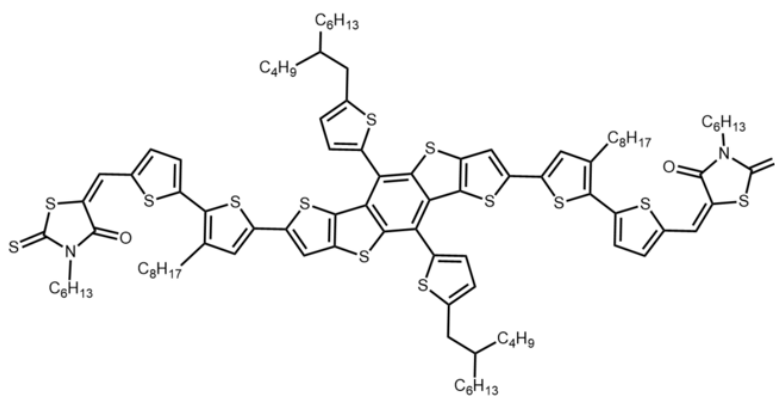
BTP-
BO-4Cl

2,2'-((2Z,2'Z)-((12,13-bis(butyloctyl)-3,9-diundecyl-12,13-dihydro-[1,2,5]
thiadiazolo[3,4-e]thieno[2',3'':4',5']thieno[2',3':4,5]pyrrolo[3,2-g]thieno
[2',3':4,5]thieno[3,2-b]indole-2,10-diyl)bis(methanylylidene))bis(5,6-dichloro-3-
oxo-2,3-dihydro-1H-indene-2,1-diylidene))dimalononitrile

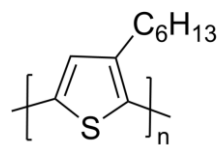


ZR1

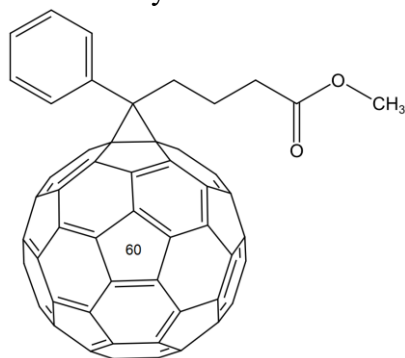
5,5'- [[4,8-bis[5-(2-butyloctyl)-2-thienyl]dithieno[2,3-d:2',3'-d']benzo[1,2-b:4,5-
b']dithiophene-2,6-diyl]bis[3'-octyl[2,2'-bithiophene]-5'',5-diyl) methylidyne
]]bis[3-hexyl-2-thioxo-4-thiazolidinone]



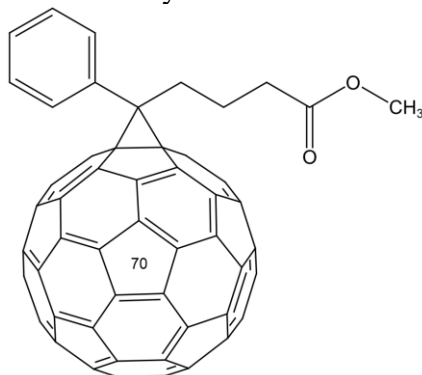
P3HT Poly(3-hexylthiophene-2,5-diyl)



PC₆₁BM [6,6]-Phenyl-C61-butyric acid methyl ester



PC₇₁BM [6,6]-Phenyl-C71-butyric acid methyl ester



Chapter 1

A brief introduction to organic photovoltaic solar cells (OPVs)

1.1 The global energy landscape and photovoltaic solar cell technology

Currently, the world's population stands at roughly 8 billion, with some estimates suggesting growth up to 9 – 11 billion by 2060 [29]. Energy is a core pillar in human development. In its electrical and chemical form, energy is required to support virtually every human activity, from transportation, to heating, to food production, to lighting, to healthcare, to communications, and many others. The continued increase in population and energy consumption in a technology-driven age will exacerbate global energy demand. Currently, fossil fuels continue to constitute the bulk of the world's energy supply, accounting for more than 80% of total primary energy supply [30].

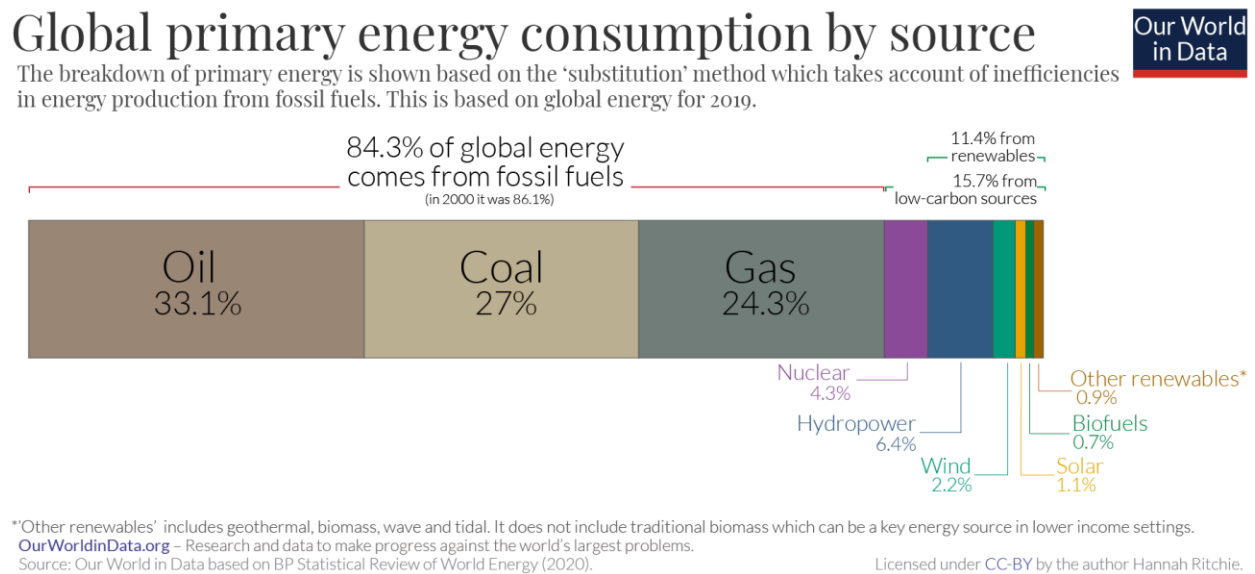


Fig. 1.1: 2020 distribution of global primary energy consumption by source. Retrieved from OurWorldInData.org on October 2, 2021. CC-BY license [2].

It has been clearly established that the production and consumption of fossil fuels is a leading cause in anthropogenic climate change [31], is directly related to increases in health problems

associated with pollution and environmental destruction [32], and continues to be a source of worry around energy security and future supply. The seriousness and importance of transitioning to renewable sources of energy cannot be understated and while important efforts have been made to develop cleaner energy sources, a complete transition to greener energy sources remains a pressing unfulfilled reality. Availability of natural resources for primary renewable energy generation like water flows for hydroelectric projects, regions with adequate wind flows for eolic energy, underground surface accessibility for geothermal power, etc. is not geographically uniform. A more ubiquitous resource is solar energy.

Solar energy is the world’s most abundant resource, and it is estimated that fewer than 8 hours of sunlight on terrestrial earth could satisfy global energy demand for a year [33]. While not every country receives the same amount of irradiation, its availability is greater than other energy sources. Thus, it is a much more ‘democratic’ energy source as it is globally distributed.

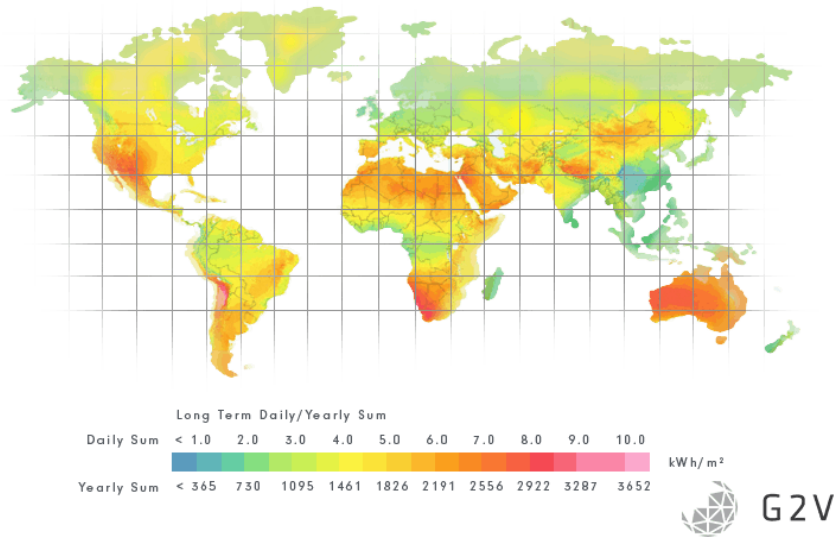


Fig. 1.2: Map of solar irradiation on terrestrial Earth. Reprinted with permission from G2V Optics [2].

One of the most promising ways to harness solar energy is the use of photovoltaic solar cells. As is shown in Fig. 1.3, multiple types of photovoltaic cells exist, including those based on amorphous poly- and mono-crystalline silicon [34], compositions of metals like CdTe [35] and CIGS [36], the new family of halide perovskite compounds [37], dye-sensitized [38], and organic photovoltaic cells, the latter of which are the subject of study of this thesis work [39], [40].

Best Research-Cell Efficiencies

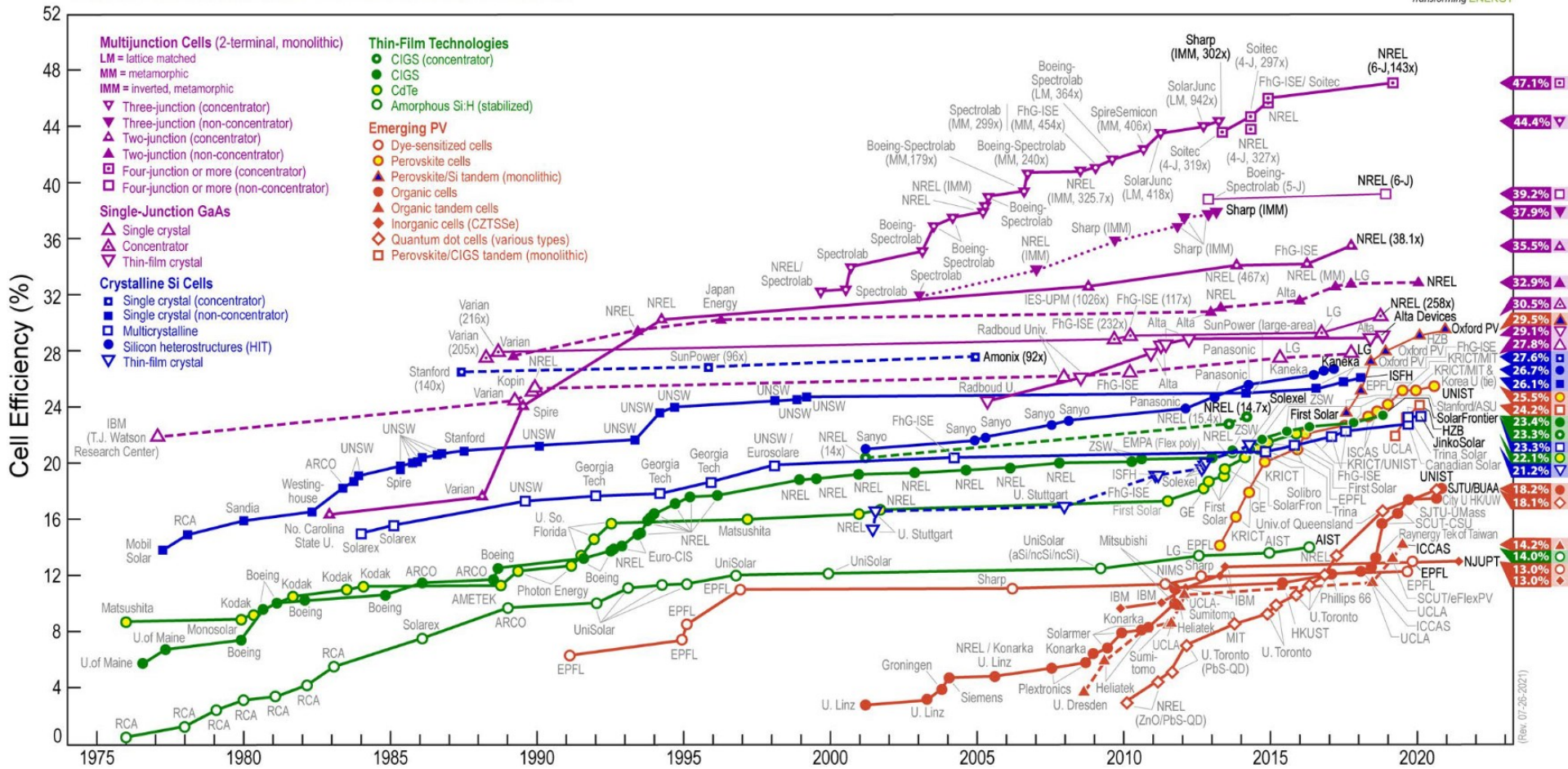


Fig. 1.3: Evolution of power conversion efficiency of different types of photovoltaic cells as published on the NREL website on October 8, 2021. This plot is courtesy of the National Renewable Energy Laboratory, Golden, CO. [3].

1.2 Organic photovoltaic solar cells

Fig. 1.3 shows the incremental improvement in efficiency achieved for different types of photovoltaic (PV) solar cells as per NREL. One technology that has gained considerable attention is organic photovoltaic cells (OPVs, or organic solar cells, OSCs). These cells are manufactured from polymeric or small molecule carbon-based materials and can be efficiently mass-manufactured from solution-processable methods like roll-to-roll printing, slot-die casting, spray coating, etc. [28], [41]. Other advantages of these cells are that they could have energy payback times as small as hours [42], they are semi-transparent, color-tunable, and can be deposited on flexible substrates, as shown in Fig. 1.4 and 3.4. Additionally, the photoactive layer thickness of these cells is normally in the order of 100 – 300 nm [43] and overall cell thickness is $\approx 2 \mu\text{m}$ [44], which means that very little material is required to produce lightweight large-area panels (estimated weight is 4 g/m^2 for plastic substrate OPV panels [44]), resulting in a much lower energetic and financial cost than traditional silicon-based PV cells that are normally manufactured as thick slabs of ultra-refined raw material and can weigh between $10 - 15 \text{ kg/m}^2$ [45].

Due to considerable research efforts that span over two decades [46], the latest state-of-the-art OPVs have reached efficiencies above 18% [47], [48]. Already, OPVs are becoming an additional tool in the arsenal of photovoltaic technologies, although it must be said that research is still needed to improve their stability, durability, and recyclability. It is fair to say that these solar cells will be very attractive from a production to decommissioning perspective. A key advantage that could help mass-commercialization of OPVs is that they do not require burdensome modifications to site infrastructure to accommodate for heavy panels (e.g. fabrication, transportation, and installation of heavy-duty aluminum or stainless-steel frames, ballast mounts, poles, concrete foundations, etc.). Additionally, it has been reported [49] that OPVs could be manufactured on cellulose substrates as an alternative to plastic or glass, and chemical processes can be used to recover raw materials like the polymeric photoactive layer and metal contacts, further adding to their value offer and technological competitiveness. The unique characteristics of OPVs make them suitable for a versatile gamma of applications, ranging from devices for the Internet of Things [50], to wearable and stretchable electronics [51], [52], to building-integrated [53] and remote off-grid power generation [54], to agrovoltatics [55], to lightweight military surveillance drones [56], and more.

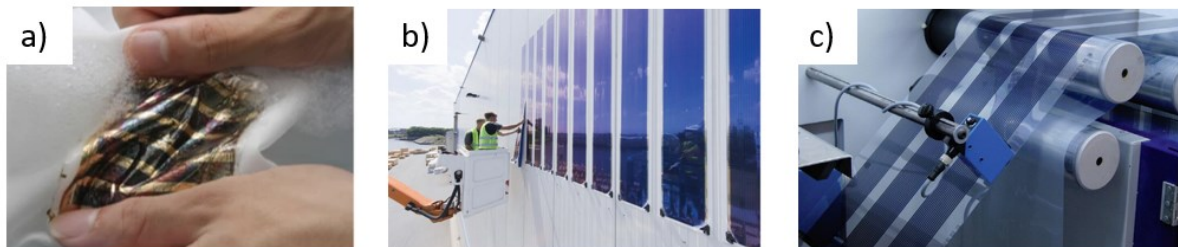


Fig. 1.4: a) Washable and flexible OPV solar cell for clothing integration, reproduced with permission from Springer Nature BV [4]. b) OPV solar overlays for building integration, reproduced with permission from John Wiley & Sons [5]. c) Roll-to-roll printing for mass deployment, reproduced with permission from Elsevier Science & Technology Journals [6].

1.3 Basic OPV theoretical concepts

An organic photovoltaic solar cell consists of a tandem structure of layers that resemble a sandwich, shown in Fig. 1.5.

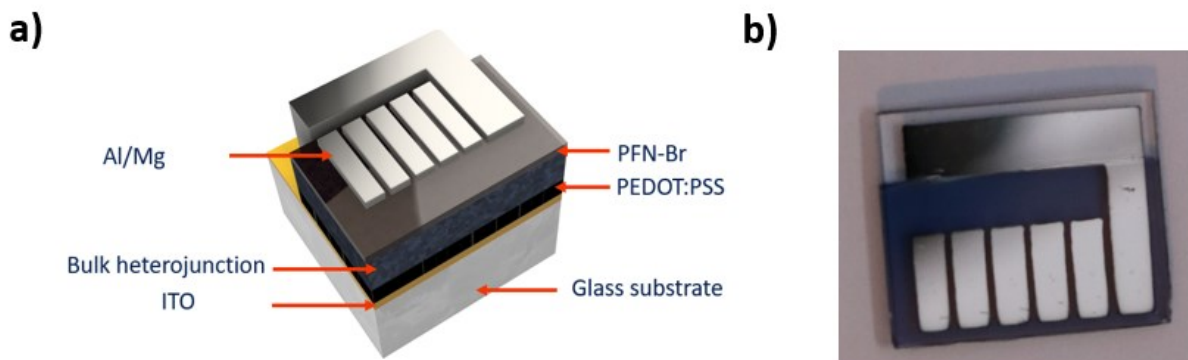


Fig. 1.5: a) Layer schematic of a conventional architecture OPV chip containing 5 solar cells. b) A sample OPV chip manufactured in our group for research purposes.

On the outer sides of the OPV cell are charge collecting electrodes. Two types of solar cell architectures exist, conventional or inverted. The main distinction is the order in which the constituent layers are deposited, which will determine the flow of charge carriers collected at which electrode. The architecture used throughout this thesis work, unless otherwise indicated,

was the conventional architecture. In the conventional architecture, an optically transparent and conductive electrode composed of a layer of indium tin oxide (ITO)-on-glass, is used as the anode, and an evaporated metal serves as the reflective counter electrode. The ITO layer is coated with a conducting PEDOT:PSS hole transport layer, upon which the active light-absorbing layer, the bulk heterojunction (BHJ), is deposited. The BHJ is composed of a mixture of donor and acceptor organic semiconductor materials, and serves as the ‘meat’ of the sandwich. The BHJ is then capped with the reflective top electrode that could include an electron transport layer in this forward cell configuration.

As stated earlier, the heart of the OPV cell is the light absorbing active layer, which can comprise a number of different structures as shown in Fig. 1.6.

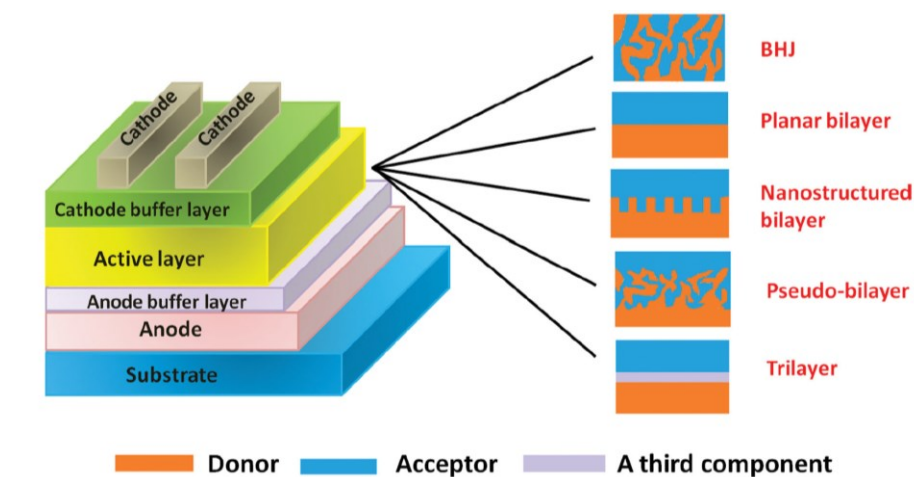


Fig. 1.6: Different types of active layer geometries. Reproduced with permission from John Wiley & Sons [7].

These different geometries will result in varied amounts of phase boundary area between the donor and the acceptor materials, an important variable to maximize photovoltaic performance. The photoactive layer form that has proven to be the most practical to fabricate on a large scale is the bulk heterojunction, as it relies upon the spontaneous nanoscale phase segregation between these donor and acceptor materials, and has a large degree of boundary interface area between them. In contrast, other geometries like the nanostructured- or pseudo-bilayers are more complex in that they require specialized steps like photolithography or chemical etching to produce the comb-like interpenetrated networks of donor and acceptor [57], [58], [59], [60], [61], [62], [63]. In terms of

the bulk heterojunction, the blending of the active layer is typically performed by mixing the donor and acceptor in an appropriate solvent, with any additives as required [64], [65], [66]. Post-deposition treatments, termed annealing, of the deposited active layer may be required to induce nanoscale phase separation of the donor and acceptor to form the BHJ, as will be discussed later in this thesis work.

1.3.1 Operating principles of OPVs and the bulk heterojunction

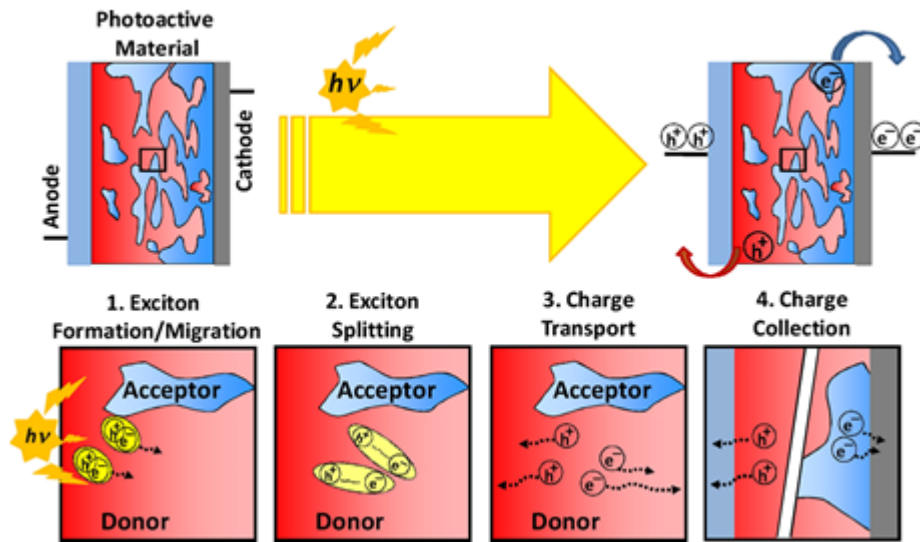
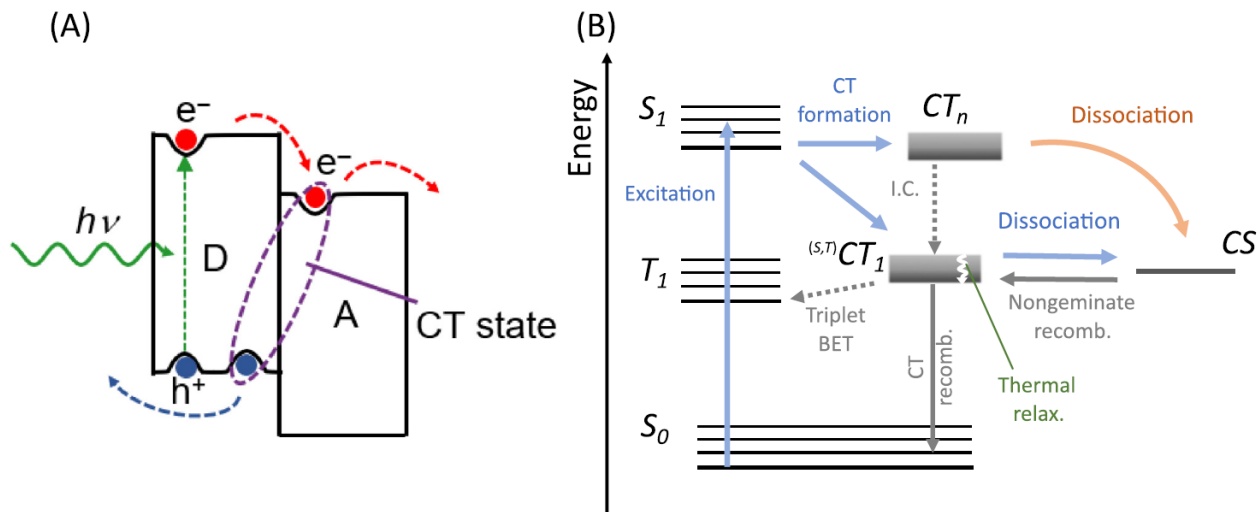


Fig. 1.7: a) Schematic of the processes involved in converting radiation to electrical energy in the bulk heterojunction of an OPV solar cell. Reproduced with permission from Elsevier Science & Technology Journals [8].



Trends in Chemistry

Figure 1. Change Transfer (CT) and Recombination via CT States at an Organic Heterojunction (HJ). (A) Schematic of photogeneration processes in a type-II organic HJ. An exciton generated on photon absorption diffuses to the interface where CT gives rise to intermediate CT excitons that subsequently dissociate. (B) Jablonski diagram illustrates the formation of multiple electronic CT states following CT from excited state S_1 . Relaxation occurs through internal conversion (I.C.) from CT_n to CT_1 and within each CT manifold. All CT states either dissociate to charge-separated (CS) states or decay to the ground state S_0 (CT recomb.). Separated charges may nongeminately recombine to the CT state. The reduced overlap between electron and hole on neighboring molecules results in a small exchange-energy splitting between singlet (sCT) and triplet (tCT) spin states. The presence of low-energy triplet states at the donor or acceptor enables triplet back energy transfer (BET) from the CT state.

Fig. 1.8) Schematic of the exciton dissociation processes from intermediate charge transfer states in the bulk heterojunction of an OPV cell. Reproduced with permission from Elsevier Science & Technology Journals [9].

There main mechanisms involved in the operation of an OPV are described in the following section:

1. Exciton formation and migration

In an organic solid, charge carriers exist in the form of electrons and vacancies left behind (holes) when those electrons are promoted to excited states. The name given to an electron-hole pair is “exciton” [67]. In the bulk heterojunction, these excitons are strongly bound due to coulombic forces. The exciton binding energy can be estimated as [10]:

$$E_b = E_d - E_a,$$

where E_a is the energy difference between an electron-pair in the same molecular unit, and E_d is the energy difference between two separate and unrelated electron and hole particles on different molecular units, shown in Fig. 1.8. The binding energy in an organic material can be as high as

0.5 eV, which is much higher than that in an inorganic material [68]; in the latter case of the inorganic material, the binding energy is insignificant and the generated charges are free to migrate to their respective electrodes, driven by the potential gradient across the device.

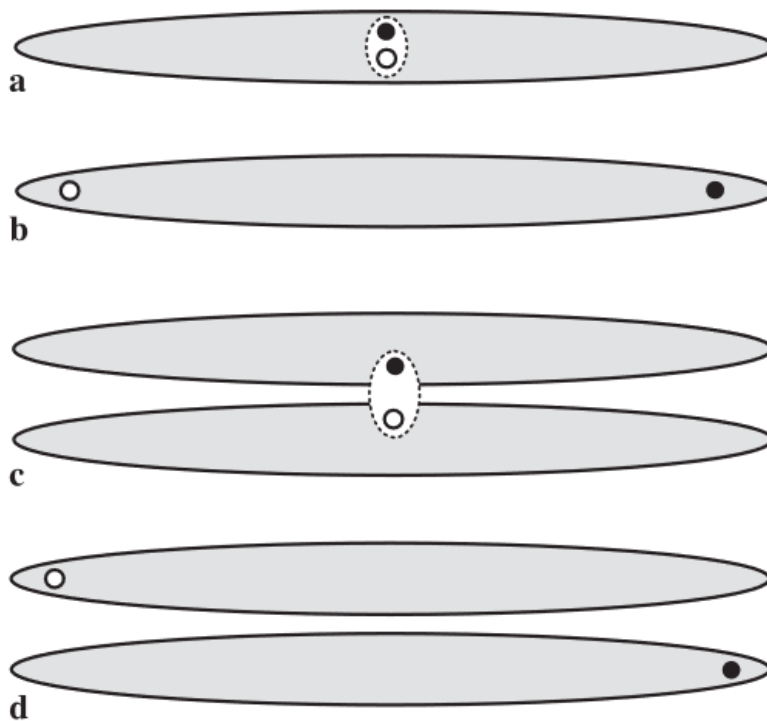


FIGURE 1 Schematic representation of electron-hole pairs in organic semiconductor. **a** bound electron-hole pair (exciton) on one molecule, **b** unbound electron-hole pair on one molecule, **c** bound electron-hole pair involving two adjacent molecules (charge-transfer exciton), and **d** unbound electron-hole pair on different molecules

Fig. 1.9: a) Representation of electron-hole pairs in organic molecular units. Reproduced with permission from Springer Nature BV [10].

Photons with an energy greater than the HOMO-LUMO gap [49] are absorbed in bulk heterojunction, promoting the excitation of electrons from a HOMO to a LUMO state and giving rise to photogenerated electron-hole pairs generates called Frenkel excitons. As will be discussed, the exciton binding energy of the electron-hole pair of the exciton must be overcome before the individual charges can be separated.

2. Exciton dissociation

The typical distance that a Frenkel exciton can diffuse through the donor towards an interface boundary before becoming lost to recombination is typically 5-20 nm [69], although modifications of molecular structure can result in increases of this distance up to 50 nm [70]. Thus, in the bulk heterojunction, a balance must be struck between larger donor domain sizes which may absorb more photons, but have longer diffusion lengths that may result in exciton recombination in the donor, called geminate recombination [71], [72]. Once the Frenkel exciton reaches the donor-acceptor interface of the bulk heterojunction, the electrochemical driving force of the interface can overcome the exciton binding energy and dissociate into free charges, with the electrons migrating to the acceptor material and the hole remaining in the donor [73].

3. Charge transport

Once generated, these free charges will travel towards the anode or cathode due to the cascading energy level structure of the solar cell formed by the organic materials and the electrodes with different work functions [74]. The electrons will hop along delocalized π - π states formed by the conjugated molecules towards the cathode while the holes will hop towards the anode [75]. During this diffusion, the charge carriers can become lost due to a number of reasons. For instance, charges may encounter an interfacial boundary and recombine with oppositely-charged charges via non-geminate recombination; charges may also encounter trap sites due to the disorder of the molecular organization in the deposited film and possible contamination; unbalanced carrier mobilities may cause regions of charge accumulation that result in recombination [72], [76], [77]. This loss or hindrance in charge transport will translate to a decrease in fill factor, open circuit voltage, and short circuit current density, thereby limiting the overall power conversion efficiency of the solar cell [75].

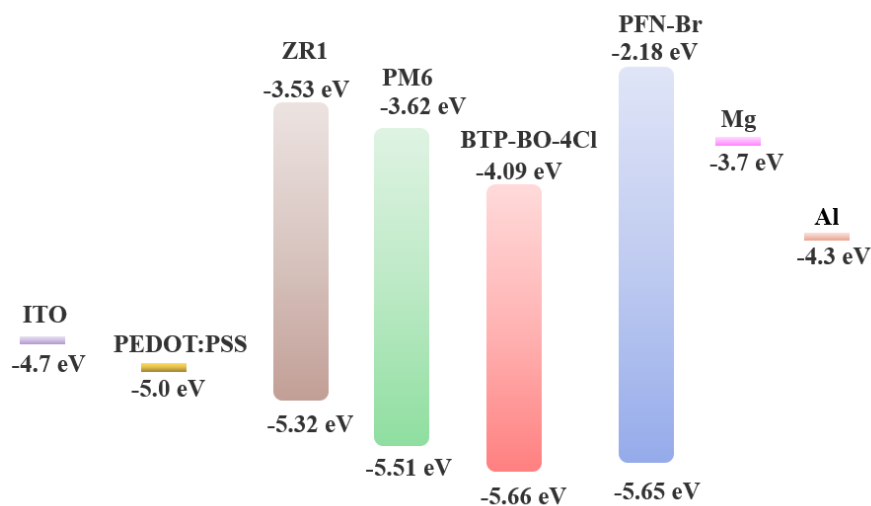


Fig. 1.10: Flatband energy level diagram aligned at the vacuum level for different materials used in this thesis work. Values for HOMO and LUMO levels were obtained from the following references: ITO, PEDOT:PSS, and PFN-Br [11], PM6 and BTP-BO-4Cl [12], ZR1[13], Mg and Al [14].

4. Charge collection

To minimize the number of holes or electrons collected the incorrect electrode, transport layers also known as blocking layers are commonly introduced; these are intermediate layers that preferentially allow the transport of either a hole or an electron [78]. This way, non-geminate charge recombination can be reduced. Once collected at the electrodes, an external circuit may be connected to form an electrical current and extract work from the system.

1.4 Photovoltaic metrics

In a laboratory setting, controlled illumination via a solar simulator is required to benchmark the performance of a solar cell in a manner that is internally comparable from experiment to experiment and externally among the wider research community. The simulator is designed to mimic the irradiance and spectral profile of the sun under standardized conditions, and generates a characteristic JV curve of the organic photovoltaic cell by measuring the generated photocurrent density response vs applied bias voltage.

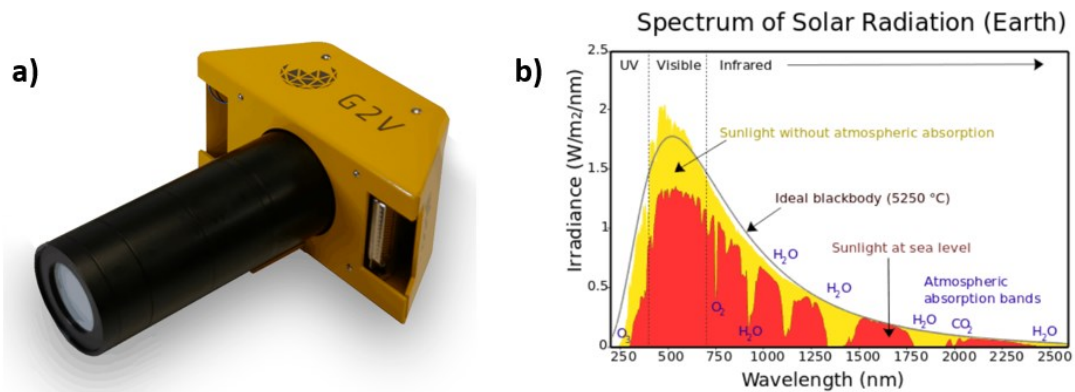


Fig. 1.11: a) Picture of a high-precision LED solar simulator manufactured by G2V Optics and b) solar spectral profile on earth. Reproduced with permission from G2V Optics [2].

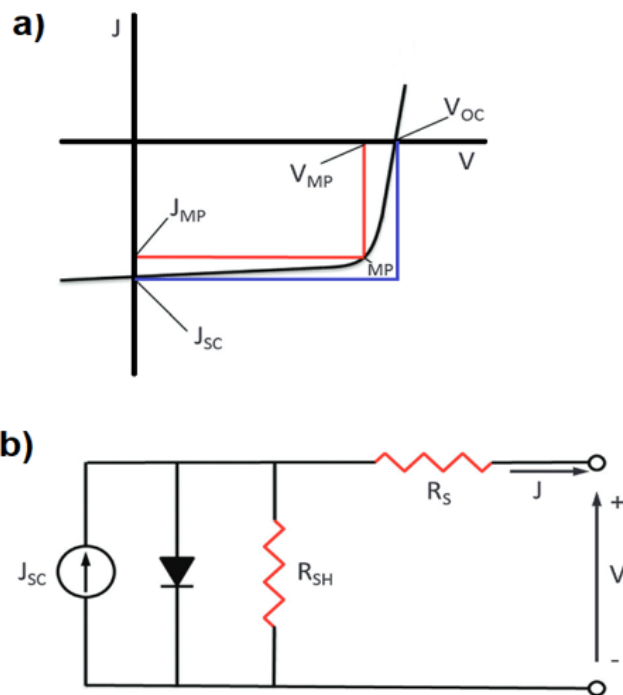


Fig. 1.12: a) Idealized characteristic J - V curve of an OPV cell. b) Equivalent photodiode circuit representation of an OPV cell. Abbreviation definitions: J_{SC} refers to short circuit current density; R_S to series resistance; R_{SH} to shunt resistance; V applied bias voltage, J current density. MP refers to a “maximum point”. Reproduced with permission from Royal Society of Chemistry [15].

Important solar performance metrics can be calculated from a JV curve like the one shown in Fig. 1.12. Although much more precise definitions and approximations exist, they include physical and electronic concepts beyond the scope of this work.

Power conversion efficiency (PCE): This value refers to how much electrical power is generated by the solar cell with respect to the power received from the sun [15]. It is defined as:

$$PCE = \frac{P_{out}}{P_{in}} = \frac{V_{oc} \times I_{sc} \times FF}{P_{in}} \times 100$$

where P_{in} is calculated from the output intensity of the simulator and the area of the solar device.

Fill factor (FF): This value refers to an ideality figure of merit that is useful to track the shape of the JV curve. Its physical meaning is related to the maximum power that can theoretically be extracted from the cell by taking into account how difficult it is for charges to be extracted [15]. It is defined as:

$$FF = \frac{J_{MP} \times V_{MP}}{J_{SC} \times V_{oc}}$$

Open circuit voltage (V_{oc}): This value refers to the maximum electrochemical potential of the cell, calculated under no current flow conditions, and can be approximated [15], [79] by:

$$V_{oc} \approx HOMO_{donor} - LUMO_{acceptor}$$

Short circuit current density (J_{sc}): This value refers to the maximum current generated under a null resistance load (no applied bias). Its physical meaning is related to the number of excitons generated from light absorption, and the efficiency of charge dissociation, transport, and collection in the cell [15].

Series resistance (R_s): This value refers to the sum of electrical resistances contributed by each deposited layer. In an ideal solar cell, no internal resistance between the layers would exist and the charge would flow exclusively through the diode [15].

Shunt resistance (R_{sh}): This value refers to losses of current in the cell derived from trapped charges, pinholes, and defects. In an ideal cell, this resistance would be infinite[15].

These resistances may be related by Kirchoff's current law as [15]:

$$J = J_{SC} - J_0 \left(e^{\frac{q(V+JR_S)}{K_B T}} - 1 \right) - V + \frac{JR_S}{R_{SH}}$$

where J_{SH} represents the shunt current and J_0 is the reverse saturation current constant, K_B is the Boltzmann constant, T is the temperature, and q is the elementary charge.

Chapter summary

This chapter offered a brief description on the potential that photovoltaic cells have as an alternative energy source to fossil fuels. A brief discussion was provided on an emerging type of photovoltaic cell, organic solar cells, whose carbon-based composition makes it an attractive option for a wide array of applications. The basic components, operational mechanisms, and performance metrics used to characterize them were introduced.

Chapter 2 of this thesis will deepen the processing parameters involved in the synthesis of OPVs. Different approaches to the assembly of the materials comprising the OPV and optimization will be addressed. This chapter will also discuss approaches to improve the solution processability of PM6:BTP-BO-4Cl OPV cells and will examine the role that different solvent treatments have on increasing photovoltaic performance.

Chapter 3 will begin with a critical examination of the application of microwave annealing as a fast and efficient means of processing organic solar cells, to more easily and reproducibly anneal the bulk heterojunction. The application of microwave annealing using a domestic microwave with temperature readout of the sample is presented. An evaluation of the reproducibility of this annealing approach for devices comprising BHJs composed of P3HT:PCBM and ZR1:BTP-BO-4Cl bulk heterojunctions is discussed.

Chapter 2

The effect of solvent annealing on the PM6:BTP-BO-4Cl bulk heterojunction

2.1 A brief on optimization approaches for high efficiency OPV bulk heterojunctions

2.1.1 The design of high efficiency bulk heterojunctions

The last two decades have been very consequential with respect to the development of organic solar cells. As mentioned in the previous chapter, the PCE of current state of the art OPV cells has surpassed the 18% mark [47]. This result is a considerable scientific achievement given that roughly twenty years ago record efficiency was only $\approx 2\%$ [3]. On the chemical side, so much of this success is due to the remarkable development of low optical band gap materials that are highly absorbent to radiation in the visible part of the solar spectrum [79], [80]. Additionally, well-matched compositions of donors and acceptors with optimized HOMO and LUMO levels, complimentary spectral absorption, and optimized molecular structures have pushed the boundary of efficient charge generation and transport [81], [82], [83], [39].

For instance, in terms of molecular design, synthesis efforts have focused on shifting away from flexible molecules with torsional rotation to materials with a planar conformation structures in the conjugated core backbone to promote electron delocalization, increase charge carrier mobility, and improve molecular packing in thin films [84], [85]. Careful selection of the type and length of side alkyl chains has enabled increased solubility [86] for better control over the quality of deposition and can influence the morphology of the bulk heterojunction [87]. Optimization of the conjugation length of the backbone molecules and adequate pairing of donor and acceptor units in donor materials are approaches used to increase optical absorption and adjust the HOMO-LUMO levels [87]. Part of the goal of synthetic chemists has been to produce polymers using as few synthetic steps as possible at a reasonable cost while maintaining adequate thermal and photochemical stability, energy levels, and phase segregation properties. However, improving the different

molecular properties simultaneously is an enormous synthetic challenge, and high efficiency donors such as PM6 or D18, and small molecule non-fullerene acceptors like Y6 and BTP-BO-4Cl, continue to be high cost due to the challenges of scaling up their syntheses. In addition, optimization of the actual small molecules in OPV devices requires an enormous quantity of resource-intensive experimental testing, much of it by empirical screening, to provide feedback for structural optimization.

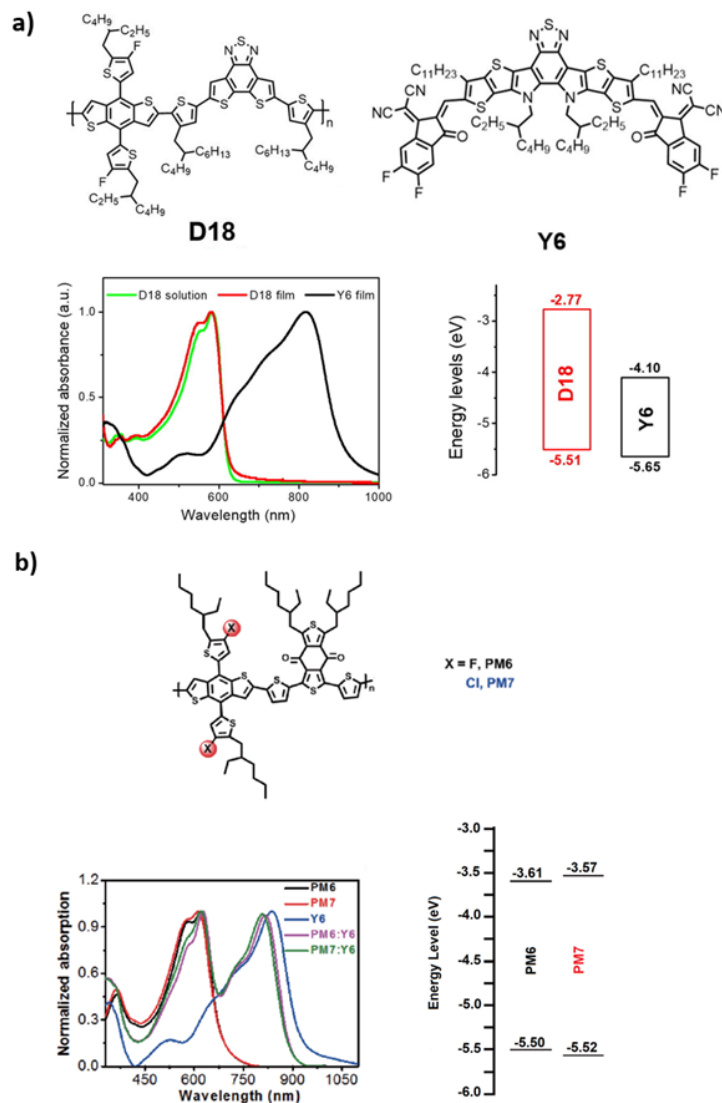


Fig. 2.1: Molecular structures, absorbance spectra, and energy levels of donor:acceptor compositions reported in state of the art OPV cells. a) A maximum device efficiency of 18.2% was reported for the D18:Y6 composition [16]. b) A maximum device efficiency of 17.0% was reported for PM6:Y6 composition [17]. Figure reproduced with permission from Elsevier Science & Technology Journals [16], and with permission from Springer Nature BV [17].

Table 2-I: State of the art donor:acceptor compositions and corresponding photovoltaic metrics, reproduced with permission from Elsevier Science & Technology Journals [1]

Donor	Acceptor	PCE (%)	Jsc (mA/cm²)	FF (%)	Voc (V)	Ref.
PM6	BTP-eC9	17.8	26.2	81	0.84	[86]
PM6	BTP-BO-4Cl	17.3	26.1	77	0.85	[88]
PM7	Y6	17.0	25.6	74	0.90	[17]
PBTT-F	Y6	16.1	24.8	77	0.84	[89]
S1	Y6	16.4	25.4	74	0.88	[90]
T1	BTP-4F-12	16.1	25.2	75	0.85	[91]
P2F-EHp	Y6	16.0	26.7	74	0.81	[92]
D16	Y6	16.7	26.6	74	0.85	[93]
D18	Y6	18.2	27.7	77	0.86	[16]
PTQ10	Y6	16.5	26.7	75	0.83	[94]
PBQ10	Y6	16.3	25.8	75	0.85	[95]

A more sophisticated way researchers are finding suitable combinations of donor and acceptors is by applying chemical computation approaches like machine learning methods coupled with density functional theory calculations to predict which molecular properties (e.g. crystallographic features, backbone structure, alkyl chains, etc.) might result in high performance cells. By using dataset information from libraries like the Genome Initiative or the ANI-1 project to predict energetic configurations or by training the algorithms with empirical data, it is possible identify common denominators and trends with a high likelihood of resulting in high efficiency devices. In this way, it is hoped that the process of finding and matching donor and acceptor materials be accelerated [96], [97] at a lower cost in terms of human researcher time and experimental cost.

However, since a complete theoretical model of organic semiconductors is nonexistent and since purely computational predictions are limited in their predictability of real device behavior, the discovery of good OPV blend compositions continues to be a joint experimental and theoretical endeavor carried out in incremental refinements. Complimentary to theoretical machine learning are experimentally-driven machine learning approaches. These experimental approaches usually begin by carrying out experiments to gather data to train an algorithm. Training can occur in

separate stages: after a sufficiently large amount of data has been gathered (e.g. when measurements from several experiments have been collected) or it can be ongoing and without prior knowledge. One example of ongoing training is found in the ADA self-run platform where an artificial intelligence controls a robotic arm to fabricate, characterize, and optimize thin-film solar devices [98]. In this case, the platform's algorithms select a set of conditions from parameter space to sample, direct the manufacture a solar device, characterize it, and feed the measured data back to the algorithm to select new refined conditions for the next experiment.

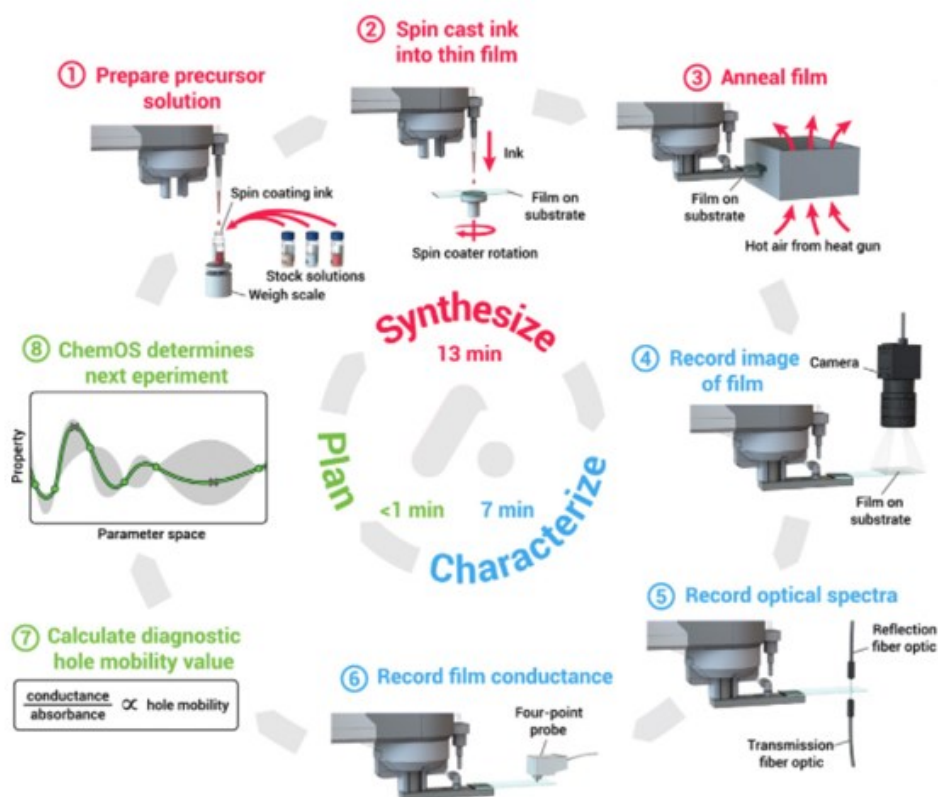


Fig. 2.2: The process workflow of the ADA self-run platform. Reproduced with permission from Royal Society of Chemistry [18].

The function of the algorithm depends on what the scientist is trying to identify. For example, a classification algorithm may be used to sort through a collection of experimental recipes which ones result in devices with a photovoltaic performance above a certain threshold. Other algorithms may be used to exploit or screen the vast parameter space of the bulk heterojunction to map and predict regions of interest. The use of such a type of approach has been reported in the application

of Design of Experiments (DOE) and machine learning to optimize the bulk heterojunction by our group [99], [100] and other researchers [19], [18].

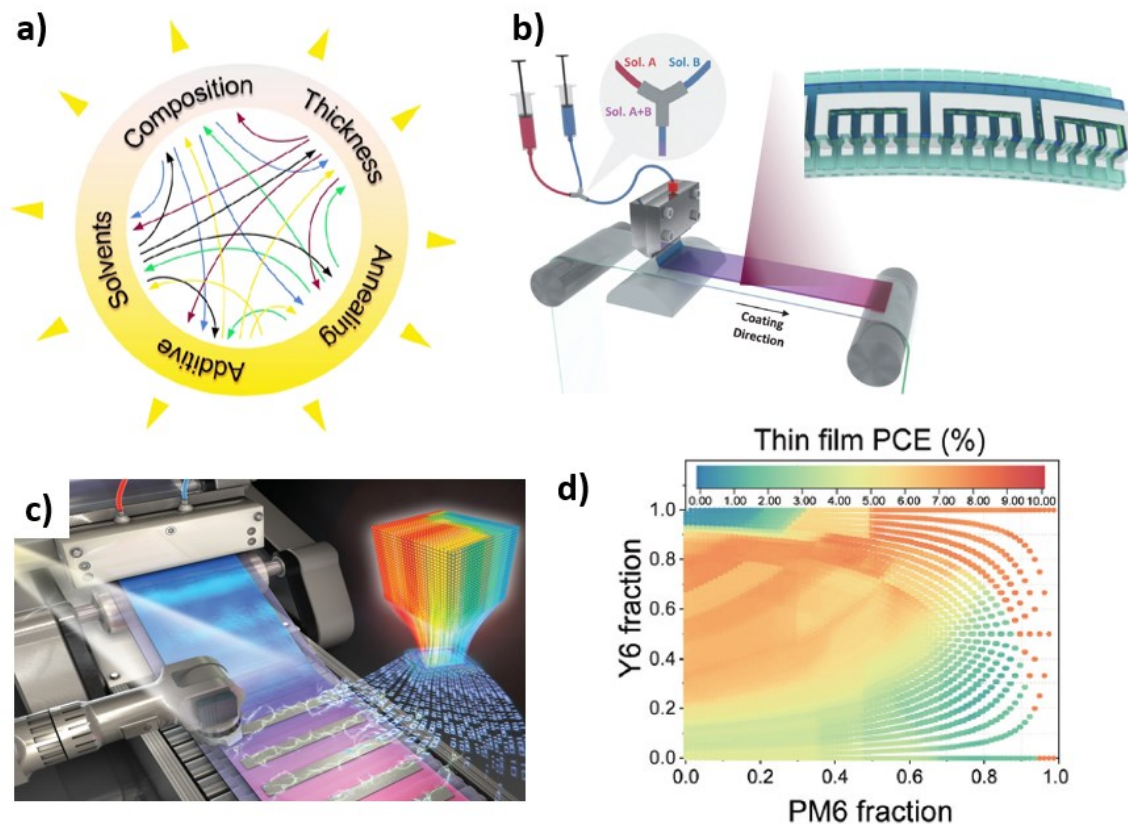


Fig. 2.3: a) Illustration of the interdependence of parameters involved in the optimization of a bulk heterojunction film. b, c) Illustrations of a large-area roll-to-roll OPV system where the ratio of donor:acceptor and film thickness is optimized by machine learning algorithms from in-situ measured data; d) Machine-learning map constructed to illustrate regions of chemical and photovoltaic interest. b-d) reproduced with permission from Royal Society of Chemistry [19].

However, before any kind of computer-assisted exploration or optimization of a facet of OPVs can be implemented, it is first necessary to first devise a fabrication approach that will lead to reliable data quality. Any machine learning algorithm trained on data which is unreliable or not representative of a particular behavior will predict an incorrect result. A euphemism to describe this notion is *bad data in = bad data out*. A takeaway of this emerging research paradigm is that AI-powered experimentation could revolutionize the speed of scientific discovery and accelerate

the transferability of small-scale lab recipes to commercial manufacturing protocols. It is an approach that may direct future organic photovoltaic research and further push the efficiency of this type of solar cell technology.

2.1.2 Post-deposition treatments to promote phase-segregation and solution processability of the bulk heterojunction

At the lab scale, one of the most common approaches for the manufacture of OPVs is the spin-coating approach, where solutions of polymers, small molecules, additives, and solvents are prepared for thin-film deposition. In this approach, an amount of a solution is dripped onto a substrate and a spinning mechanism is activated so that centrifugal forces “flatten” and “spread” the deposited solution over the surface of the substrate [20], [101], as shown in Fig. 2.4. This approach is fast and generally reproducible but is not suitable for large-area manufacturing [102].

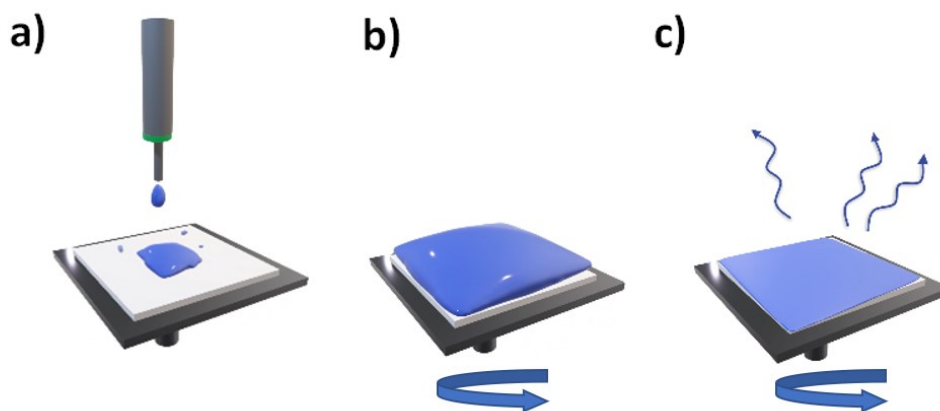


Fig. 2.4: Schematic of a conventional spin-coating process: a) droplets of a bulk heterojunction solution are deposited on the substrate, b) the sample is spun so that centrifugal forces flatten and spread the solution over the substrate, most of the solution is flung off the sample, c) airflow causes most of the solvent to evaporate, leaving behind a thin plasticized film. Image remains the copyright of Ossila. Taken with permission from Ossila.com [20].

For conventional architecture solar cells, PEDOT:PSS is one of the most commonly used hole transport layers deposited on an anode contact (usually ITO). Afterwards, the bulk heterojunction layer is deposited on the PEDOT:PSS, and often, an electron transport layer is added before

evaporation of metal cathode contacts. The manufacture of high efficiency OPVs usually requires the optimization of each layer, either in individual standalone steps or as a global treatment. Multiple optimization approaches exist to achieve this goal, ranging from those focused on modifying the molecular structure of the materials during synthesis to enhance their electronic and molecular properties [82], [103], [79] to those focused on the application of post-deposition treatments to each OPV layer [104], [26], [99], [105]. The overall objective of these optimizations is to boost power conversion by improving the efficiency of photon-to-exciton generation, exciton dissociation, and charge carrier collection.

As was discussed in greater detail in section 1.3 of Chapter 1, it is generally accepted that the bulk heterojunction is the most practical and successful donor:acceptor structure in the manufacture organic solar cells from solution-processable approaches. Part of its success stems from the large surface area available for exciton dissociation formed by the phase segregation of the donor and acceptor materials into submicron (100-300 nm) domains [43]. Multiple post-deposition treatments have been reported for the optimization of the bulk heterojunction, including those based on light irradiation [106] (e.g. laser, visible, infrared), external electromagnetic field alignment [107], mechanical shearing [108], electrical biasing [109], thermal annealing [104], solvent vapor annealing [110], microwave annealing [111], etc. This thesis focused on the application of the latter three of these annealing treatments. Chapter 2 explores the application of solvent vapor annealing to the PM6:BTP-BO-4Cl blend and Chapter 3 will focus on the application of thermal annealing by conventional hotplate and microwave approaches.

The optimization of the bulk heterojunction consists of exposing this active layer to an atmosphere enriched with a solvent for the purpose of enhancing the mobility of the molecules in the film into energetically-favorable configurations [112]. During spin-coating, part of the solvent used to dissolve the donor and acceptor materials evaporates, causing a decrease in the thickness of the deposited film. Because the solvent evaporates quickly, the molecules in the bulk heterojunction become kinetically trapped. When solvent vapor annealing is applied, the bulk heterojunction absorbs part of the solvent, causing the film to swell and plasticize, thus providing it with additional mobility and time for molecular rearrangement to take place due to non-covalent forces interacting on the molecules of the blend [112]. This process is similar to thermal annealing of polymeric

materials where the temperature is raised above the glass transition temperature so the materials rearrange themselves in thermodynamically favorable structures [110].

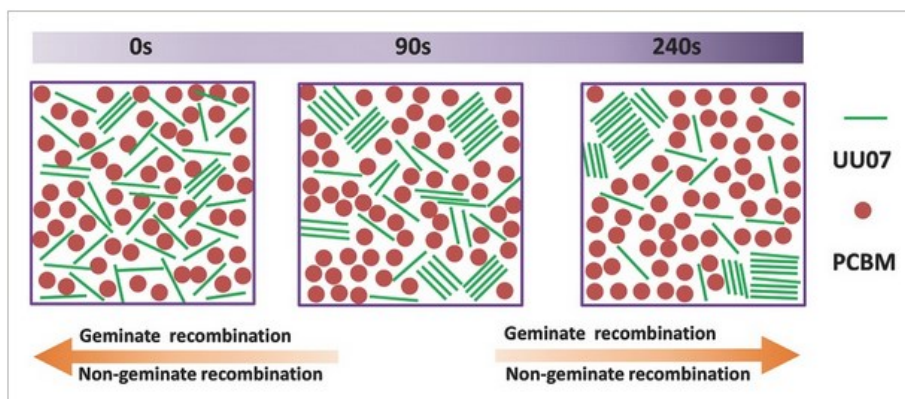


Fig. 2.5: Representation of the morphological evolution of a UU07:PCBM bulk heterojunction subjected to solvent vapor annealing for different times and the impact that different domain formations have on exciton recombination. Reproduced with permission from John Wiley & Sons. [21].

Solvent vapor annealing promotes demixing and aggregation of donor and acceptors into domains [113] whose size can be controlled by varying parameters like the solvent type, solvent ratio, annealing time, and ramping protocol [23]. The control of these parameters can also impact the crystallite size of the phase segregated domains and can lead to specific molecular pi-stacking configurations [110], [114]. For example, the application of solvent vapor annealing could cause molecular chains to stack along preferential in-plane or out-of-plane directions which may be more or less favorable for charge transport along transversal or longitudinal directions.

The careful selection and application of a post-deposition treatment can play a huge role in OPV power conversion efficiency. The materials in a bulk heterojunction may be very well designed to be highly effective in generating excitons and with an adequate energetic profiles but if the appropriate post-deposition treatment is not implemented, the benefits of good molecular design will not yield the expected results.

In the case of the bulk heterojunction, additives and co-solvents may also be introduced to promote phase segregation. Particularly, solvents with high boiling points or those selective to the donor or acceptor can be used to fine tune the morphology.

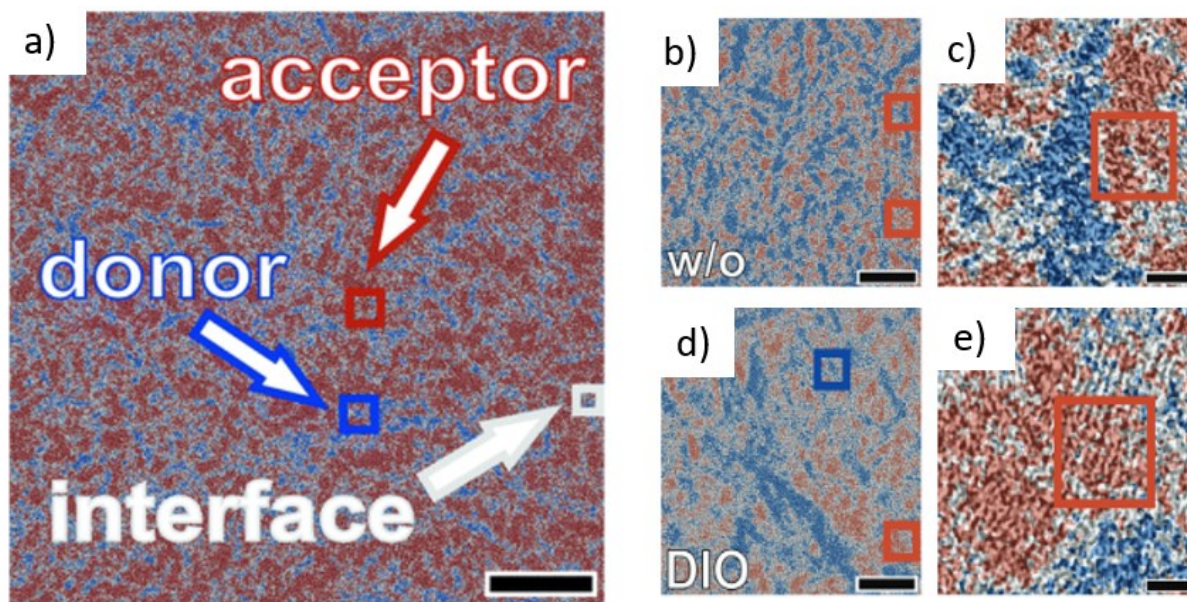


Fig. 2.6: Analytical transmission electron microscopy visualization of crystallization of donor and acceptor domains of a PBDB-T:ITIC bulk heterojunction induced by the application of thermal annealing (a, b) or DIO (f, g). Crystallinity is observed by the formation molecular structures arranged in the shape of parallel rows. Scale in a) is 100 nm and scales in b-e) are 10 nm. Reproduced with permission from John Wiley & Sons [22].

2.2 Chapter results overview

The first part of this chapter consisted of the examination of different experimental variables to improve the reproducibility of OPV cells fabricated from a PM6:BTP-BO-4Cl blend. Although this BHJ has been reported to reproducibly achieve power conversion efficiencies above 16%, difficulties were encountered regarding reproducibility. Therefore, the isolation of various steps in the fabrication process was made to minimize possible sources of irreproducibility. From this fabrication auditing process, it was noticed that one processing step in particular, deposition of the PFN-Br electron transport layer from a methanol solution, stood out as having significant impact on final device performance. Therefore, a more targeted examination of this step was carried out

to more deeply understand its role in improving device efficiency. By applying dynamic and static methanol solvent annealing treatments, it was observed that the deposition of the PFN-Br/MeOH layer accomplished a dual effect. On one hand, it reduced charge recombination at the cathode interface and on another hand, it induced a wetting effect on the PEDOT:PSS layer, possibly improving this layer's conductivity.

2.3 Approaches to improve reproducibility of PM6:BTP-BO-4Cl solar cells

Among the state of the art bulk heterojunctions with highest reported photovoltaic performance is the PM6:BTP-BO-4Cl blend with published power conversion efficiencies roughly between 15% to <18% [85], [86], [115]. Most recent papers report the combination of the PM6 polymer and non-fullerene acceptors like BTP-BO-4Cl. A trend observed in PM6:Non-fullerene pairings is that research efforts are focused on improving photovoltaic efficiency by tweaking the molecular structure of the acceptor [86], [103], additive content in the blend [116], [117], solvent type [88], or by introducing a ternary component to the binary composition [118].

A common denominator missing in most of these works is a lack of detailed experimental discussion on how the authors achieved such high device performance results, often while maintaining an astonishing degree of reproducibility. The first tests in this thesis work attempted to reproduce a 16% efficiency target based on the recipes reported by Ma et al. [119] and Xu et al. [88]. Unfortunately, the initial results fell far short of the expected values, almost certainly due to the artisanal aspects of device manufacture; therefore, various fabrication steps were isolated to minimize the lack of reproducibility.

The general bulk heterojunction recipe in this work was a 1:1.2 donor:acceptor ratio, 17.6 mg/mL total concentration dissolved in chlorobenzene with a 0.5% v/v amount of DIO additive. Ma et al. reported that full dissolution of the blend occurred upon stirring at 40 °C for 4 h, however, these conditions did not result in a fully dissolved blend and the deposited films showed large fragments of undissolved material, which resulted in poor film quality and uncontrolled concentration conditions. To address this problem, different actions were explored, as shown in Fig 2.7c.

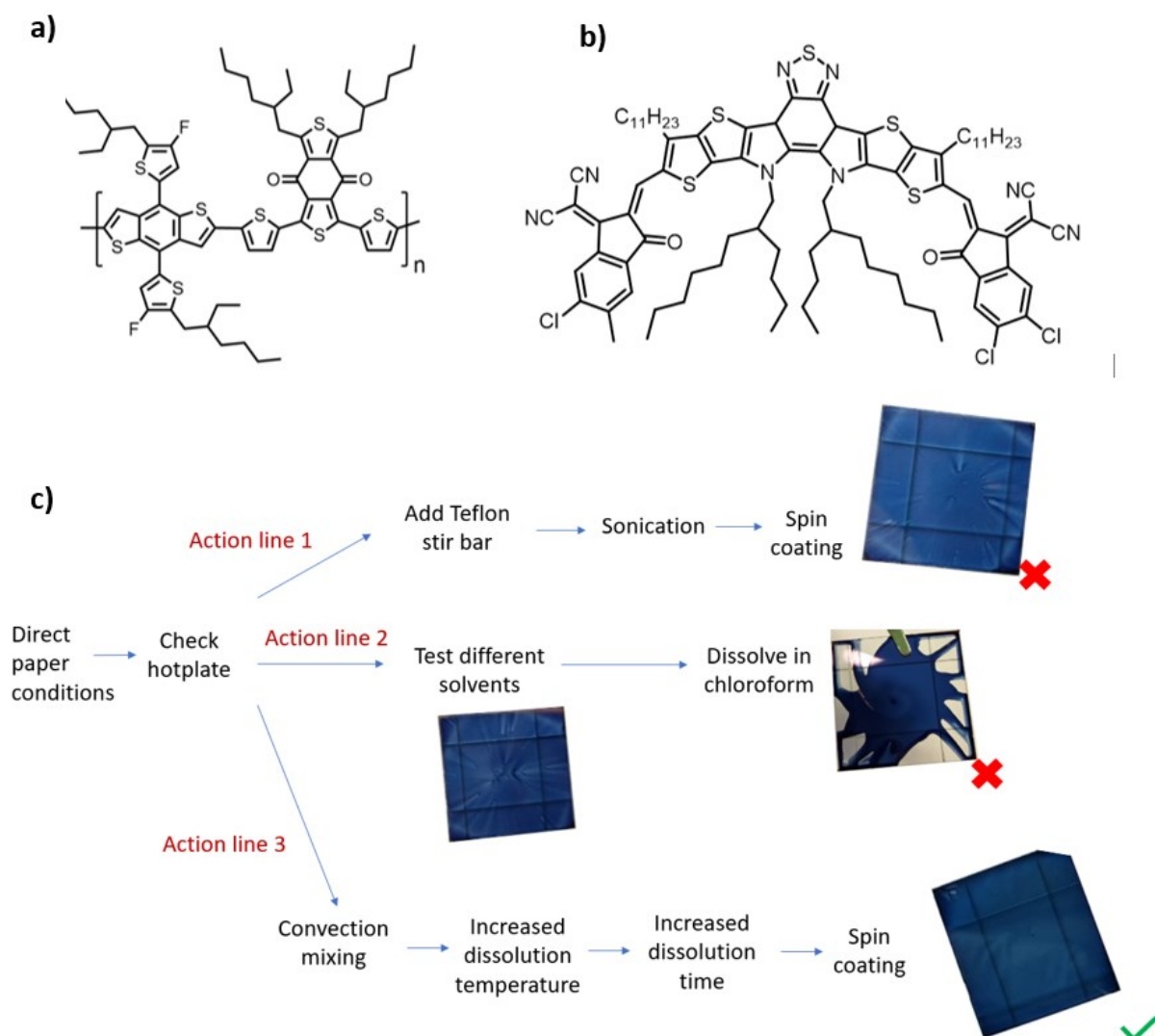


Fig. 2.7: a) Molecular structure of the PM6 donor. b) Molecular structure of the BTP-BO-4Cl acceptor. c) Flowchart of action lines taken to improve dissolution of PM6:BTP-BO-4Cl blend and quality of deposited thin film.

The first line of actions taken to improve the dissolution of the donor and acceptor materials consisted of mechanical approaches; however, these attempts worsened the problem. The introduction of a Teflon stir bar in the dissolution vial caused a ring of undissolved material to form on the upper part of the solution vortex. Sonication caused the bulk heterojunction ink to splash on the walls and cap of the vial, causing some of it to dry and become lost from the rest of the solution, thereby altering the total concentration and possibly the blend ratio. Spin-coated cells

tested by following these actions led to undissolved specks of material in the surface of the deposited thin films.

A second line of action consisted in changing the solvent type used to dissolve the donor and acceptor materials, and it was observed that the donor polymer appeared to be more resistant to dissolution than the small molecule acceptor. The dissolution effectiveness of *o*-xylene, dichlorobenzene, toluene, chloroform, and dichlorobenzene was tested by adding 1 mg of PM6 to 1 mL of each solvent and gently tapping the container vial. From a simple qualitative visual inspection after 1 min of tapping, it was observed that the fastest dissolution occurred with chloroform, followed by chlorobenzene, dichlorobenzene, *o*-xylene, and toluene, with toluene resulting in very poor solubility.

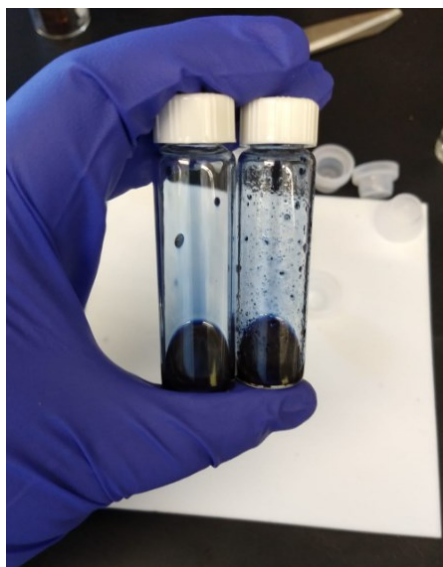


Fig. 2.8 Visual appearance of vials used to qualitatively assess the dissolution of 1 mg of PM6 in 1mL of solvent at room temperature. This picture was taken after 1 min of gentle tapping on the vial. The vial on the left contained chloroform and the vial on the right contained toluene, corresponding to best and worst observed dissolution, respectively, as was observed from the size and number of undissolved specks or clumps of material sticking to the walls of the vial.

Attempts were made to spin-cast films from a BHJ ink prepared in chloroform, however, the solvent evaporated too quickly before uniform coating of the cell could be achieved, as shown by the swirl-like appearance of a deposited film in Fig. 2.7c. Therefore, chlorobenzene was kept as the second best option that balanced dissolution effectiveness and spin-coating processability.

A third line of action consisted of incrementally raising the temperature and dissolution time from the literature recipe of 40 °C for 4 h. No stir bar was introduced, instead, the materials were allowed to dissolve by thermal convection inside the vial. Remarkable improvement in the quality of the deposited film was observed by applying this approach, as shown in Table 2-II.

Table 2-II: Effect of increased dissolution time and temperature on the performance of PM6:BTP-BO-4Cl solar cells

Overnight at 60 °C					Overnight at 80 °C					Overnight at 100 °C				
Spin speed (rpm)	PCE (%)	Jsc (mA/cm ²)	FF (%)	Voc (V)	Spin speed (rpm)	PCE (%)	Jsc (mA/cm ²)	FF (%)	Voc (V)	Spin speed (rpm)	PCE (%)	Jsc (mA/cm ²)	FF (%)	Voc (V)
1000	8.52	24.87	43	0.81	800	9.51	23.87	48	0.83	600	10.08	22.71	53	0.84
1200	8.83	24.38	45	0.80	1200	11.05	23.90	56	0.83	800	13.17	24.32	64	0.84
2000	7.72	22.03	44	0.79	2200	8.32	19.21	54	0.70	1200	13.52	23.32	69	0.85
2200	8.52	25.36	42	0.80	3000	7.86	20.58	48	0.76	2200	12.27	20.13	72	0.85
3000	6.73	19.88	41	0.82	4000	6.37	17.05	47	0.74	3500	10.63	17.65	71	0.85
6000	5.27	20.35	32	0.81	6000	5.75	71.74	47	0.63	6000	12.07	19.84	72	0.85

From Table 2-II it can be seen that by increasing the dissolution temperature, a higher fill factor and a more stable open circuit voltage was achieved, leading to improved power conversion efficiency. The increase in V_{oc} is particularly revealing, as it is related to the morphology and donor:acceptor interface area (directly impacted by the blend ratio) [120]. This value is often used as a fingerprint to determine whether defects have a chemical origin. Wide variations in V_{oc} like those seen when the dissolution temperature was set to 60 and 80 °C are a sign of poor dissolution of the materials which was verified by visual inspection of the deposited films, as can be seen in Fig. 2.9.

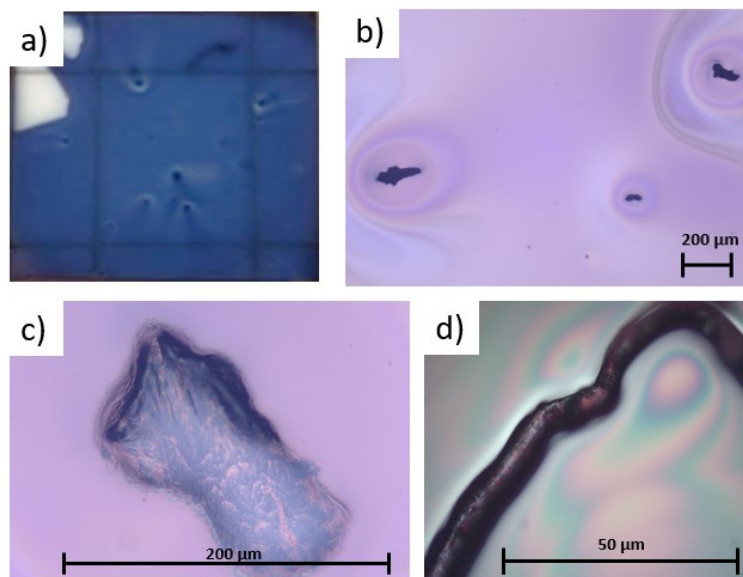


Fig. 2.9: Visual appearance of PM6:BTP-BO-4Cl OPV substrates. a) Image of BHJ layer spin-coated on a glass/ITO/PEDOT:PSS substrate as taken by a cellphone camera, and corresponding b-d) reflectance-mode optical microscopy close-ups where film defects caused by “specks” of undissolved of PM6 polymer are shown.

After increasing the temperature of the dissolution vial to 120 °C and allowing the materials to dissolve overnight, the quality of the deposited film improved significantly and minimal undissolved material remained, as shown in Fig. 2.10. The optimum spin speed for this active layer was 800 rpm, corresponding to a film thickness of approximately 105-108 nm (as measured by an AFM technique).

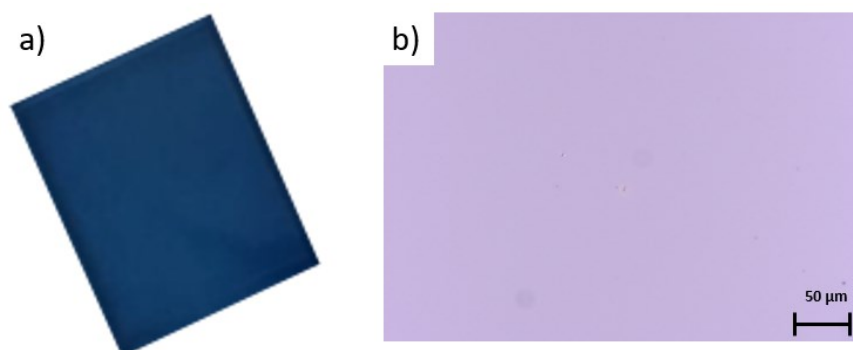


Fig. 2.10: Improved PM6:BTP-BO-4Cl film deposition after overnight dissolution at 120 °C. a) Image of BHJ layer spin-coated on a glass/ITO/PEDOT:PSS substrate as taken by a cellphone camera, and corresponding reflectance-mode optical microscopy close-up.

While the steps in action line 3 led to an improvement in PCE from $\approx 8\%$ to $\approx 13\%$, this was still under the expected $\approx 16\%$ performance reported in the literature. In previous experiments a 2 mL, 5% v/v stock solution of DIO:CB was prepared and stored over the course of days and used as needed in the preparation of a BHJ solution. An aliquot would be taken to be added to the BHJ vial for a 0.5% v/v additive content. However, it was found that to older (in the order of hours) stock solutions corresponded a loss in performance of OPV devices. Therefore, in a refined step, fresh stock solutions were prepared for immediate use during each experiment. It was also found that by adding the DIO from a fresh stock solution 1-2 h prior to spin coating, device efficiency increased. However, these observations were merely observational and thus it was difficult to make any solid conclusions from them.

A final step to improve processability of the bulk heterojunction consisted of allowing the PEDOT:PSS solution deposited on a glass/ITO substrate to thaw for 15 min prior to spin-coating. PEDOT:PSS is normally stored in a refrigerator to improve stability and when spin-coated from a cold solution, wettability problems would sometimes appear which prevented the deposition of a uniform bulk heterojunction layer.

By implementing these actions and by depositing the PFN-Br electron transport layer after thermal annealing (details which will be discussed in a later section), it was possible to finally achieve comparable results to those reported in the literature, as can be seen in Table 2-III.

Table 2-III: Comparability of experimental results to those reported in the literature

Source	Film thickness	PCE (%)	Jsc (mA/cm ²)	FF (%)	Voc (V)
Ma et al. [119]	110 nm	15.7 ± 0.6 (16.5 max)	24.7	76	0.85
Experimental	105 nm	15.6 ± 0.6 (16.4 max)	26.2 ± 0.8	69 ± 1	0.86 ± 0.01

2.4 Methanol treatment of the PM6:BTP-BO-4Cl bulk heterojunction

Up to this point, the quality of the deposited bulk heterojunction film and corresponding photovoltaic efficiency had been controlled by addressing issues in solubility. As was previously mentioned, initial tests did not match those reported in the literature, so various fabrication steps were isolated and tested to explore the extent that each one contributed to (or subtracted from) to processability and photovoltaic performance. The application (and lack thereof) of thermal annealing and the deposition of a PFN-Br layer from a methanol solution were two of those isolated fabrication steps. As will be explained in later sections, the use of the term “thermal annealing” in the literature to describe a thermal treatment step of this PM6:BTP-BO-4Cl bulk heterojunction appears to be imprecise given the lack of morphological or crystallographic changes observed after its application, as experimental data in a later section will show. Therefore, unless otherwise indicated, “thermal drying” will be used as a more precise term to describe the act of placing an OPV substrate on a hotplate for treatment at a certain temperature for a specific amount of time.

It was observed that if thermal drying was not applied prior to the deposition of PFN-Br/MEOH, cracking of the bulk heterojunction film would occur, as shown in Fig. 2.12.



Fig. 2.12: Visual appearance of two glass/ITO/PEDOT:PSS/PM6:BTP-BO-4Cl samples (no thermal treatment) after spin-coating deposition of PFN-Br from a methanol solution.

As was mentioned, reported literature on this blend frequently mentions the necessity of a “thermal annealing” step (understood to be a process that results in a modification of the crystallographic and morphological properties of a material by thermal means). Thus, it was believed that some modification of the bulk heterojunction caused by “annealing” was necessary to prevent film cracking. Observationally, film cracking appeared to be related to the lack of thermal drying step

or methanol spin-coating, therefore, actions were taken to determine which treatment was responsible for this behavior.

A first hypothesis to explain this phenomenon was that methanol was drastically modifying the bulk heterojunction. It is known that some organic semiconductor blends experience molecular reorganization due to thermal or solvent annealing, causing the molecular structure to change and become more orderly and stable [121], [122], [104], [22], [23]. Thus, it was thought that if a polar solvent like methanol was allowed to make contact with the film, perhaps van der Waals forces might cause the dipoles of the donor and acceptor to realign and cause a similar molecular reordering. In this sense, it was hypothesized that direct physical contact of the methanol with the bulk heterojunction might induce a much stronger molecular response than thermal annealing. However, as is discussed in a later section, no measurable change in the morphological features of the PM6:BTP-BO-4Cl blend was observed due to the deposition of PFN-Br/MeOH or by spin-coating methanol on the cell.

To more clearly understand how the photovoltaic metrics were affected by the deposition of PFN-Br and methanol, OPV samples were prepared and characterized in a solar simulator, these results are shown in Table 2-IV.

Table 2-IV: Effect of PFN-Br/MeOH and MeOH treatment on thermally- treated and untreated PM6:BTP-BO-4Cl solar cells

Thermal treatment	Post-deposition	PCE (%)	Jsc (mA/cm²)	FF (%)	Voc (V)	Rsh (kΩ)	Rsr (Ω)	No. devices
Yes	-	8.93 ± 1.40	22.63 ± 3.89	59 ± 4	0.67 ± 0.29	0.68 ± 0.17	3.90 ± 1.34	20
Yes	MeOH	11.66 ± 0.48	22.15 ± 0.59	64 ± 1	0.82 ± 0.44	0.83 ± 0.02	3.42 ± 1.2	5
Yes	PFN-Br/MeOH	15.60 ± 0.57	26.22 ± 0.84	69 ± 1	0.86 ± 0.01	0.72 ± 0.19	2.01 ± 0.49	21
No	-	9.61 ± 1.41	22.39 ± 3.26	60 ± 2	0.72 ± 0.03	0.75 ± 0.17	4.49 ± 1.86	17
No	MeOH	12.97 ± 0.07	22.91 ± 0.20	67 ± 1	0.84 ± 0.01	0.88 ± 0.11	2.57 ± 0.24	4
No	PFN-Br/MeOH	14.45 ± 0.87	24.67 ± 1.46	68 ± 2	0.87 ± 0.01	0.57 ± 0.12	1.92 ± 0.49	18

Thermal treatment consisted in placing the sample on a hotplate for 10 min at 120 °C. Post-deposition refers to the spin-coating of an electron transport layer or MeOH on the BHJ layer. Although the number of devices for the MeOH-only treated cells is low, it was obtained from different batches of solar cells, thus providing a degree of experimental confidence. To prevent film cracking of the samples not thermally treated, they were first dried under vacuum at 1×10^{-5} atm.

A first inspection of the data in Table 2-IV was made to ascertain whether the thermal step resulted in increased photovoltaic efficiency. A seemingly contradictory behavior was observed; samples prepared as-spun showed a PCE efficiency of 9.61% which was reduced to 8.93% after the application of a thermal treatment. However, efficiency increased to 15.6% for thermally-treated samples which then subjected to PFN-Br/MeOH deposition. Samples not thermally-treated but subjected to PFN-Br/MeOH deposition only had an efficiency of 14.45%. Note: it was found that if the samples not thermally-treated were instead subjected to high-vacuum drying at 1×10^{-5} atm, film cracking could be prevented.

While comparability and statistical significance questions are valid in the light of the of the inclusion of a high-vacuum step and the large error interval in the photovoltaic results of Table 2-IV, it is important to recall that at the time it was thought that thermal annealing by definition had to be causing a modification of the morphological properties of the bulk heterojunction and must therefore consistently result in increased photovoltaic performance, contradicting the results in seen in this table.

The results in Table 2-IV led to two burning questions, why was maximum efficiency reached when the thermal step was applied? And why was the application of methanol or PFN-Br/MeOH correlated to a considerable increase in photovoltaic performance.

The hypothesis that methanol must be modifying the bulk heterojunction in some way could not be discarded right away because of the noticeable increase in V_{oc} and FF observed after spin-coating this solvent on the bulk heterojunction. While the lack of an appreciable change in J_{sc} suggested no additional exciton generation, the drop in series resistance and increased shunt resistance after methanol spin-coating indicated improved charge extraction, further strengthening the case that some electronic property was being modified. Moreover, existing literature has reported that that the type of solvent used to process the bulk heterojunction can affect its photovoltaic behavior [123], [124], [120]. Thus, to more precisely discern what effect methanol had on the BHJ, additional characterization techniques other than solar characterization were considered.

A simple qualitative x-ray diffraction test was performed on two OPV samples processed by spin-coating them with PFN-Br/MeOH. One sample was subjected to thermal drying and the other one

was not. From the comparison of both diffractograms, shown in Fig. 2.13, it was concluded the bulk heterojunction in the samples remained amorphous. Hence, this evidence was one indication that neither the thermal nor the methanol treatment promoted molecular reordering (crystallization) of the bulk heterojunction, phenomenon thought to be a possible explanation for the increase photovoltaic performance measured after their application, shown in Table 2-IV.

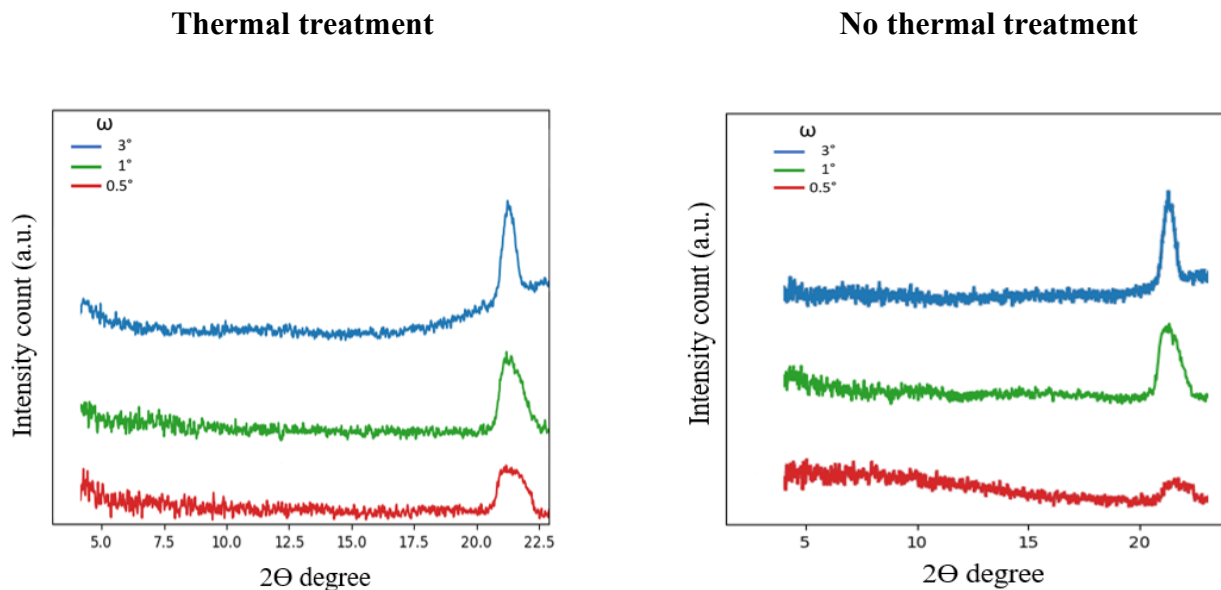


Fig. 2.13: XRD diffractograms showing no apparent change in crystallographic structure between OPV samples thermally- treated and untreated.

In the x-ray experiment, a Cu K α source in a small incidence angle configuration was used. The diffractograms in Fig. 2.13 show a lack of discernable peaks at low 2θ angles ($5-20^\circ$), often a region rich with information for crystalline polymeric materials. The single amorphous peak around 21° may correspond to the (211) reflection of the glass/ITO substrate [125], [126] used to prepare the OPV samples. While a more precise experiment could have developed by preparing the samples on a monocrystalline silicon substrate (to reduce background noise), by increasing the exposure times, reducing step size, and probing a wider 2θ range, this quick result was considered one valuable source of information.

As will be discussed later, additional characterization by tapping-mode AFM, shown in Table VI, also showed no discernable difference between a sample that was thermally treated and two

samples subjected to different methanol treatments. However, a core takeaway from Table IV had been that a methanol treatment correlated to a notable increase in photovoltaic efficiency. The unsolved questions were, if the methanol treatment had no discernible effect on the bulk heterojunction, why was it causing photovoltaic performance to increase? And if the bulk heterojunction was not being modified, what was? Additionally, what was it about this methanol treatment that was causing cracking of the deposited films?

To try to answer these questions, refinements to the methanol treatment were applied. One refinement was attempted by applying dynamic solvent vapor annealing. A computer-controlled solvent vapor annealing system was used to vary the solvent content ratio and exposure time, shown in Fig. 2.14.



Fig. 2.14: Image of the group’s computer-controlled solvent vapor annealing system. A full schematic and detailed explanation of its components is reported by Jin et al. [23].

From this dynamic solvent annealing exploration, it was further observed that a correlation existed between the drying step (thermal or vacuum), the solvent ratio, the amount of solvent exposure, and the emergence of film modifications in the form of “textures”. Moreover, different film textures could be induced by modifying these parameters, as shown in Fig. 2.15.

Note, the term “texture” is used henceforth to describe the visible change in the appearance of the solvent-treated substrates.

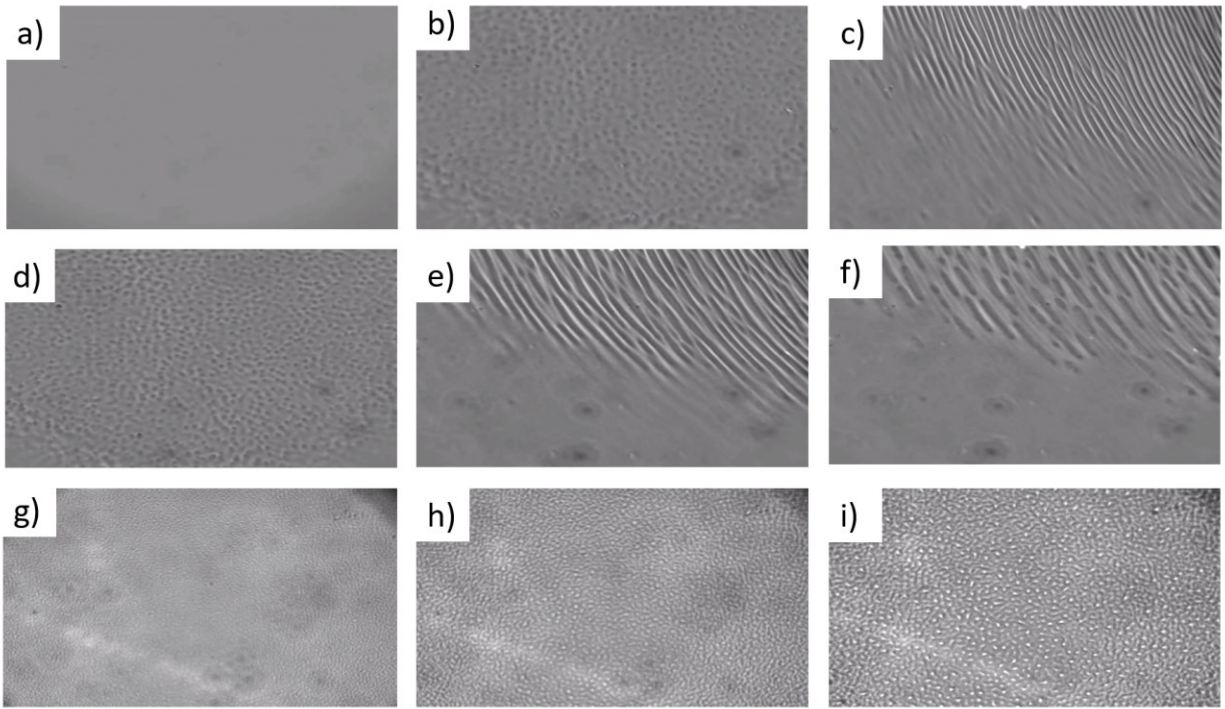


Fig. 2.15: In-situ images of the film evolution of two PM6:BTP-BO-4Cl OPV chips during methanol solvent vapor annealing (the area shown corresponds to a section of roughly 3 mm by 3 mm and was captured by a digital camera coupled to a microscope focusing; the area of the OPV chip was roughly 13 mm x 15 mm; the initial thickness of the BHJ film was approximately 108 nm, the thickness of the PEDOT:PSS layer was 30 nm; solvent ratio was 98%, approximate annealing time was 30 min). a-f) Correspond to surface texture evolution of one OPV chip in a chronological order matching the order of the alphabet. e-f) correspond to the chronological film evolution of a second sample.

A static type of methanol solvent treatment was also applied. In this case, the solvent was allowed to soak the films in liquid form for different times, as is illustrated in Fig. 2.16.

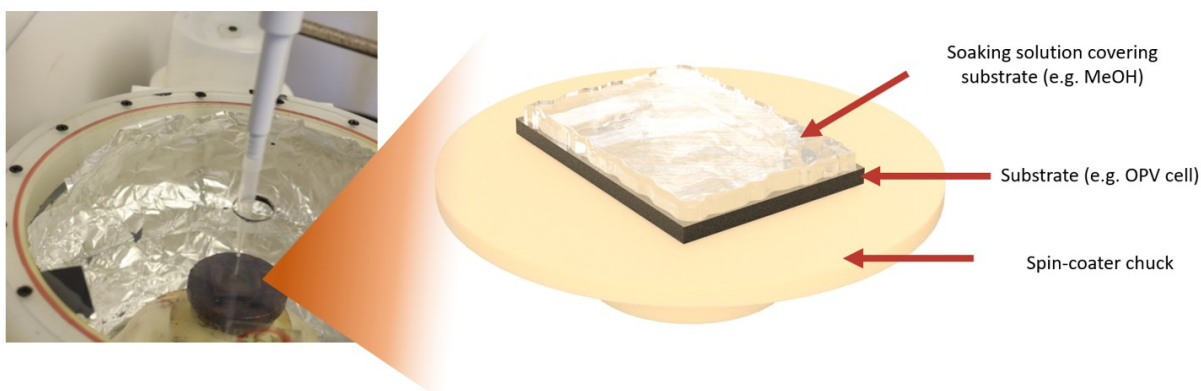


Fig. 2.16: Soaking setup for static solvent annealing. A sample was placed on the spin-coater chuck, covered with a solution and spun-dry after a certain amount of humidification time had passed.

In the following sections, “soaking” treatment is understood to be the action of depositing an amount of solution on a substrate to cover its surface. The substrate was placed on the chuck of a spin-coater so that after a certain amount of time, the soaking solution could be spun off the sample. The terms “flush” or “wash” refer to the action of covering a substrate with a solution and immediately spinning it off.

In this static solvent annealing approach, the OPV substrates were soaked in a solution of 0.5 mg/mL of PFN-Br/MeOH for varied times. This approach considerably correlated to increased PCE when compared to as-spun controls, as shown in Fig. 2.17.

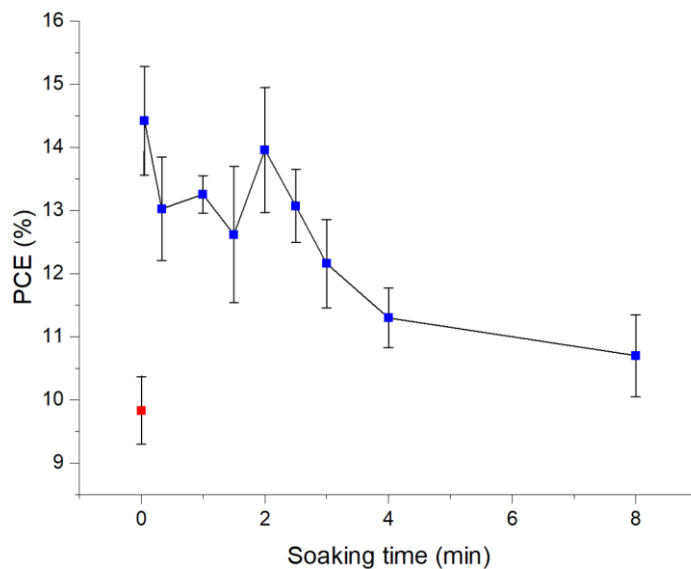


Fig. 2.17: Effect of PFN-Br/MeOH soaking time on PCE of vacuum-dried PM6:BTP-BO-4Cl solar cells. Blue squares correspond to OPV samples subjected to soaking and the red square corresponds to an untreated sample. Error bars correspond to performance values one standard deviation away from the average.

Table 2-V: Effect of PFN-Br/MeOH soaking time on the performance of PM6:BTP-BO-4Cl solar cells

Soaking time	PCE (%)	Jsc (mA/cm ²)	FF (%)	Voc (V)	Rsh (kΩ)	Rsr (Ω)	No. devices
None (as spun)	9.83 ± 0.53	23.71 ± 0.59	57 ± 2	0.72 ± 0.01	0.57 ± 0.17	4.89 ± 0.87	10
3-5 s	14.42 ± 0.86	24.73 ± 1.46	67 ± 2	0.87 ± 0.00	0.56 ± 0.12	1.85 ± 0.49	18
20 s	13.03 ± 0.82	25.43 ± 0.93	59 ± 2	0.87 ± 0.00	0.37 ± 0.02	2.20 ± 0.28	4
1 min	13.25 ± 0.30	24.22 ± 0.39	63 ± 1	0.87 ± 0.01	0.42 ± 0.06	2.08 ± 0.36	4
1.5 min	12.62 ± 1.08	23.53 ± 1.26	62 ± 3	0.87 ± 0.00	0.48 ± 0.13	2.49 ± 1.19	8
2 min	13.96 ± 0.99	24.71 ± 1.23	65 ± 2	0.87 ± 0.00	0.74 ± 0.18	2.32 ± 0.88	18
2.5 min	13.07 ± 0.58	23.22 ± 0.62	65 ± 1	0.87 ± 0.00	0.63 ± 0.11	2.73 ± 0.49	4
3 min	12.16 ± 0.69	23.47 ± 0.58	60 ± 2	0.86 ± 0.03	0.38 ± 0.08	2.09 ± 0.39	8
4 min	11.30 ± 0.47	22.47 ± 0.65	58 ± 1	0.87 ± 0.00	0.41 ± 0.04	2.82 ± 0.86	5
8 min	10.70 ± 0.65	23.28 ± 0.95	53 ± 1	0.87 ± 0.00	0.30 ± 0.02	3.22 ± 0.61	5

No thermal treatment was applied, instead, cells were subjected to vacuum drying at 1×10^{-5} atm prior to soaking.

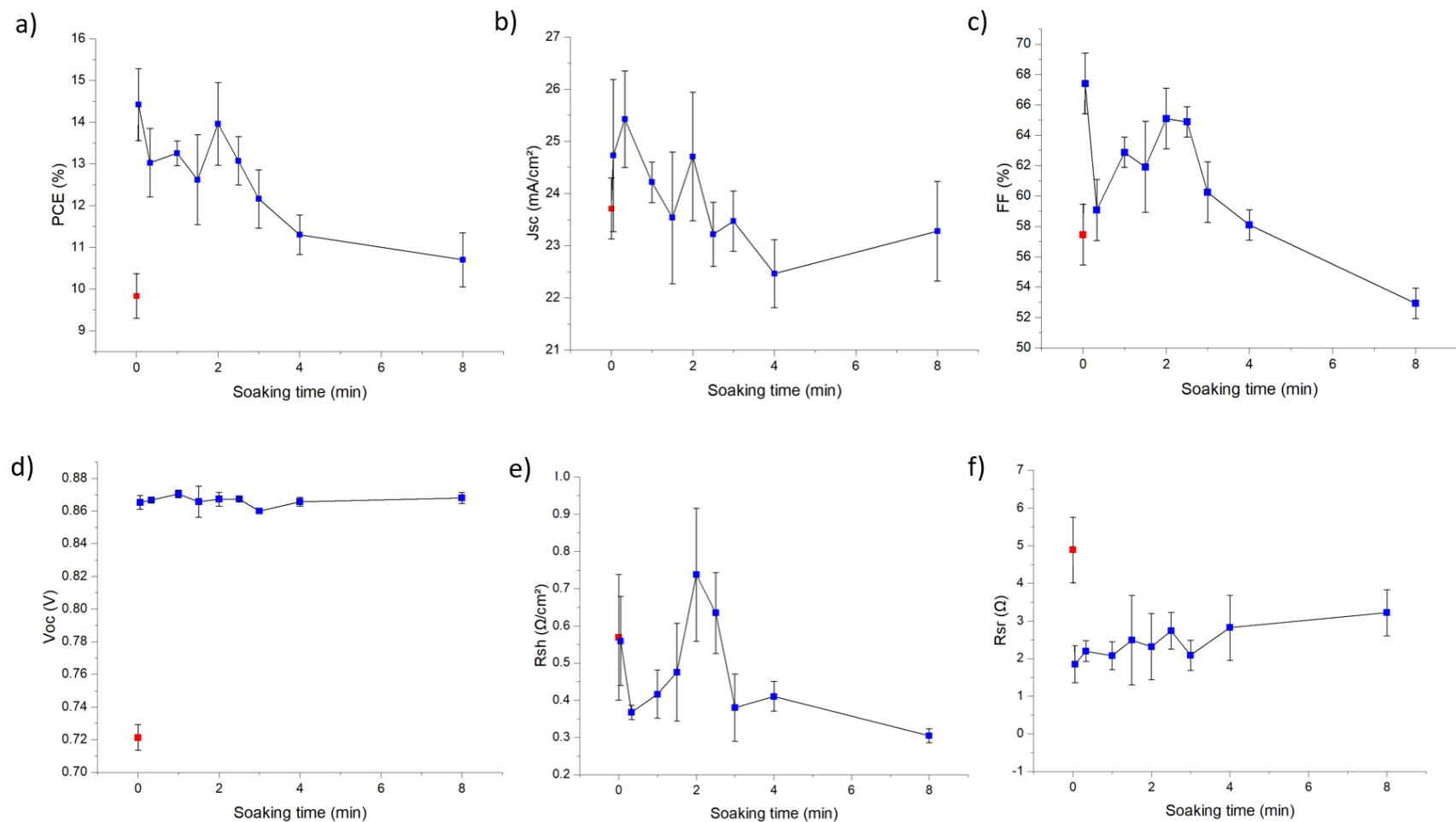
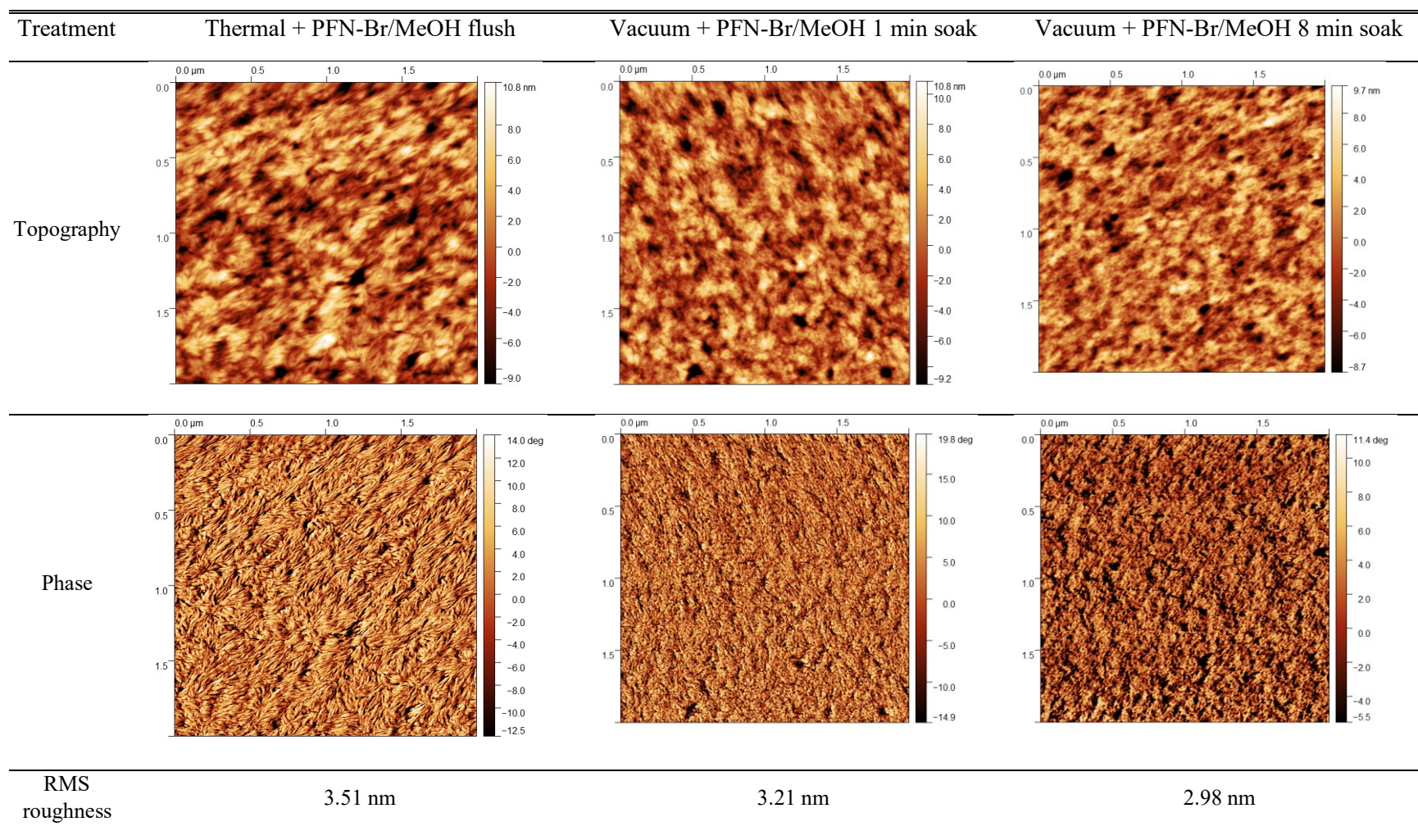


Fig. 2.18: Effect of PFN-Br/MeOH soaking on various solar parameters, a) on power conversion efficiency, b) on short-circuit current, c) on fill factor, d) on open-circuit voltage, e) on shunt resistance, f) on series resistance. Blue squares correspond to averaged response of soaked solar cells and red squares correspond to as-spun cells. Error bars correspond to performance values one standard deviation away from the average.

Table 2-VI: Atomic force micrographs of best performing PM6:BTP-BO-4Cl samples after subjected to thermal drying, soaking in PFN-Br/MeOH for 1 min, and soaking for 8 min.



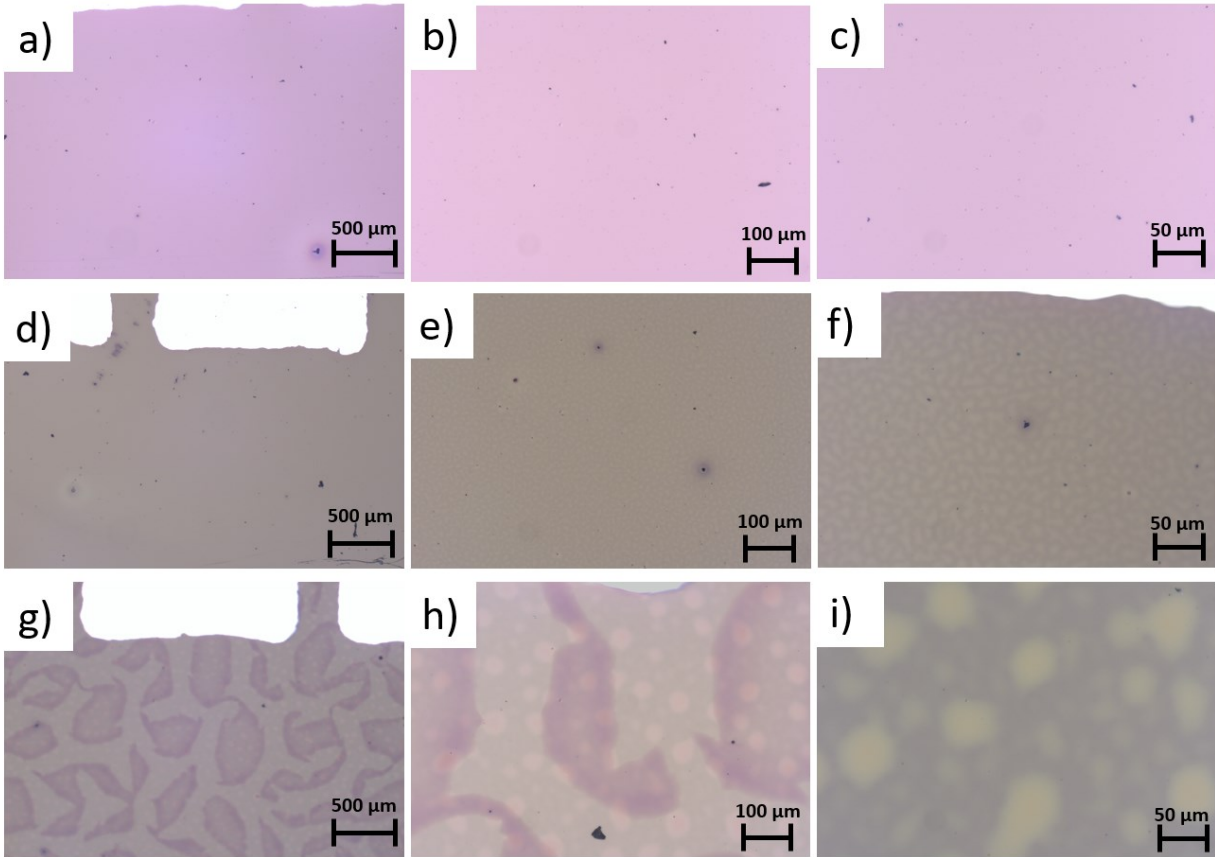


Fig. 2.19: Reflectance-mode optical microscopy images of PM6:BTP-BO-4Cl OPV cells subjected to methanol soaking treatment for different times. Images a-c) correspond to different magnified views of an as-spun OPV cell where no texturing spontaneously occurs. d-f) Images correspond to an OPV cell soaked in PFN-Br/MeOH for 10 s, in this case, fine texturization features begin to form. Images g-i) correspond to an OPV cell soaked in PFN-Br/MeOH for 8 min, in this case, texturization becomes severe.

At this point, the hypothesis that thermal “annealing” played a meaningful role in increased photovoltaic performance by the modification of the morphology of the PM6:BTP-BO-4Cl bulk heterojunction had been dismissed. Instead, the use of the term thermal “annealing” in the literature appeared to refer to a thermal drying treatment, as defined previously.

However, a point of continued “discrepancy” existed between the visible changes in physical appearance observed in samples subjected to a methanol treatment and the information acquired from other characterization techniques (XRD, AFM) which suggested that no modification of the bulk heterojunction was occurring. After all, since the bulk heterojunction was the key layer in driving photovoltaic performance, it was assumed that methanol must be changing its properties in such a way that charge extraction was enhanced, as was manifested from the photovoltaic characterization.

An increase in open circuit voltage from 0.72 V to ≈ 0.87 V was observed in all soaked samples, as shown in Fig. 2.18d. This increase in V_{oc} remained steady despite increased soaking time, suggesting that the possible modification in surface energy caused between the bulk heterojunction and the cathode by the introduction of the PFN-Br layer did not vary considerably once achieved. Moreover, while the introduction of this electron transport layer was expected to play a significant role in improving the photovoltaic properties of the cell.

However, the increase in V_{oc} also occurred by the application of a simple methanol flush, as shown in Table 2-IV. This observation suggested that the role of the PFN-Br layer was to enhance an existing underlying effect correlated to methanol. The decrease in series resistance in Fig. 2.18f, suggested increased electrical conductivity in the cell.

It has been hinted so far in this chapter that although the application of a methanol treatment correlated to increased photovoltaic performance, a causal relationship between the bulk heterojunction and the modification of its morphology derived from the application of a methanol treatment could not be clearly established. Therefore, as additional evidence to discard the possibility that methanol was modifying the chemical character of the bulk heterojunction, an XPS depth profiling test was carried out to determine if the different colors in the textures (brighter and darker regions shown in Fig. 2.19) corresponded to the migration of donor or acceptor material towards the anode (ITO layer) or some form of phase segregation.

In this characterization, the chlorine atoms in the acceptor and the fluorine atoms in the donor were used as elemental trackers, and an argon gas cluster ion beam was used to “drill” through the film so that electron signals at varied depths could be used to quantify elemental content, see Fig. 2.20.

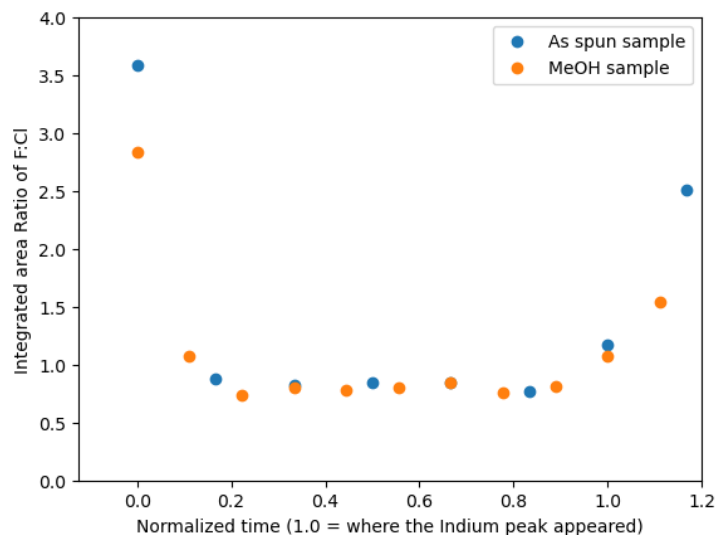


Fig. 2.20: XPS depth profiling of PM6:BTP-BO-4Cl OPV samples. The ratio of F:Cl in the donor and acceptor material, respectively, was used to track possible migration of these materials towards the ITO anode. No PFN-Br was used in this test, the samples were instead prepared as-spun and flushed with methanol.

At first sight, Fig. 2.20 might suggest that a higher content of acceptor material (tracked by the lower fluorine ratio) occurred after treatment with a methanol flush, suggesting a possible explanation for enhanced efficiency attributed to a higher content of the acceptor material towards the cathode, condition known to be beneficial for electron extraction from the polymeric layers into the metal contacts [127]. However, a more careful examination of this figure shows that the content of donor and acceptor is virtually identical in both samples at every other measurement point.

If a higher amount of donor or acceptor had migrated towards the anode, a decrease in its presence throughout the rest of the layer would have been expected as matter must be conserved. While XPS is a very powerful characterization technique, the beam size is not suitable for cm-wide area analysis, thus, multiple additional test points would be needed to more reliably determine whether phase separation took place in other regions of the films. However, because the treated sample was fully covered in methanol, any surface modification would have been expected to occur uniformly and the slightly lower fluorine ratio at the beginning and end measurements of the methanol-treated

sample could be attributable to the beam measuring a section close to the rim of a Voronoi polygon formed by a dewetted film.

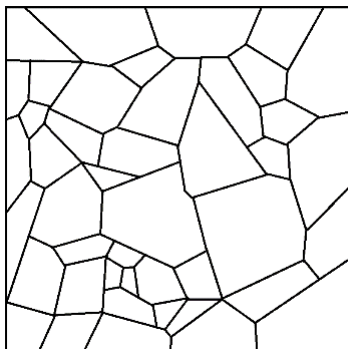


Fig. 2-21: Image of a Voronoi polygon pattern.

From this XPS test, it was reasonably concluded that as XRD and AFM suggested, methanol did not appreciably modify the bulk heterojunction, even if it did affect the solar cell, as was seen from the optical microscopy images.

The ongoing “discrepancy” was resolved by stepping back and reflecting on the bigger picture, that is, an OPV solar cell is more than just the all-important bulk heterojunction. An OPV cell contains multiple layers which also play critical roles in power conversion efficiency. The only other layer in the tandem structure which may be susceptible to drastic modification by methanol was the PEDOT:PSS layer. Therefore, a search in the literature on “methanol effects in OPV cells” was carried out, revealing that methanol has in fact been used as a chemical treatment to increase the conductivity of the PEDOT:PSS layer and to induce dewetting effects [26], [128].

2.4.1 Application of methanol treatments to improve the PEDOT:PSS layer

PEDOT:PSS is a composition of the electrically insulating hydrophilic PSS polymer and the conductive hydrophobic PEDOT polymer. In conventional architecture organic solar cells, PEDOT:PSS is used to prevent indium and oxygen from the ITO anode from diffusing into the active layer, to preferentially allow the transport of holes towards the anode, and to improve the interface contact between the anode and the active layer [26]. In its bonded state, PEDOT:PSS presents a core-shell structure and is solution-processable from water, as is shown in Fig. 2-22.

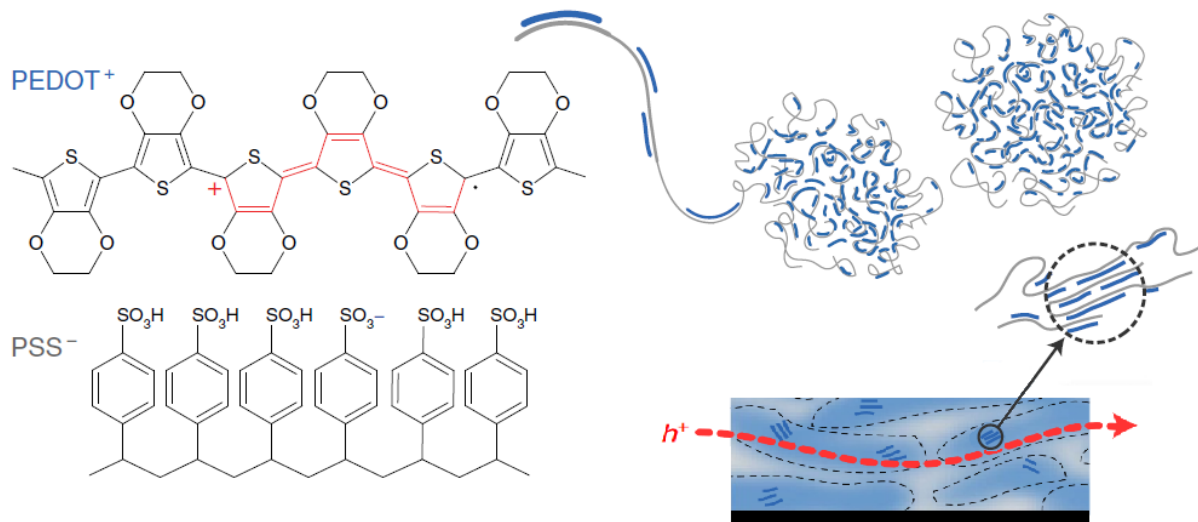


Fig. 2-22: Copolymer microstructure of the PEDOT:PSS system forms a core-shell arrangement. The application of a solvent like methanol on a PEDOT:PSS film can cause the separation of PEDOT from PSS, resulting in PEDOT rich domains (blue) and PSS-rich domains (gray) which create pathways for electronic transport (hole transport) through the conductive PEDOT domains. Reproduced and adapted with permission from CC BY 4.0 open access license [25].

Different authors have reported washing or dipping of this layer in polar solvents like methanol, ethyleneglycol, ethanol, etc. to improve its conductivity [26], [129], [128]. This increased conductivity is explained in terms of a screening effect between the positively charged PEDOT polymeric chains and the negatively charged PSS chains under the presence of a solvent like methanol. The solvent's dipoles are believed to reduce the coulombic interaction between the polymeric chains and the OH groups in methanol are believed to dissolve the hydrophilic PSS, causing a separation between both polymers to take place at the nanoscale [26].

The resulting process is the formation of PEDOT-rich domains with linear structures that are phase segregated from PSS and which provide percolated pathways for improved charge transport [129]. Alemu et al. confirmed that morphological changes in this layer could be induced by the application of a methanol treatment (dipping or dripping). One of their findings was that phase segregation of both polymers resulted in an increase in the conductivity of by three orders of magnitude [26]. Song et al. also confirmed that a methanol-induced modification of PEDOT:PSS also occurred in organic solar cells where the PEDOT:PSS was buried under a bulk heterojunction

layer; specifically, they demonstrated that methanol can permeate the active layer and cause the formation of PEDOT-rich domains with linear and coiled structures [129].

Additionally, Aghassi et al. showed that the amount of water remaining in the PEDOT:PSS film had an impact on how much improvement methanol could induce on the photovoltaic performance of different bulk heterojunctions [130]. According to their observations, the enhanced “methanol effect” was prevalent in freshly made solar cells that used a PEDOT:PSS layer. In contrast, when the cells were dried under vacuum for 12 h or when a MoO₃ hole transport layer was used, very little if any improvement in photovoltaic response could be seen in the bulk heterojunctions exposed to a methanol treatment. His observations are consistent with the high-vacuum step necessary in this thesis work to prevent cracking of the film. In this case, cracking occurred not from the bulk heterojunction but rather, from the PEDOT:PSS layer underneath which simply carried the upper BHJ layer with it.

Based on these reports and from the evidence discussed in earlier sections, it can be concluded that the PM6:BTP-BO-4Cl bulk heterojunction, like many other bulk heterojunctions, is not altered in any discernible way solely as a response to a methanol treatment. Instead, the increase in photovoltaic performance in this blend is likely attributable to the modification of the PEDOT:PSS layer underneath. The increase in power conversion efficiency, current density, and series resistance seen in this work is in agreement with the observations made by other authors who also used PEDOT:PSS and a methanol treatment in the preparation of their samples.

The textures observed in the optical micrographs likely correspond to dewetting of the PEDOT:PSS layer as a response to methanol permeation and evaporation. This would also explain why severe film cracking like the one shown in Fig. 2.12 occurred if the samples were not first thermally dried or vacuum-dried. The more water or solvents left over from spin-coating (or the more water the cells absorbed from the atmosphere during handling), the easier it was for methanol to permeate the PEDOT:PSS layer and induce dewetting.

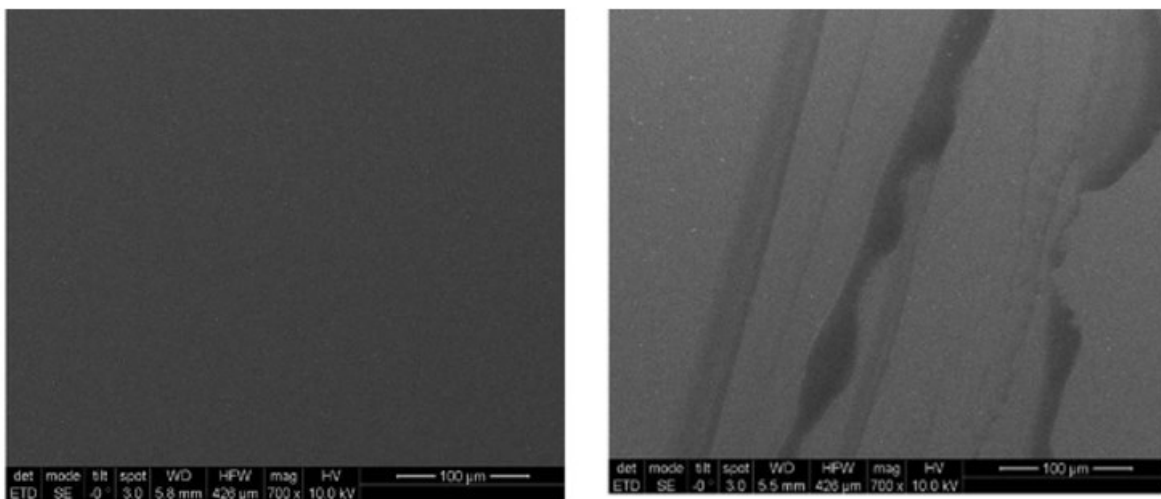


Fig. 2-23: Alemu et al. reported that a methanol immersion treatment caused serrated lines to appear in PEDOT:PSS films, as shown in their SEM micrographs. The right micrograph shows a pristine PEDOT:PSS film and the left micrograph corresponds to film that had been immersed in methanol. Reproduced with permission from Royal Society of Chemistry [26].

In this work, no attempt was made to systematically control the humidity exposure conditions of the solar cell samples other than by the application of a vacuum-drying step or thermal treatment. Future experiments in dehumidified atmosphere like that of a glove box could be carried out to more conclusively prove that the PM6:BTP-BO-4Cl bulk heterojunction is not modified by methanol.

The results in this chapter show how although so much effort and emphasis is placed on designing and optimizing bulk heterojunctions, the importance of other layers should not be ignored. Moreover, this chapter illustrates how an experimentally “innocuous” variable like laboratory humidity or water content in a sample could result in the appearance of correlations in behaviors that are not causal in nature.

This chapter discussed that that methanol is not simply an innocent solvent used to facilitate the deposition of a PFN-Br layer; instead, methanol can modify the PEDOT:PSS. It is the phase segregation of the PEDOT and PSS what causes improved conductivity and ultimately allows for a more efficient charge collection from the bulk heterojunction.

Chapter summary

This chapter opened with a brief on different approaches used to design and optimize organic solar cells. A description of emerging computer-assisted tools in OPV discovery was discussed.

This chapter also examined the fabrication of high efficiency PM6:BTP-BO-4Cl solar cells. The first section addressed different approaches used to improve the quality and uniformity of the deposited bulk heterojunction thin film. From the data gathered, it was confirmed that even small undissolved amounts of donor and acceptor material can have a considerable impact on solar device efficiency. Therefore, when preparing organic solar cells, care should be given to ensure full dissolution of the donor and acceptor materials. Otherwise, batch to batch variances will make any analysis excruciatingly difficult to track.

The second part of this chapter focused on the application of methanol treatments to PM6:BTP-BO-4Cl OPV cells. It was shown that methanol has no discernible effect over the bulk heterojunction. Instead, methanol can modify the PEDOT:PSS layer by causing phase separation of these polymers, resulting in increased conductivity. Additionally, it is thought that the greater content of solvent left over in OPV layers from spin-coating corresponds to greater dewetting effects induced by methanol. Therefore, careful control over the humidity of the OPV layers is important and thermal drying or vacuum-drying are two ways to reduce dewetting.

Chapter 3

Microwave annealing of OPV bulk heterojunctions

“Everyone who has done chemistry in a domestic microwave oven has had some kind of mishap... You have to put in the time to get the conditions right... Too much power and you absolutely obliterate your materials; too little and nothing happens. But once you get it right, you're away.” – Dr. Nicholas Leadbeater [131]

“Those chemists who braved the risks [of microwaving] saw interesting results – usually a phenomenal increase in reaction rate...” David Adam [131]

3.1 A critical stroll through the literature on OPV microwave annealing

There is growing interest in the scientific community in the application of microwaves for chemistry and materials research applications. This is evidenced from a simple Web of Science search for papers containing the keywords “microwave”, “materials”, “chemistry”. Since the early 1980s, the number of annual publications with these keywords has grown considerably from just 4 papers in 1983 to 1,823 papers in 2020. What is driving this growing interest?

A possible answer might be the desire to harness the characteristic ability of microwaves to efficiently transfer energy into a target to rapidly heat it up to hundreds of degrees in seconds. This effect can be achieved in a contactless fashion, with high reproducibility, and with high quality results that can be translated to large-scale production; moreover, microwave heating is being explored in greener chemistry works because of high treatment time efficiency [132], [133], [134]. Rapid heating has been reported to enable synthetic processes to steer towards specific products from multiple possible products or to forego the need for catalysts in certain reactions [131], microwaves have also been used to promote block-copolymer self-assembly [135], to rapidly dry organic materials [136], and to improve the efficiency of organic solar cells, as is the subject of this chapter.

Microwaves are a type of electromagnetic radiation with wavelengths in the range of 10^{-2} to 10^2 m (300 GHz - 300 MHz) [137]. Typically, a 2.45 GHz radiation source is used (in smaller labs, this is often in the form of a household oven). It is generally accepted that two mechanisms drive the conversion of the electromagnetic energy of the microwaves into thermal energy in an irradiated target material: ionic conduction and dipolar polarization [132], [134]. Ionic conduction refers to the response of free charges in a material to the applied electric field; in this case, the charges experience an attractive or repelling force (according to the sign law) that will cause them to move back and forth along a crystal structure or space as a response to the oscillating direction of the electric field. A similar response occurs in the case of dipolar polarization where dipolar molecules will wobble or rotate as they try to align to the applied electric field. In both cases, frictional effects and the increase in kinetic energy are manifested in the form of a higher temperature [138]. This is illustrated in Fig. 3.1, where the response of different objects to an electric field at a time t and t' is shown.

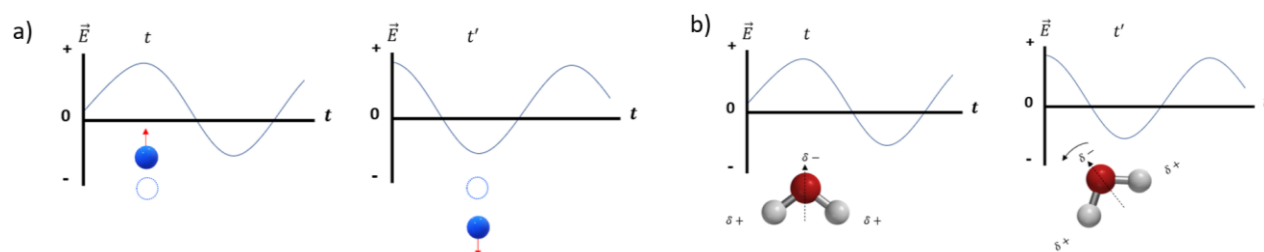


Figure 3.1: a) Ionic conduction motion of a negative charge in response to an external electric field and b) dipolar polarization of a water molecule.

While microwave heating has found utility in many areas of chemistry and materials research [131], [139], [135], an area that has received much less attention is the application of microwave annealing to the optimization of organic photovoltaic solar cells (OPVs). Most OPV devices require some form of thermal annealing treatment as part of their fabrication. This annealing step is performed to optimize the morphology of the bulk heterojunction by inducing a phase separation of donor and acceptor materials into nanodomains within the bulk heterojunction to improve exciton generation and charge harvesting. By far the most common thermal annealing method used in laboratory-scale research is that of traditional hotplate annealing where a solar cell is heated by thermal conduction. This method, while useful, is inefficient and lacking in reproducibility as it is

energy-intensive and does not account for thermal gradients from the point of contact with the substrate and through it. Moreover, the position of the heating elements in a hot-plate and their on/off duty cycle can also negatively impact the reproducibility of large area devices.

In the field of organic solar cells, microwave annealing is a thermal annealing technique that has been studied for roughly 15 years with successful and promising results. Curiously, it has not yet been widely adopted for laboratory-scale OPV optimization or industrial-scale OPV manufacturing. It is possible that this is attributable to the laborious work necessary to configure a reliable annealing setup and the lack of a practical roadmap with “look-outs” and strategies to get started – which is intriguingly, a common denominator missing in most published works. This thesis work sought to dispel some misconceptions and confusion in this area associated with microwave annealing and to provide a detailed guide for future researchers interested in implementing their own microwave experiments.

To our knowledge, the earliest work that discusses the application of microwaves for the optimization of organic solar cells was reported in 2007 by Ko et al. In this work [140], the authors microwave-annealed a regular architecture ITO/PEDOT:PSS/P3HT:PC₆₁BM/Al solar cell. Remarkable improvement was achieved as demonstrated by the increase of J_{sc} from 2.95 to 9.5 mA/cm², FF from 33.8% to 63.5%, and PCE from 0.58% to 3.6% in comparison with as-spun devices. These results are surprising since no electron transport layer was applied. Additionally, the authors attempted to measure the annealing temperature of the various layers in the tandem structure in situ by the application of a fluorescent rhodamine B dye whose intensity varied linearly with the temperature. Although this approach led them to conclude that their 90 s of microwave annealing resulted in a reasonable annealing temperature of 140 °C, which is close to the established optimized hot-plate annealing temperature (\approx 120 – 150 °C) for this BHJ [104], their approach incorrectly led them to believe that no heating occurred due to the ITO substrate. The authors claimed that microwave radiation selectively heated the BHJ with no impact on the ITO or PEDOT:PSS layers. However, as this thesis work will show in later sections from in-situ temperature measurements, it is the ITO layer and not the polymeric layers the primary driver for the microwave heating response. Despite this intriguing observation, this work was key in stirring interest in the field around microwave annealing. To date, this publication is still one of the few

reports where an in-situ temperature measurement is discussed or even attempted. However, virtually no experimental information regarding the microwave configuration was provided.

Other authors were quick to pick up the claim by these authors that microwaves selectively heated the BHJ layer. A paper published in 2009 by Yoshikawa et al. [141] and another one published in 2010 by Flügge et al. [111], attributed the ITO component of P3HT:PCBM solar cells as being primarily responsible for the increased temperature of the solar cell, and not the BHJ. In Yoshikawa’s work, the authors mention that “the temperature of the various samples was directly monitored by digital thermometer through the sight hole during the microwave irradiation” [141] but did not elaborate further on the meaning of this configuration. To a reader, this result might suggest some form of in-situ measurement but since no further details or specifications on the type of thermometer used or its position with respect to the solar cell are provided, this work does not offer a practical guide to reproduce their experiments. Nevertheless, Yoshikawa’s findings are relevant because they show that the PEDOT:PSS and BHJ layers do in fact absorb very little microwave radiation, in contrast to the claims by Ko. et al.

Flügge’s work takes the analysis of heating components one step further by examining Maxwell’s electromagnetic equations and modeling a simple approximation derived from absorption and transmission relationships to propose that the amount of microwave radiation absorbed and converted into thermal energy by a particular layer is dependent on its conductivity. Since nanometric thicknesses are used in OPVs, they assume the irradiated medium thickness to be null and thus, the absorption, a , of a layer to a vertical planar microwave wavefront can be calculated by:

$$a = \frac{2\sqrt{Z_0 R_{\square}}}{Z_0 + 2R_{\square}}$$

where $Z_0=377 \Omega/\text{cm}^2$ is the free space resistance and R_{\square} is assumed as the homogenous sheet resistance of the film. This equation indicates that the more conductive a film is, the greater the amount of microwave radiation that will be reflected [111]. Conversely, higher resistivity materials (e.g. some types of Si wafers) will heat up faster than more conductive materials [135]. This approximation holds true for materials whose sheet resistance is not considerably high; for a pure dielectric ($R_{\square} \rightarrow \infty$) absorption decreases to 0.

Both Flügge and Yoshikawa were able to improve the efficiency of their P3HT:PCBM bulk heterojunctions with microwave annealing close to their standard hotplate controls. In Flügge's report, only 8 s of irradiation were necessary to improve PCE up to 2.59% from 0.03% for the as-spun control. Little difference in efficiency was observed with a corresponding 300 s of conventional hotplate annealing treatment which resulted in a PCE of 2.69%. However, their reported microwave annealing temperature of 216 °C was far above their reported hotplate temperature of 120°C. At such a high temperature, this P3HT blend is expected to experience a drastic drop in efficiency to the 0.0-0.5% PCE range [104]. Therefore, it is likely that Flügge's thermographic camera overshot the real temperature of their substrate. Since a detailed description of their setup is not provided, readers are once again left with an incomplete perspective of how to apply microwave annealing.

Another work that focused specifically on the optimization of BHJs by microwave annealing was the work of Kim et. al. [142]. There, optimizations of P3HT:PCBM and PFT2:PCBM were explored. However, no mention was given to the type of microwave or power setting used. Additionally, no attempt to measure the substrate temperature was performed. Instead, the authors explored the causal relation between microwave time and solar device efficiency. In the case of their P3HT:PCBM blend, a low donor:acceptor total concentration, corresponding to an very thin 80 nm bulk heterojunction layer, might explain their low microwave-optimized efficiency of 1.16% PCE vs 0.59% PCE for the unannealed blend. In the case of their PFT2 composition, an improvement in efficiency from 0.09% to 0.97% PCE was observed after microwave annealing. The optimized microwave time for the P3HT system was 60 s and for the PFT2 system, treatment time was 30 s. For the P3HT blend, the hotplate control efficiency was 1.62% PCE for 600 s of treatment at 120 °C and for the PFT2 blend, a 1.16% PCE for 600 s of treatment at 80 °C. The common denominator in these works is that microwave annealing improved the efficiency of OPV devices at a fraction of time required with conventional hotplate annealing.

In the case of P3HT:PCBM, there is general consensus that the reason for performance improvement after thermal annealing stems from morphological changes induced on the bulk heterojunction, regardless of the source of heat. As annealing is applied, the materials pass the glass transition temperature, the molecules rearrange themselves in more thermodynamically

favorable structures. As larger P3HT nanodomains are formed, more delocalized electrons are available to interact with absorbed light to promote exciton formation [143].

A balance must be struck between the size of the domains because although larger domains generate more excitons, very large domains reduce the available interfacial area for exciton dissociation to take place [71]. As donor and acceptor materials form percolated interpenetrating networks, more excitons dissociate at the interfaces. Afterwards, charge carriers commence a diffusion process through the layered structure of the OPV cell and are collected at the electrodes. Due to the energy level structure of the bulk heterojunction, holes diffuse towards the anode and electrons towards the cathode.

However, while horizontal phase segregation is one factor credited with an improvement in the short circuit current of P3HT:PCBM cells, thermal annealing has also been reported to produce a vertical phase segregation effect [144]. For instance, solvent vapor annealing prior to metal contact deposition is reported to cause PCBM to diffuse towards the cathodes, and a higher acceptor content close to this interface facilitates charge extraction and reduces recombination, boosting efficiency [71]. In contrast, when thermal annealing is applied prior to metal deposit, P3HT tends to diffuse to the top of the bulk heterojunction. Electrons are not as readily transported through the polymer and therefore, a higher concentration of P3HT towards the cathode interface is believed to create trapping sites and increase recombination [71]. Ultimately, it is the summation of all these factors that determines final device efficiency and microwave annealing has been demonstrated to be a technique suitable to promote these morphological changes.

A couple of years after the first papers on microwave optimization of the bulk heterojunction were published came a second wave of microwave annealing papers focused on the optimization of hole transport layers and even the commonly used ITO anode. In 2014 and 2015, Gilissen et al. [134], [27] applied microwave annealing to optimize the PEDOT:PSS layer, finding no appreciable difference in morphology between microwave annealing and hotplate annealing. While in situ measurements of current-voltage were performed for hotplate annealing, no temperature measurement was made for microwave annealing due to the presence of metal contacts. Instead, the authors examined the power to time relationship on the sheet resistance of the ITO. Although microwave-annealed films were slightly less conductive, they closely resembled those prepared by conventional annealing. Additionally, treatment time was reduced from 10 minutes to 30 s.

Also in this paper was a report on the use of a screen printing technique to retain water in the PEDOT:PSS film deposited on glass slides. The objective was to analyze how water remnants could induce heating by microwaving. Their microwave setup included a waveguide apparatus and wave stirrers to prevent the formation of nodes and anti-nodes in any one area of the substrate, thus preventing the formation of standing waves and hot-spots.

Yeom et al. [145] also attempted to microwave anneal the PEDOT:PSS layer but were unsuccessful in controlling the treatment temperature. Although they reasonably claim that due to the high response of water in film, a temperature of 180 °C was reached in 30 s, as measured by a thermographic camera, no attribution for the heating was given to the ITO substrate. Interestingly, their work also applied a microwave treatment to sinter metal contacts deposited from a silver paste. In their work, it is suggested that conductivity of the contacts was improved after 20 s of microwave exposure due to the volatilization of residual carbon between the silver flakes of the deposited metallic contacts.

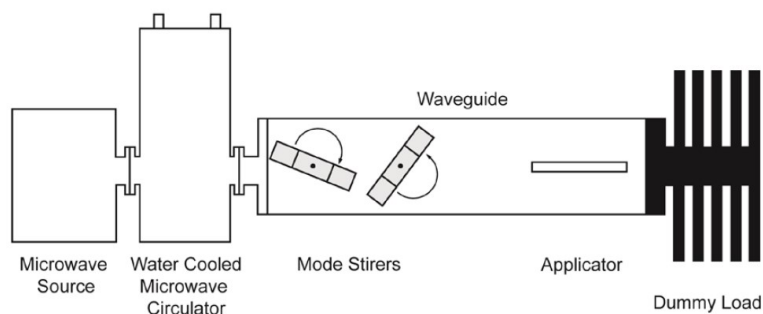


Figure 3.2: A microwave system custom-designed to reduce standing wave hot-spots. Reproduced with permission from IEEE [27].

Also published in 2014 was the article by Vasilopoulou et al. on the improvement of the work function of MoO_x and WO_x hole extraction layers by microwave annealing of inverted-architecture OPVs [146]. In 2015, this same group reported an improvement in PCE from 2.59% to 3.97% for P3HT:PC₇₁BM OPVs whose WO_x layer was microwave-annealed prior to the deposit of the active layer [147]. In 2016, this group also followed up with a publication on additional microwave optimization, finding that by evaporating water trapped in the crystal structure of the MO_x layer, it was possible to achieve better molecular stacking, resulting in an improved fill factor, short

circuit current and ultimately, power conversion efficiency. Additionally, they reported that the dehydration of their substrates by microwave annealing improved storage lifetime of the organic solar cells, with samples retaining 95% of their efficiency after 600 h of storage, contrasting with cells manufactured from PEDOT:PSS which began to lose efficiency virtually immediately after production [148]. Although in this work, an FTO substrate was used, no heating effects were attributed to it.

A more recent publication also by this group was reported on the optimization of the ITO-glass anode by microwave treatment. In their 2017 work [149], microwave irradiation was used as a treatment approach to reducing surface roughness and improve hydrophilicity of the ITO prior to PEDOT:PSS deposition. A comparison of the root-mean-square roughness the ITO was reported, indicating an RMS value of 1.9 nm for microwave and oxygen plasma treatments vs 2.2 nm RMS for as-received ITO. PEDOT:PSS contact angle measurements for the as-received, microwave-, and oxygen plasma- treated samples were 77°, 17°, and 16°, respectively. Their reported P3HT:PC₇₀BM controls showed that this approach was just as effective in improving OPV efficiency as traditional oxygen plasma cleaning with reported OPV PCE reaching 3.54% for microwave treatment, 3.43% for oxygen plasma treatment, and 2.07% for ITO-glass used as received. An improved contact (seen through lower series resistance in treated OPVs) between the ITO and the PEDOT:PSS layer is attributed as a cause for this performance boost. Although the authors do not discuss their microwave setup in detail, other than to mention that a microwave oven was used at a power setting of 450 W, it may be inferred that no controlled atmosphere was used to achieve these results. Moreover, their microwave approach only required 60 s of treatment vs 10 min of oxygen plasma [149].

Shin et al. also explored annealing treatments of ITO films [150]. Their comparison of conventional, rapid heating, and microwave annealing revealed that heating promotes crystallization of the ITO, as determined by the appearance of several x-ray diffraction peaks after the treatment. This change in structure was accompanied by a slight improvement in optical transmittance from 87.2% (untreated sample) to 89.7% (microwave-treated). Despite an increase in surface roughness after the microwave treatment, a reduction in sheet resistance was noticed, going from $1.72 \times 10^3 \text{ } \Omega/\text{cm}^2$ to $4 \times 10^2 \text{ } \Omega/\text{cm}^2$ for unannealed and annealed samples, respectively. The authors reported that the power consumption of a conventional thermal annealing method was

776 Wh to 160 Wh for rapid thermal annealing, to 114 Wh for microwave annealing. The optimized microwave conditions were reported as 2.5 min at 250 W.

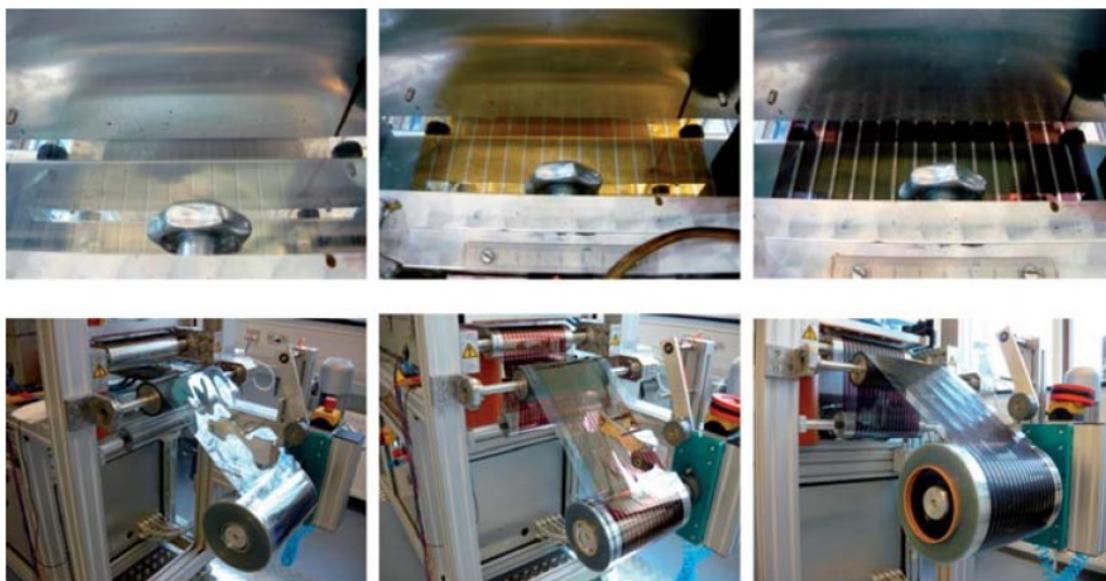
In 2018 Huang et al. reported on the thermal annealing of a ZnO hole transport layer which resulted in PCE boosts from 3.23% to 3.93% and from 7.34% to 8.23% for P3HT:PC₆₁BM and P7BT:PC₇₁BM compositions, respectively [151]. An improved surface smoothness and interfacial contact were achieved in the ZnO film after microwave treatment, thus leading to the improved efficiency. A highlight of this work is the time saved on the film treatment. Whereas conventional hot-plate annealing required a treatment of 200 ° C for 60 min, microwave annealing only required 9 min of treatment. The authors did not report the temperature of their substrate, only a microwave operating power of 65 W.

While technical questions remain around microwave annealing, including how to accurately measure substrate temperatures, how to calculate microwave irradiance absorbed through the layers, how to prevent standing waves from causing hotspots, how to standardize annealing conditions between different commercial microwaves, etc. clearly microwave annealing has shown potential as a technique to improve the efficiency and properties of organic solar cells. Microwave annealing has important advantages over conventional annealing and it could become an all-round technique to optimize OPVs in all stages of the manufacturing process, from conductive substrate preparation to the hole transport layer deposit to the bulk heterojunction annealing, and even the metal contact optimization. Existing microwave annealing efforts have achieved results very close results to those reported by conventional thermal annealing, in some cases with slight underperformance and in some cases with slight improvement, but often within a reasonable margin of error and not of considerable statistical significance. Thus, these techniques are comparable, but an enduring trend is the considerable reduction in annealing time from hours to seconds by the implementation of microwave annealing while reducing instrumental power consumption.

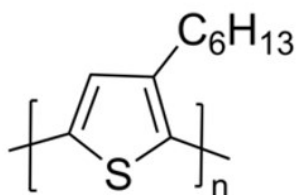
Aside from the potential that microwave annealing has in expediting and pushing laboratory-scale research, it could become an important component of mass-production systems where short processing times and low manufacturing costs are central to successful commercialization. In roll-to-roll systems where the total processing time of OPV modules is targeted to be in the order of seconds [6], [28] microwaves offer an annealing solution with very short start-up and shut-down

times. Additionally, since the majority of large-scale OPV manufacturing techniques (slot-die printing, roll-to-roll printing, etc.) are based on solution-processing of organic inks from water and solvents, microwaves could further assist in the dehydration and drying process which is crucial to cell stability [152], [153]. The industrial-scale potential to reduce manufacturing times and energy costs associated to the annealing treatment of each layer, from minutes and hours to seconds would considerably improve the prospects of mass commercialization of this solar technology.

a)



b)



c)

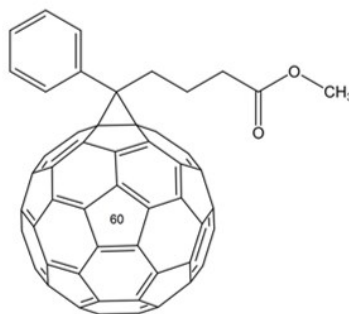


Fig. 3.3: a) A roll-to-roll assembly system. To the left is shown a ZnO slot-die deposition module, on the center a P3HT:PCBM deposition module, and on the right a PEDOT:PSS deposition module. Meters-long flexible films can be quickly manufactured using this system. Reproduced with permission from Royal Society of Chemistry [28]. b) Molecular structure of the P3HT donor, c) Molecular structure of the PC₆₁BM acceptor.

3.2 Chapter results overview

The first part of this chapter addresses the refinement of different microwave annealing configurations based around a simple household microwave coupled to an in-situ fiber optic thermometer probe. Detailed descriptions are given of the implemented procedure to assist readers in setting up a similar cost-effective research system. Various bulk heterojunctions were used during various calibration stages to ascertain with greater certainty whether the effects seen depended or not on a particular type of composition used. Particular emphasis is placed on the P3HT:PC₆₁BM system due low cost, well-known annealing behavior, and its easily visible color variation response to annealing temperature and.

The second part of this chapter addresses the application of microwave annealing for the optimization of the all small-molecule ZR1:BTP-BO-4Cl bulk heterojunction. Characterization of the optimized samples showed an excellent response to thermal annealing, resulting in a 4.6x improvement in power conversion efficiency from 1.56% to 7.28%. No significant difference in optimized efficiency was seen between microwave annealing and a comparable hotplate annealing approach.

3.3 Rational optimization of a microwave annealing setup

One of the greatest challenges in the application of microwave annealing lies in configuring a system that uniformly heats a substrate and that prevents wave node and anti-node hot-spots from forming along its surface. As was discussed earlier, some researchers have built custom-designed systems equipped with waveguides and radiation stirrers to produce planar wavefronts to anneal their OPV cells. However, specialized microwave equipment is not always available in most small research labs. A considerable part of existing microwave applications in general chemistry literature and in the field of OPVs rely on the use of domestic microwave ovens but in most works, very little if any description is given of the approach used by the authors to microwave their targets.

Particularly in the field of OPV microwave-annealing, there seems to be a void with regard to a “microwave annealing troubleshooting” or a guide on “how to microwave” effectively and reproducibly using a household oven to take advantage of this technique. Many microwave papers

seem to be unaware or unwilling to discuss the challenges of annealing in a domestic oven, potentially burdening experimentalists with the necessity to “re-invent the wheel” over and over or worse, leaving them unable to reproduce reported results. Moreover, virtually all works on microwave annealing of the bulk heterojunction that have been reported have been on the well-known P3HT:PCBM blend, which has been around for close to 20 years. This work sought to fill these apparent gaps by evaluating different annealing configurations and applying microwave annealing treatment to more recently reported, high efficiency ZR1 and BTP-BO-4Cl small molecule semiconductors. Specific details on OPV fabrication steps, instrumentation, and materials are described in the Materials and Substrate Preparation section of this thesis.

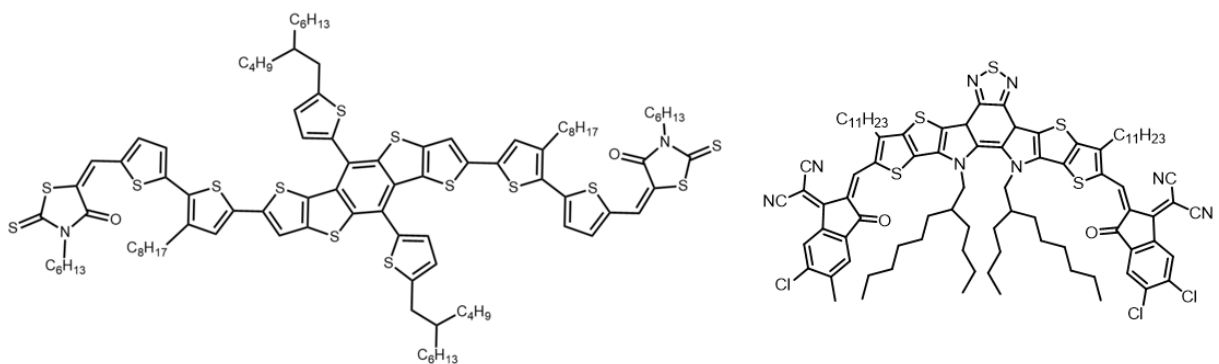


Fig. 3.4 Molecular structure of ZR1 donor (right) and of BTP-BO-4Cl acceptor (left).

3.3.1 Evaluation of different microwave annealing configurations

The first microwave configurations of this work were inspired by a previous report on block-copolymer self-assembly by our group [135]. In that work, a domestic microwave oven was used as a microwave source. A Teflon vessel was used to house the substrates during the annealing process. Overall annealing temperature range was controlled by adjusting the oven’s power levels, annealing time, and by varying the mass of SiC in a mortar, which served to absorb radiation and prevent microwave burn-out. A microwave-compatible fiber optic thermal probe was used for in-situ substrate temperature measurements during calibration runs.

Using that work as a starting point, three initial microwave configurations were tested in this work and are shown in in Fig. 3.5. Target OPV samples were prepared by spin-coating organic semiconductor layers onto a plasma-cleaned glass-ITO, as described in the materials and substrate preparation section. Unless otherwise indicated, an “OPV chip” or an “OPV cell” consisted of a regular architecture glass/ITO/PEDOT:PSS/BHJ architecture/ETL/Al/Mg layer structure.

While early microwave experiments were performed with a Type I configuration, it was noticed that this configuration led to unreliable results, as is described in the following section. Therefore, trial-and-error refinements were made to the annealing setup until settling with the Type IV configuration. No rotatory glass base was used as the base as the plate absorbed too much energy and the in-situ thermometer probe had to remain static in most conditions. Additionally, substrate rotation resulted in sample cracking or melting in only a few seconds. Note that during the entire process, the microwave door was closed to prevent radiation from escaping the chamber.

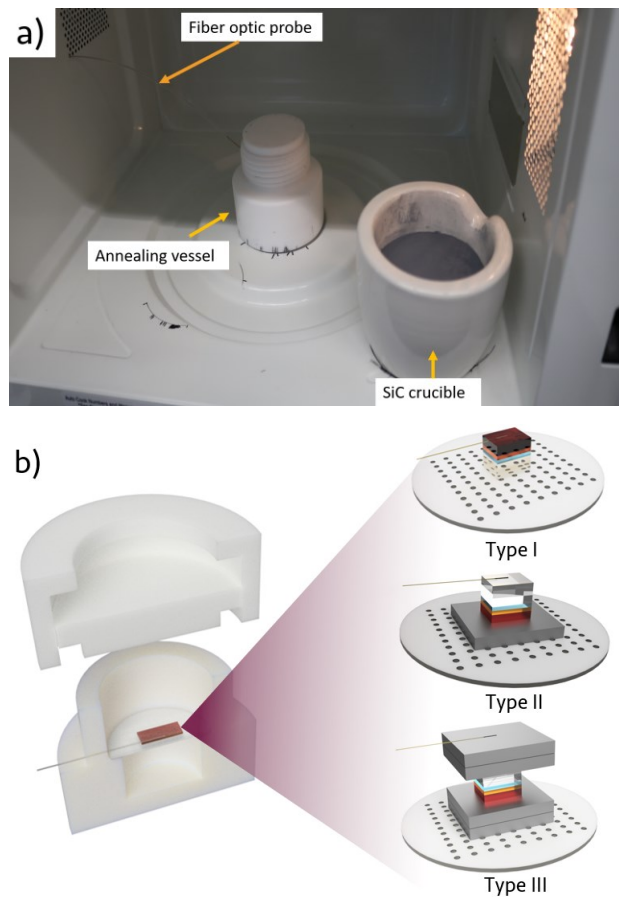


Fig. 3.5: a) Position of Teflon vessel and crucible in the microwave (upper lid removed for insertion of in-situ thermometer probe). b) Three initial microwave annealing configurations used during screening calibration experiments. Type I: the OPV chip is placed upright and the thermometer probe is in contact with the BHJ, Type II: The OPV chip is placed upside down with the BHJ making contact with a Si heating element while the probe is in contact with the glass side of the chip, Type III: a pair of silicon heating elements are placed on the top and on the bottom of the OPV chip forming a sandwich structure, the chip itself is placed upside down and the thermal probe is in contact with the uppermost heating element.

Because it is known that in a domestic microwave resonance in the metallic cavity leads to the formation of standing waves and regions of constructive and destructive interference (antinodes and nodes) which result in hot-spots, it was important to avoid annealing a sample at the interface edge between these regions. Moreover, it was important to place the sample in a position of

constructive interference to fully take advantage of the energy carried by the microwaves. Therefore, a simple thermogram of the oven cavity, inspired by the work of Vollmer [137] was obtained by placing a cardboard square at the approximate height where the OPV chip would anneal inside the Teflon vessel. Running the microwave for 5 s at the maximum power setting was sufficient to avoid combustion and to obtain a clear false-color temperature profile, see Fig. 3.6.

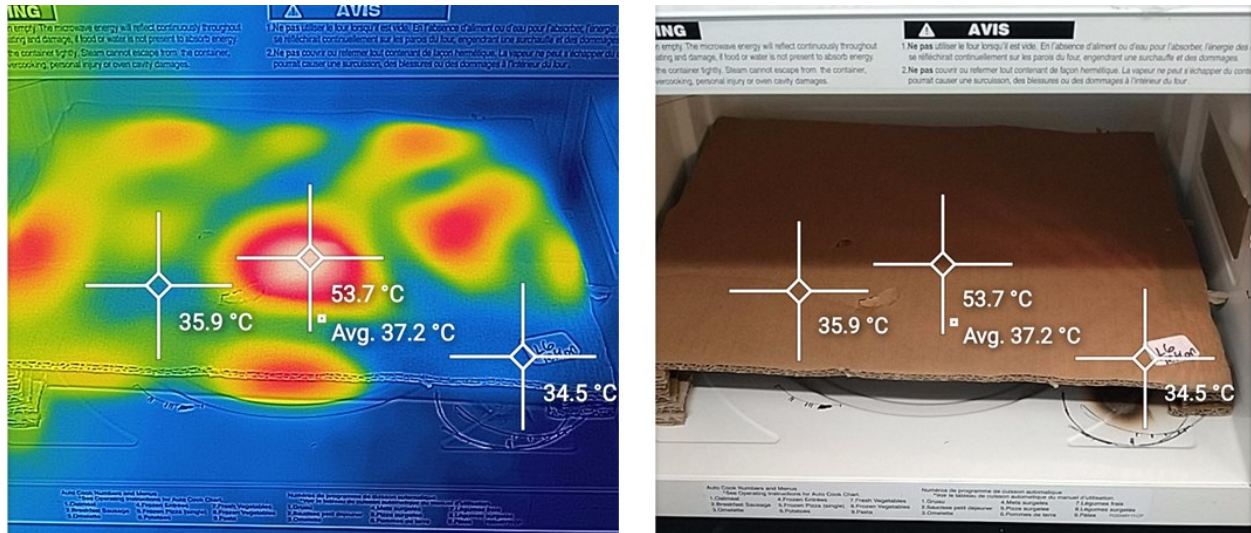


Fig. 3.6: Thermal profile of the microwave cavity. The highest microwave antinode was located at the center of the cavity; hence, the Teflon vessel was placed in that position to take advantage of the constructive interference.

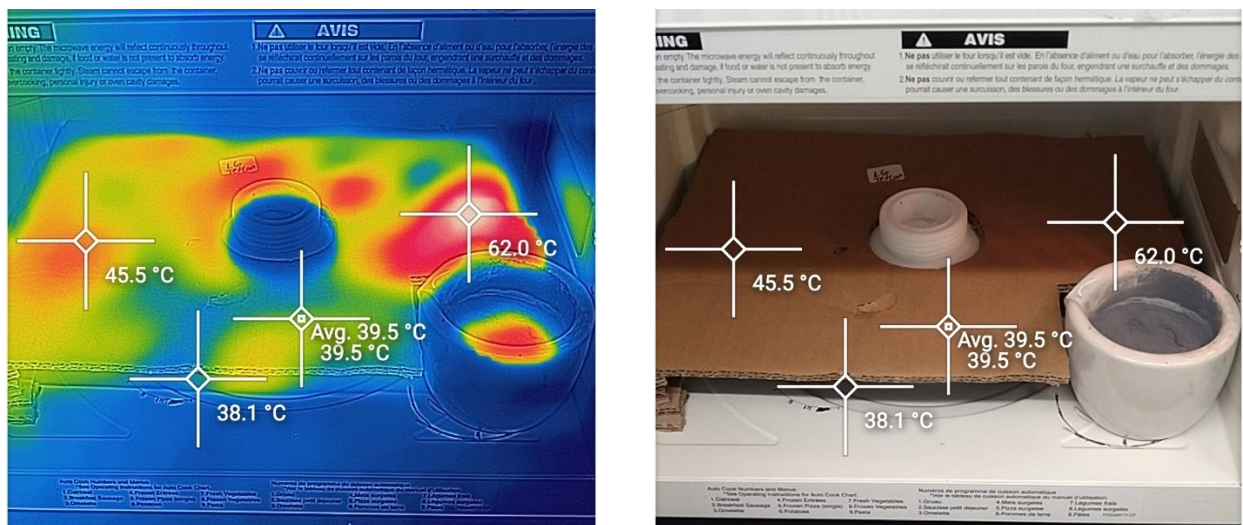


Fig. 3.7: Thermal profile of the cavity after the introduction of the Teflon vessel and SiC crucible. The cooler central region of the thermogram likely occurred because Teflon has a high degree of transparency to microwaves, therefore little microwave absorption took place in that position.

Because the position of the control crucible alters the wave resonance profile of the chamber, its location inside the oven was fixed during the entire project. The addition or removal of the SiC powder was done by taking small scoops and gently tapping the sides of the crucible to flatten the remaining powder. Generally, increments of 1-2 g of SiC resulted in a temperature increase of 5-15° C (for a fixed time and a medium power setting). However, this behavior was not completely linear as sudden spikes of 20-50° C were randomly observed after removing a gram or less of SiC once a critical amount had been taken. In other cases, a mass variation of up to 15 g was required to see any major change in the substrate temperature. One possible reason for this random behavior is believed to be caused by changes in the dielectric constant of the absorbing materials (SiC and working substrate) corresponding to increased temperature [137] after running the microwave oven for an extended time. To reduce this possible source of variance in radiation absorption due to thermal effects, a forced cooling step was implemented after each annealing run to lower the temperature of the Teflon vessel (and any contents inside, when applicable) to 20 °C \pm 3 °C. The temperature in the SiC in the crucible was roughly kept between 20-30 ° C throughout the workday, as measured with an IR thermometer gun.

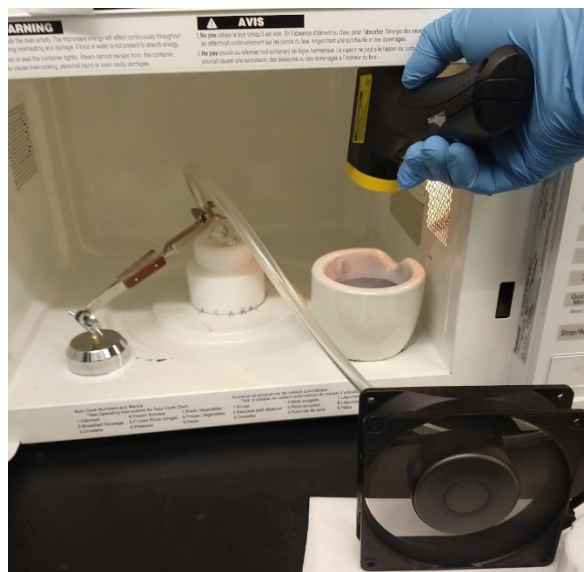


Fig. 3.8: Forced cooling setup. A N₂ exhaust line was placed over the Teflon vessel for rapid cooling of substrates and a fan was used to cool down the SiC crucible.

3.3.2 Type I configuration

As an initial screening step, various substrates were heated for different times at a fixed medium power setting (PWR 6) in a continuous microwave mode, using a Type I configuration, see Fig. 3.5b. From these tests, a plot of the relationship between time and temperature was obtained showing that ITO was the primary driver of substrate heating, with organic semiconductor layers playing a minor role in the absorption of radiation and its conversion into thermal energy.

Although the data appears to follow a composition of linear and natural logarithmic functions, a simple linear fit was chosen to extrapolate the number of seconds required to reach a target temperature. Moreover, the linear slope provided a quick estimate of the temperature resolution as a function of the power setting and annealing time. Higher power settings implied a higher slope and hence, lower temperature resolution. Target temperature and resolution at various power settings could also be fine-tuned by adjusting the amount of SiC in the crucible.

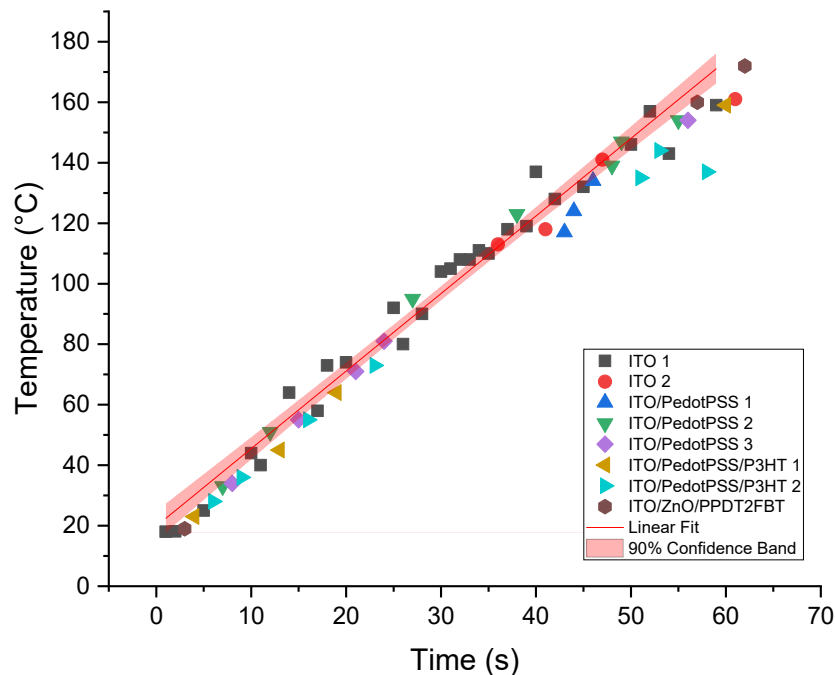


Fig. 3.9: Calibration ramp of microwave annealing time vs maximum substrate temperature. Multiple substrate configurations (glass/ITO, glass/ITO/PEDOT:PSS, glass/ITO/PEDOT:PSS/BHJ, glass/ITO/ZnO/BHJ layer structures) were used to confirm that neither the number or content of the layers caused a thermal response discernably different from simple glass/ITO controls.

The linear fit for the Type I configuration referenced in Fig. 3.9 was determined as:

$$T = 2.46 \frac{^{\circ}\text{C}}{\text{s}} + 19.7 \text{ }^{\circ}\text{C}$$

It is important to note that this seemingly linear regime could collapse and give way to sharp exponential spikes after a critical temperature was reached. This exponential rise could occur by increasing the annealing time as little as 3 s from the unknown critical temperature, so care should be placed when measuring calibration ramps.

As was mentioned earlier, the optimum thermal annealing treatment for the P3HT:PCBM bulk heterojunction has been reported to approximately be 150 °C for 10 min. In this work, two microwave operation modes were examined to achieve this temperature, “continuous” and “instant” microwave generation, as allowed by the built-in functions of the oven, as shown in Figs. 3.10 and 3.11.

As a starting point in this project, an initial objective had been to compare microwave and hotplate annealing treatments as faithfully as possible. Maintaining a substrate at the target thermal annealing temperature for an optimum amount of time was believed to be necessary to provide the active layer with sufficient time for self-assembly of donor and acceptor domains. However, because continuous microwave irradiation causes a constant increase in the substrate temperature, maintaining the annealing temperature constant for an extended period of time could only be achieved by applying pulsed microwave runs. Two options for pulsed microwaves were possible in the domestic oven, an “instant” mode and a “continuous” mode.

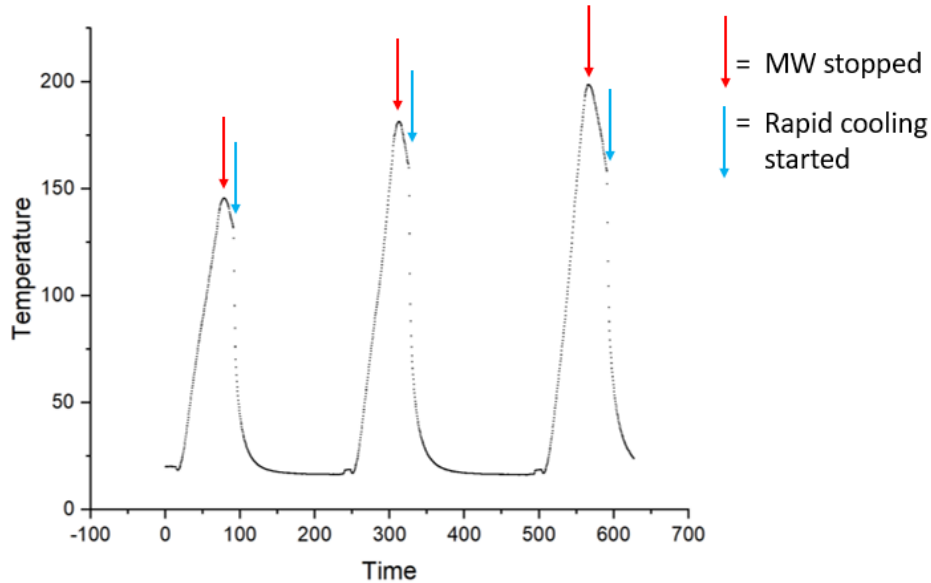


Fig. 3.10: Consecutive heating and cooling cycles of a P3HT:PCBM solar cell, microwave (MW) annealing time was fixed at 56 s at a medium power setting (microwave option PWR 6).

In the “instant” mode, a fixed power setting and number of seconds required to reach the target temperature was selected. After execution, the substrate was cooled down to room temperature and was reheated using the same settings as in the first run, as attempted in Fig. 3.10. Thus, “extended” annealing times could be reached by adding the multiple time intervals (runs) when the substrate reached the target temperature. However, it was observed that after the first annealing run, subsequent runs on the same substrate, with the same power and time parameters, and no change in its position resulted in a higher final temperature. This might be due a modification of the dielectric properties of ITO and the polymeric layers which causes changes in microwave absorbance [135]. This behavior was very problematic excessive heating causes a degradation of the organic materials and thus, results in a significant drop in power conversion efficiency. Because this changing temperature behavior could not be controlled, another operation mode was explored.

In the “continuous” mode, (oven setting: PWR 1), the microwave oven cycled between on and off states at a fixed output power. By running this duty cycle, energy was absorbed and dissipated by the substrate, keeping it hot within a temperature range that averaged to a mean “convergence” temperature. Thus, it was possible to anneal a substrate at a relatively steady mean temperature for

prolonged times, as shown in Fig. 3.11. The “convergence” temperature could be adjusted by varying the amount of SiC in the crucible.

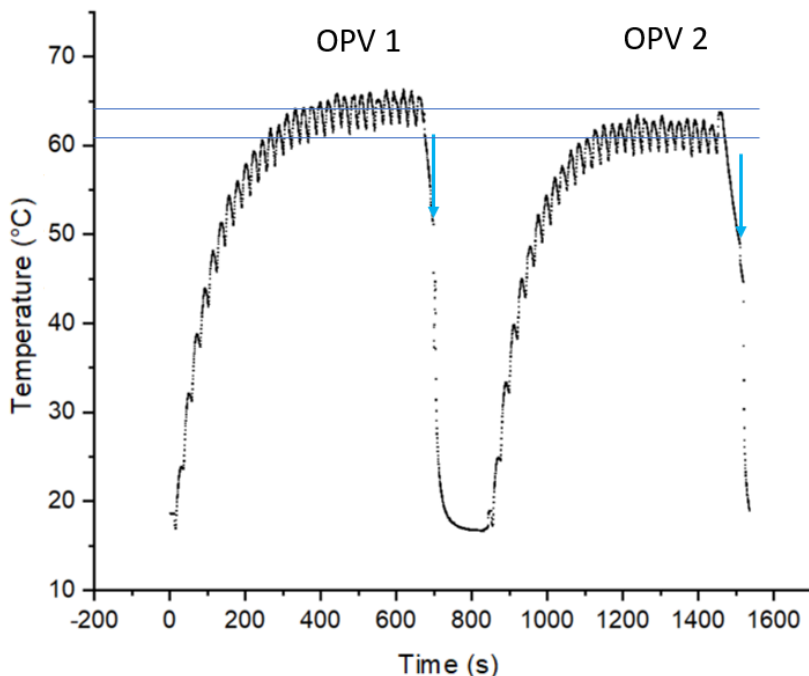


Fig. 3.11: Continuous microwave annealing of two P3HT:PCBM OPV chips. Convergence temperature is denoted by the blue lines. Target convergence temperature in this screening was 60 °C and was set by varying the SiC mass. Variance from target temperature was roughly ± 7 °C.

The earliest calibration runs for P3HT:PCBM in this work were performed at low temperatures (60 – 100 °C) to reduce the time needed to cool down the system to make adjustments. Once an apparently reliable temperature control procedure was established, the convergence temperature was increased to 150 °C to treat this bulk heterojunction. Up to this point, the in-situ thermometer probe had been a constant component of the experimental setup as it was crucial to determine the temperature of the samples exposed to microwaves. However, its presence prevented the Teflon vessel from being sealed with an inert atmosphere during annealing, a necessary step to prevent drops in efficiency from annealing in an air atmosphere.

While annealing temperatures remained below 100 °C, the annealed the bulk heterojunction appeared uniformly colored. However, as the temperature was increased to 150 °C, a non-uniform

coloration appeared around the edges of the OPV substrates, as shown in Fig. 3.12a for both the “instantaneous” and “continuous” modes. From previous solvent vapor annealing experience it was known that for P3HT:PCBM blend, a darker maroon-color appearance was usually indicative of higher device performance. In the case of thermal annealing, an annealing temperature above 150 °C caused a lighter visual appearance of the bulk heterojunction and a lowering of performance.

To discard the possibility that the thermometer probe might have a scattering or a thermal absorption effect along the edges of the substrate, two OPV chips were placed side by side, allowing one chip to maintain contact with the probe (as a temperature proxy) while the other one was unperturbed, see Fig. 3.12b.

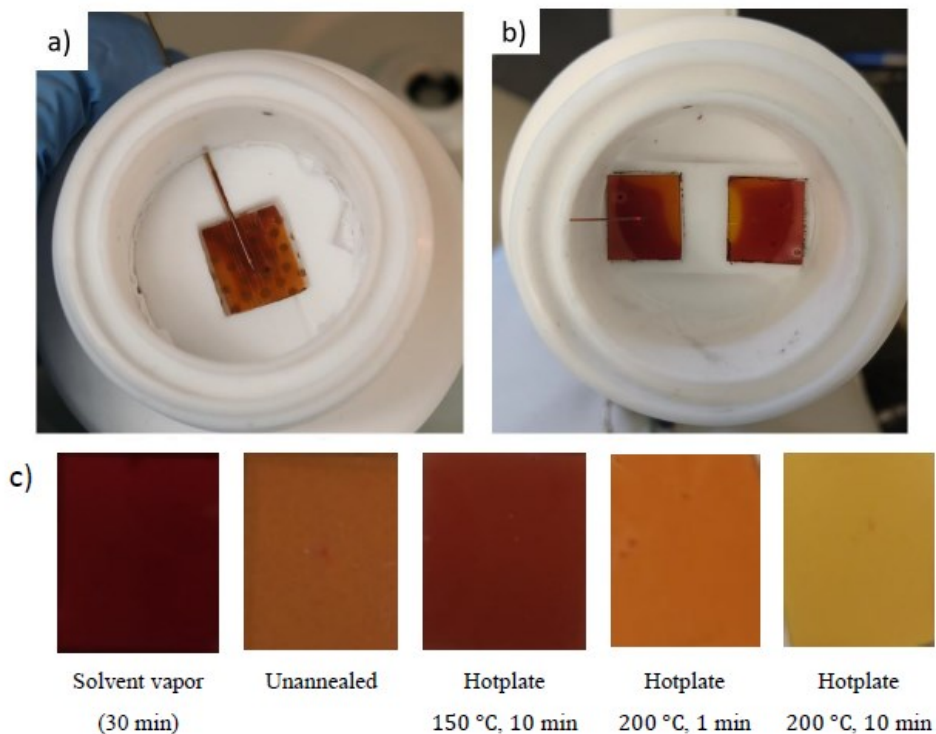


Fig. 3.12: Non-uniform color profile of solar cells prepared from a glass/ITO/PEDOT:PSS/P3HT:PCBM layer structure. a) Single P3HT:PCBM chip and b) double chip setup in the “instant” mode. Non-uniform coloration caused by microwave annealing became significant at higher temperatures or longer annealing times. c) Appearance of reference solvent vapor- and hotplate- annealed P3HT:PCBM chips.

Since non-uniform coloration was present with or without the in-situ thermometer probe and since discoloration was particularly noticeable at higher temperatures or long annealing times, as shown in Fig. 3.13, it was concluded that the poor lateral heat conductivity of ITO was unable to compensate for hot-spots generated by microwave interference generated even in the center of the oven cavity.

Thus, an experiment was carried out where the Teflon vessel was placed on the rotating cog of the microwave so that the chip inside would be irradiated more evenly as it crossed wave anti-nodes forming on the plane of the OPV position. However, this approach resulted in very high temperatures that burned off the organic layers in the cell, did not result in uniform heating, and even melted the glass substrate, see Fig. 3.13. Therefore, the use of a rotating configuration was entirely abandoned.

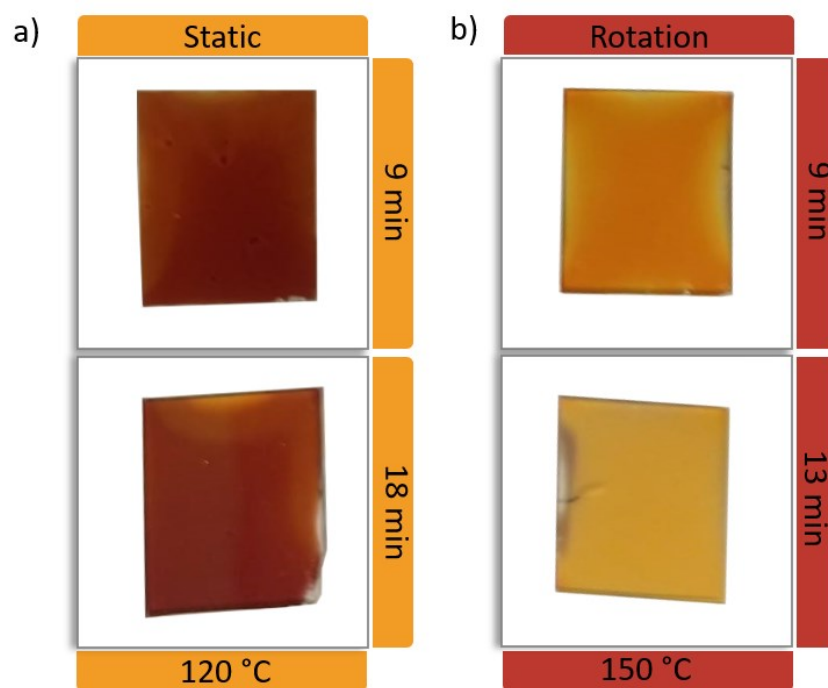


Fig. 3.13: Solar cells prepared from a glass/ITO/PEDOT:PSS/P3HT:PCBM layer structure. Continuous mode annealing of P3HT:PCBM chips for extended times, a) using a static configuration and b) using a rotating configuration.

To further illustrate the negative impact of poor lateral thermal conductivity, a DRCN5T:IT-4F small-molecule system known to be highly responsive to thermal annealing [30] was tested. The blend was spin-coated and annealed using the static instant mode configuration, resulting in a similar edge discoloration as seen in P3HT:PCBM. After annealing, Al/Mg metal contacts were deposited and individual device performance was compared, see Table 3-I.

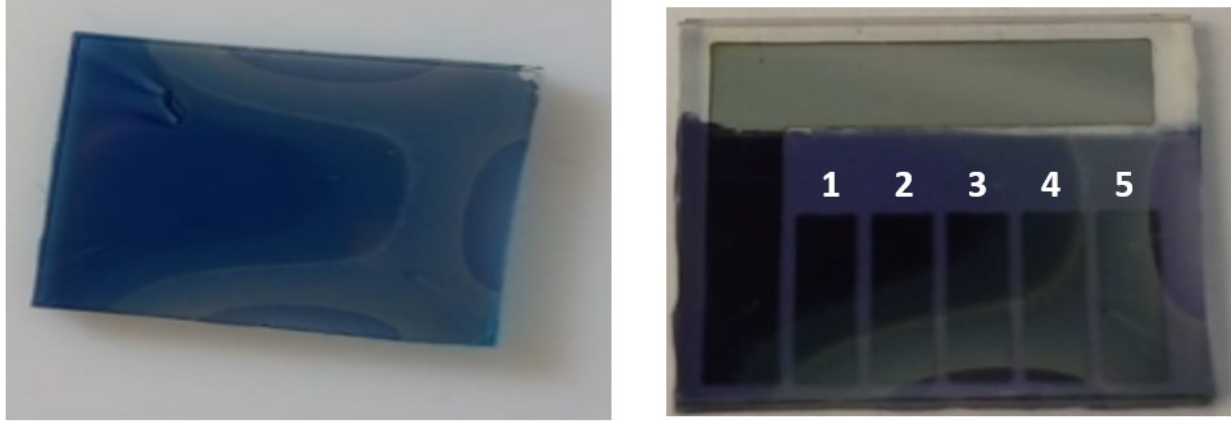


Fig. 3.14: Solar cells prepared from a glass/ITO/PEDOT:PSS/DRCN5T:IT-4F/Al/Mg layer structure. Side by side images of an instant mode (Type I configuration) microwave-annealed OPV chip before and after metal contact deposit. Individual devices are labeled in white.

Table 3-I: Individual device performance of a DRCN5T:IT-4F chip annealed using a Type I configuration

Device	PCE (%)	Jsc (mA/cm ²)	FF (%)	V _{oc} (V)	R _{sh} (kΩ)	R _{sr} (Ω)
1	1.65	4.15	47	0.86	0.69	3.48
2	1.13	2.94	45	0.85	0.65	3.88
3	0.61	1.85	39	0.85	0.88	3.50
4	0.23	0.80	35	0.84	1.37	4.51
5	0.01	0.21	10	0.64	0.85	45.46
No thermal annealing	0.02	0.07	28	0.96	13.91	161.18
Hot Plate: 150 °C, 20 min	3.09	6.74	54	0.85	0.82	2.30

Hot plate and unannealed controls were obtained from the average of 5 individual devices.

While the lateral thermal gradient of the glass-ITO substrate was largely responsible for poor annealing quality, it is also known that conductive objects exposed to an external electromagnetic field tend to experience electrical edge effects where charge accumulates on the borders of the object. This commonly causes electrical discharges and increased heating of metals placed inside a microwave oven. Thus, to improve heat conductivity and reduce electric edge effects in ITO, a Si heating element was introduced. This modification became Type II configuration, as shown in Fig. 3.5b.

3.3.3 Type II configuration

The introduction of a Si heating element to absorb radiation and disperse heat laterally more efficiently reduced the degree of non-uniform coloration of the active layer but did not eliminate it completely, see Fig. 3.15. Inspiration for this heating element approach was taken from the experimental work on microwave heating for organic thin-film self-assembly by Cong et al. [135].

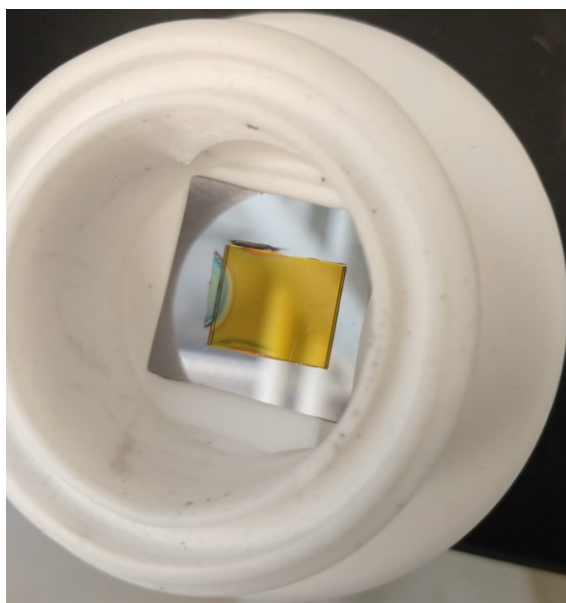


Fig. 3:15: Solar cell corresponds to a glass/ITO/PEDOT:PSS/P3HT:PCBM layer structure. Microwave edge defects persisted in the Type II configuration.

The dimensions of the heating element were approximately L :24.5, W: 27.5 cm, H: 0.06 cm and the dimensions of the glass substrate were approximately L: 13.0, W: 15.5 cm, H: 0.11 cm. Additional details are provided in the materials section. Building on this improvement, a Type III

configuration (Fig. 3.5c) was implemented which consisted of two Si elements with the same dimensions placed above and below the glass substrate with the ITO sandwiched between them facing down. Teflon weights were added to the vessel to improve contact between the active layer and the Si surface.

3.3.3 Type III configuration

High temperature tests with the Type III configuration were considered adequate to begin bulk heterojunction optimization, see Fig. 3.16. For microwave-annealed samples manufactured to be tested in the solar simulator, unless otherwise indicated, the Teflon vessel was sealed in a nitrogen atmosphere in a glove box, brought to the microwave for annealing, allowed to cool inside the vessel for 2 min prior to sample extraction¹, and finally, taken to the metal evaporator for metallic contacts deposition. Because the vessel was sealed, in-situ temperature could not be measured. Instead, temperature parameters were first calibrated and then the sample was annealed to an extrapolated target temperature.

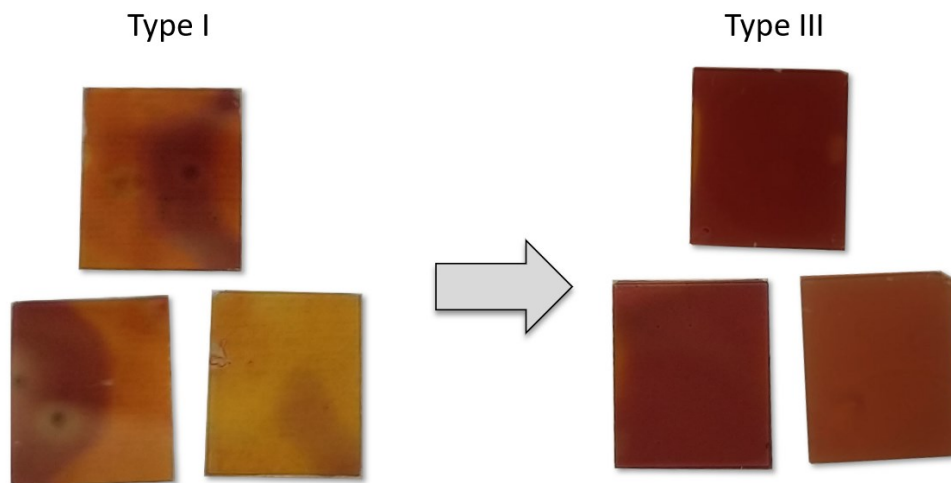


Fig. 3.16: Comparison of the visual appearance of three P3HT:PCBM OPV samples microwave-annealed using a Type I and a refined Type III configuration. Discoloration corresponding to hotspots is considerably reduced by the introduction of Si heating elements above and below the substrate. Note that small areas of non-uniform heating were still present on the borders for

¹ This time was chosen arbitrarily to facilitate handling. The time the substrate remains at the target temperature is close to 3 s, afterwards, a rapid decrease in temperature was observed.

samples prepared using the Type III setup; however, those imperfections did not greatly impact device quality.

The increased quality of microwave treatment enabled a more reliable and reproducible optimization of P3HT:PC₆₁BM OPVs. Attempts were made to optimize microwave annealing around extended treatment times (ie. “continuous mode” microwaving). However, the introduction of multiple Si elements greatly increased the heat dispersive nature of the setup and temperature resolution decreased considerably (variance of ± 17 °C), see. Fig. 3.17.

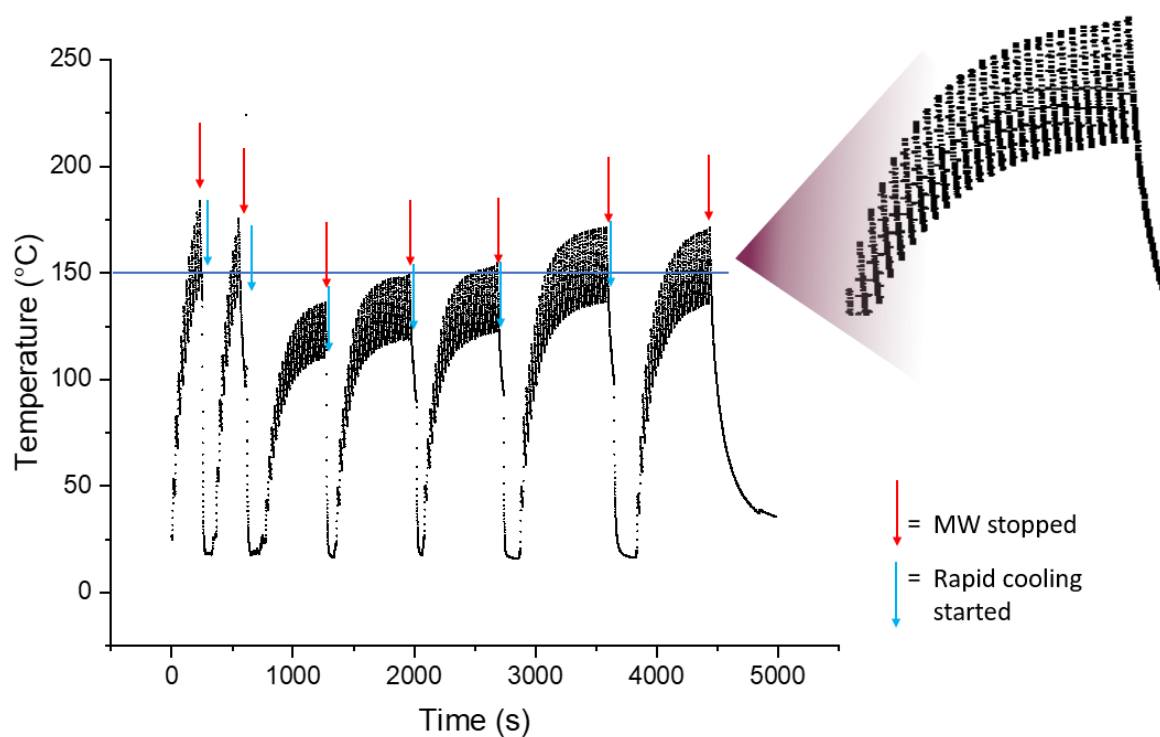


Fig. 3.17: Temperature calibration of a continuous mode Type IV treatment. Target “convergence” temperature was set at the P3HT:PCBM optimized value of 150 °C. Multiple adjustments to the SiC mass in the control crucible were made to achieve it. A magnified view of the microwave duty cycle profile is shown in the inset.

Additionally, preliminary testing suggested a decrease in OPV performance as a function of increased microwave time (time spent annealing in a regime where convergence temperature was reached), likely due to excessive upper bound heating. This behavior is exemplified in Table 3-II. In the case of continuous treatment, the upper temperature bound was expected to be 167 °C,

whereas, in the case of 3 consecutive “instant” runs, the expected temperature after the third cycle was expected to be 200 °C. For continuous treatment, the ramp-up time necessary for convergence temperature was roughly 8 min and the time spent annealing after that time was considered as the effective annealing time. Because the temperature could not be adequately controlled, these attempts at increasing the annealing time at a chosen convergence temperature were abandoned. However, in a more sophisticated microwave oven where the pulse and output power can be fine-adjusted, it may be possible to achieve better results.

Table 3-II: Extended microwave annealing of P3HT:PC₆₁BM

Mode	Treatment	PCE (%)	J _{sc} (mA/cm ²)	FF (%)	V _{oc} (V)	R _{sh} (kΩ)	R _{sr} (Ω)
Continuous	8 min ramp + 2 min effective annealing	0.69	2.71	42	0.58	0.91	11.62
Instant	3 consecutive cycles, 56 s each	0.59	2.01	45	0.64	1.18	14.81
Instant	1 cycle	0.84	2.43	54	0.63	1.43	4.39

Results are the average of at least 5 devices.

Further microwave experiments confirmed that the most effective annealing occurred when a single heating run was carried out. A comparison between conventional thermal annealing and microwave annealing of P3HT:PC₆₁BM OPVs showed a small difference between performance achieved by both approaches, see Table 3-III. Particularly, microwave annealed cells had a slight decrease in performance, perhaps attributable to the reduced time that the active layer had to phase segregate or perhaps due to random annealing temperature variations.

3.4 Optimization of P3HT:PC₆₁BM organic photovoltaic solar cells

Note that since P3HT:PC₆₁BM has been widely studied in the literature and since in this work it was not the object of the study but rather an aid used for calibration and screening purposes, a more comprehensive evaluation of this bulk heterojunction was not performed. Thus, the number of devices differed between examined treatments. Nevertheless, clear tendencies in performance are still evident.

Table 3-III: Reference controls for P3HT:PC₆₁BM solar cells

Treatment	Expected Temperature	Atmosphere	PCE (%)	Jsc (mA/cm ²)	FF (%)	V _{oc} (V)	R _{sh} (kΩ)	R _{sr} (Ω)	No. of devices
No thermal annealing	20 °C	Air	1.82 ± 0.22	6.24 ± 0.63	46 ± 4	0.59 ± 0.03	0.55 ± 0.12	15.34 ± 9.63	15
			2.18	6.85	54	0.60	0.40	6.14	Maximum
SVA 30 min	20 °C	DCB vapor-enriched air	3.97 ± 0.21	10.91 ± 0.56	59 ± 1	0.63 ± 0.01	1.09 ± 0.22	2.35 ± 0.23	15
			4.30	11.66	59	0.63	1.10	2.25	Maximum
Thermal HP 10 min	100 °C	Air	1.74 ± 0.41	6.29 ± 1.55	47 ± 4	0.61 ± 0.07	0.41 ± 0.10	7.72 ± 2.47	10
			2.10	7.18	46	0.62	0.34	10.60	Maximum
Thermal HP 10 min	150 °C	Air	1.89 ± 0.44	5.78 ± 1.15	51 ± 1	0.64 ± 0.03	0.50 ± 0.03	7.79 ± 3.08	10
			2.41	7.08	51	0.67	0.50	7.84	Maximum

HP denotes conventional hot-plate annealing; MW denotes Type III microwave annealing.

Table 3-IV: Performance evaluation for microwave-annealed P3HT:PC₆₁BM solar cells

Treatment	Expected Temperature	Atmosphere	PCE (%)	Jsc (mA/cm ²)	FF (%)	V _{oc} (V)	R _{sh} (kΩ)	R _{sr} (Ω)	No. of devices
MW 6 s	60 °C	N ₂	2.12 ± 0.26	5.52 ± 0.79	59 ± 2	0.65 ± 0.01	0.69 ± 0.11	4.60 ± 0.69	8
			2.45	6.64	58	0.64	0.55	4.50	Maximum
MW 7 s	80 °C	N ₂	2.55 ± 0.46	6.34 ± 1.15	61 ± 2	0.66 ± 0.01	0.69 ± 0.12	4.91 ± 2.76	10
			3.30	8.08	0.63	65	0.71	1.90	Maximum
MW 8 s	100 °C	N ₂	2.26 ± 0.20	6.44 ± 0.55	54 ± 2	0.65 ± 0.01	0.61 ± 0.10	3.26 ± 0.58	10
			2.46	6.79	56	0.54	0.65	2.56	Maximum
MW 9 s	130 °C	N ₂	1.56 ± 0.42	4.64 ± 0.86	51 ± 3	0.65 ± 0.02	0.63 ± 0.08	5.66 ± 1.74	8
			2.34	6.13	57	0.67	0.74	3.00	Maximum
MW 10 s	150 °C	N ₂	1.01 ± 0.41	3.61 ± 1.46	44 ± 10	0.65 ± 0.04	0.83 ± 0.46	13.28 ± 8.80	15
			1.78	6.72	47	0.56	0.55	16.23	Maximum

HP denotes conventional hot-plate annealing; MW denotes Type III microwave annealing.

Table 3-V: Performance evaluation for hotplate annealed P3HT:PC₆₁BM solar cells

Treatment	Expected Temperature	Atmosphere	PCE (%)	Jsc (mA/cm ²)	FF (%)	V _{oc} (V)	R _{sh} (kΩ)	R _{sr} (Ω)	No. of devices
HP 10 min	80 °C	N ₂	1.86 ± 0.10	4.86 ± 0.32	59 ± 2	0.65 ± 0.01	0.74 ± 0.08	5.87 ± 0.77	10
			2.00	5.18	60	0.64	0.72	4.80	Maximum
HP 10 min	100 °C	N ₂	2.51 ± 0.18	6.93 ± 0.65	57 ± 4	0.63 ± 0.02	0.50 ± 0.05	3.91 ± 0.47	8
			2.72	7.83	55	0.63	0.52	4.35	Maximum
HP 10 min	130 °C	N ₂	2.49 ± 0.36	6.60 ± 0.79	59 ± 4	0.64 ± 0.02	0.58 ± 0.10	3.67 ± 0.48	6
			2.85	7.48	61	0.63	0.50	3.89	Maximum
HP 10 min	150 °C	N ₂	3.03 ± 0.19	7.80 ± 0.36	59 ± 2	0.66 ± 0.01	0.59 ± 0.17	2.89 ± 0.65	6
			3.32	8.37	60	0.66	0.76	2.40	Maximum
HP 5 min	150 °C	N ₂	1.62 ± 0.15	5.20 ± 0.46	50 ± 0	0.63 ± 0	0.62 ± 0.03	3.54 ± 0.41	5
			1.74	5.57	50	0.63	0.60	3.28	Maximum
HP 2 min	150 °C	N ₂	1.06 ± 0.19	3.84 ± 0.48	45 ± 2	0.60 ± 0.01	0.53 ± 0.04	4.61 ± 0.70	5
			1.21	4.32	46	0.61	0.51	5.33	Maximum
HP 10 min	200 °C	N ₂	0.38 ± 0.01	1.84 ± 0.07	28 ± 0	0.73 ± 0	0.61 ± 0.04	22.90 ± 1.29	5
			0.39	1.89	28	0.73	0.59	23.30	Maximum

HP denotes conventional hotplate annealing; MW denotes Type III microwave annealing.

From the results in the previous tables it was confirmed as has been reported in the literature, that hotplate annealing at 150 °C for 10 min is ideal to optimize power conversion efficiency of the P3HT:PCBM composition. Intriguingly, with this microwave configuration, 7 s (80 °C) resulted in the highest performance out of all the tested microwave annealing times. Because the substrate was sealed inside the Teflon vessel, no in-situ temperature measurement could be carried out to definitively confirm whether the substrate annealed at this temperature. Additionally, because the position of the OPV chip between the Si heating elements might have shifted during transport from the glove box to the oven, further temperature validations are needed to explain the discrepancy between this annealing temperature difference to expected power conversion efficiency. An improved statistic analysis could also help to give better context to the limited data captured.

3.5 Type IV configuration

While the Type III configuration led to promising results, the persistence of minor edge defects continued to be a source of worry. It was believed that during the transport from the glove box to the microwave the glass substrate might move off center towards the edge of the Si elements and anneal non-uniformly or at incorrect temperatures. Therefore, a larger Si heating element was introduced to reduce the local thermal gradient around the cell and further improve the annealing setup, see Fig. 3.18.

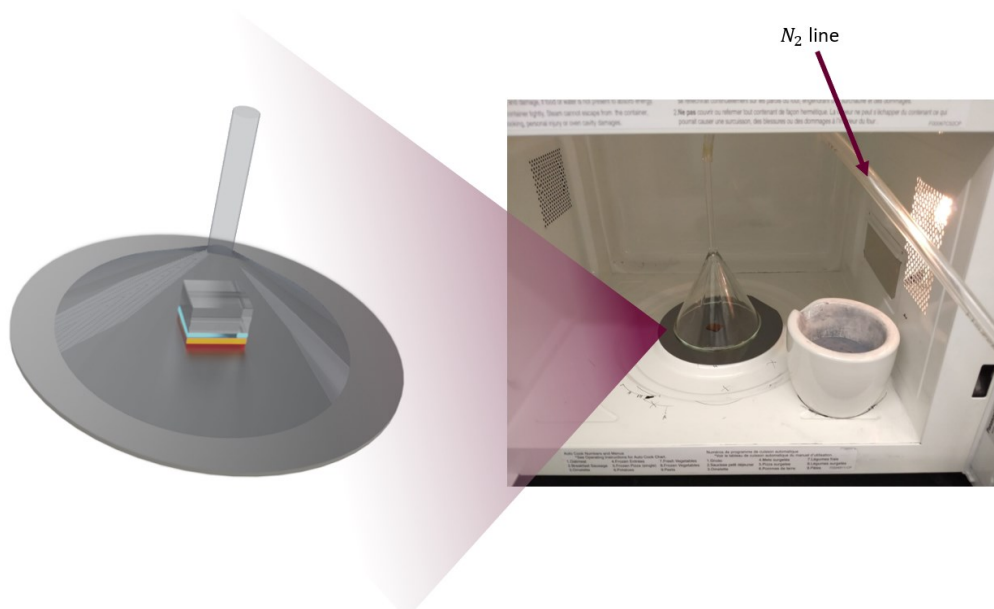


Fig. 3.18: Type-IV microwave annealing configuration. Here, the OPV cell is flipped so the glass substrate faces upwards. A moderate nitrogen gas flow is allowed to flush oxygen inside the funnel for 2 minutes prior to annealing to reduce the possibility of oxidation of the BHJ. Afterwards, the gas line is carefully disconnected, and the microwave door is closed to perform the annealing treatment.

In this configuration, the Si wafer (heating element) was allowed to rest on a small circular Teflon base to facilitate setup “reset” to room temperature in between different treatments. While the same inherent hot-spot problem seen in previous configurations remained, the larger area significantly reduced local device performance variations in OPV solar cells. To better understand the thermal profile of the heating element, a second Si wafer was covered with black electrical tape, microwaved, and thermographs were taken with an IR camera. Note that since the wafer was too hot to handle, the thermographs were taken at an angle and therefore, the thermal overlay in the thermographs is slightly shifted. See Fig. 3.19 and Fig. 3.20.

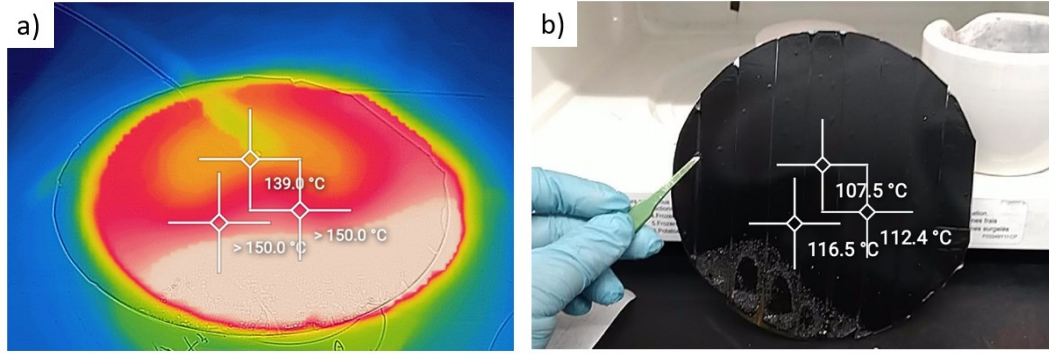


Fig. 3.19: a) Thermograph of a Si heating element showing a region of intense heating on one edge, likely corresponding to the position of antinodes in the microwave cavity (taken approximately after 30 s of microwave exposure). b) Visual inspection of the heating element immediately after microwaving.

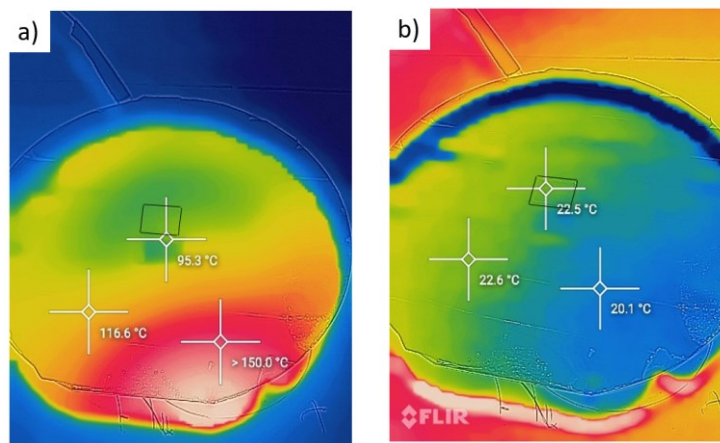


Fig. 3.20: Thermographs of solar cell and heating element taken a) immediately after microwaving and b) after several minutes of cooling. The physical location of the solar cell is marked by a black square and was always placed at the center of the wafer during the entire project.

At first sight, the temperature gradient of the larger heating element might suggest considerable variance between individual devices of the OPV chip. However, the excellent thermal conductivity of the Si appears to cause a wave-like heat diffusion throughout its volume. An analogy that may facilitate conceptualization of this effect is by imagining a rain cloud that moves over a small town from East to West; the eastern parts of the town will get wet before the western parts, but in the end they will all receive roughly the same amount of rain. In this sense, a Type IV configuration (Table 3-VI) takes advantage of the much larger ratio of wafer heating area vs OPV substrate area

to reduce local temperature differences between devices. No noticeable local variance directly attributable to poor thermal uniformity was seen in OPV substrates annealed with this configuration.

Table 3-VI: Individual device performance of a ZR1:BTP-BO-4Cl solar cell
MW-annealed for 15 s

Dev	PCE (%)	Jsc (mA/cm²)	FF (%)	V_{oc} (V)	R_{sh} (kΩ)	R_{sr} (Ω)
1	7.58	14.61	57	0.91	0.46	2.00
2	6.89	13.56	56	0.91	0.53	3.10
3	6.48	12.76	56	0.91	0.57	2.88
4	7.41	13.90	59	0.91	0.55	2.72
5	7.02	14.02	56	0.90	0.43	2.22

Device variance is within expected tolerance for spin-coated OPVs.

Although this Type IV setup allows for a functional thermal annealing range between ≈ 1 -20 s of microwave treatment corresponding to an OPV substrate temperature of ≈ 20 -150 °C, hot-spot non-uniformity became too extreme for the Si to effectively disperse heat after 23 s (173 °C). After this time, the same edge effects seen in other configurations were considerable.

Once the Type IV configuration was validated for reliability, a calibration curve was obtained and optimization of an all-small molecule bulk heterojunction was performed. These temperatures were measured with a microwave-compatible fiber optic probe in physical contact with the glass side of the OPV solar cells.

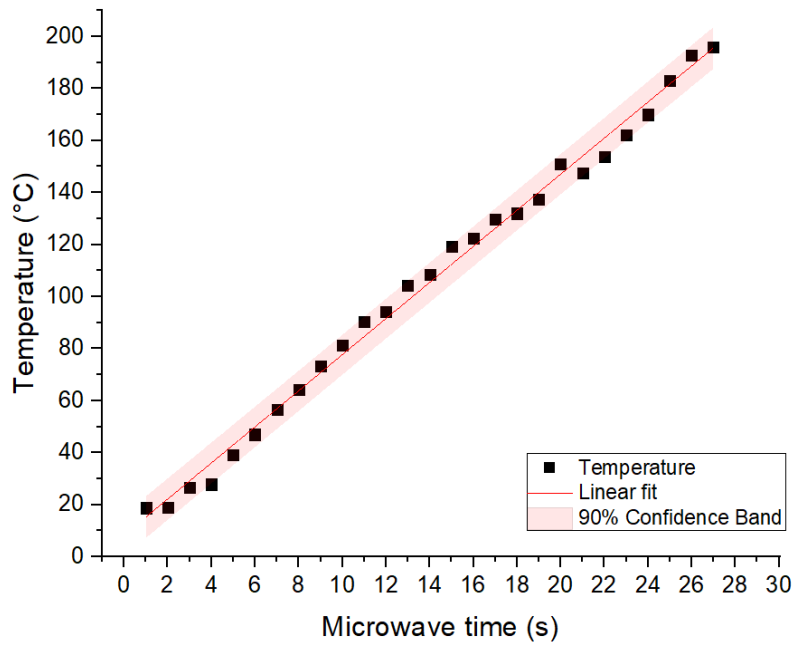


Fig. 3.21: Calibration curve of microwave time vs temperature for the Type IV configuration, taken by measuring the temperature various glass/ITO substrates.

A linear fit was calculated for this calibration curve as:

$$T = (6.93 \text{ }^\circ\text{C/s})t + 8.35 \text{ }^\circ\text{C}$$

$$\Delta m = \pm 0.10 \text{ }^\circ\text{C/s}$$

$$\Delta b = \pm 1.73 \text{ }^\circ\text{C}$$

where T is the temperature of the OPV substrate, Δm is the uncertainty of the slope, and Δb is the uncertainty of the intercept.

Although a more realistic behavior could have been modelled where a temperature intercept matched with the room temperature, this linear fit was sufficient for the purposes of estimating the temperature that the OPV substrate reached and shows that this configuration has a thermal resolution of roughly $7 \text{ }^\circ\text{C/s}$.

Limited optimization of a ZR1:BTP-BO-4Cl bulk heterojunction composition was performed by a rapid one-variable-at-a-time optimization approach. While more powerful approaches have been previously explored by our group [99], [100], time limitations and a focus on microwave annealing were reasons to apply this simple approach. To our knowledge, this blend has not been previously

reported but falls in line with a wider literature pattern in favor of non-fullerene acceptors paired to high efficiency donors, particularly of the Y-series type [80], [83], [154]. Additionally, ZR1 is one of a handful of reported high efficiency ($14\% < \text{PCE}$) small molecule donors.

3.5.1 ZR1:BTP-BO:4Cl optimization

The initial inspiration for this blend was the work of Zhou et al. [13] where a ZR1:Y6 composition was optimized via thermal annealing for a maximum PCE of 14.34%. The BTP-BO-4Cl acceptor was chosen as a substitute of Y6 because the ZR1:BTP-BO-4Cl blend had a compatible energy level structure, this BTP-BO-4Cl chlorinated, butyloctyl version of Y6 has been reported to have enhanced solubility and lead to higher performance for PM6-based cells. Additional details may be found in the materials section.

In this work, preliminary screening tests were performed by varying the donor:acceptor weight ratio between 1:0.4, 1:0.5, and 1:0.7 while maintaining a fixed total concentration of 15 mg/mL and varying the spin speed. Additional sample preparation details are found in the Materials and Substrate Preparation section.

From those limited screening tests, the best performance was found at 1:0.5 w.w. ratio of ZR1:BTP-BO-4Cl. Optimum spin speed was 2200 rpm. As was discussed in Chapter 2, electron transport layers play a considerable role in improving charge collection and reducing recombination. While Zhou et al. did not report the use of an ETL, this work did. A PFN-Br layer was deposited on the bulk heterojunction by spinning it at 3000 rpm from a 0.5 mg/mL solution of methanol (corresponding to a thickness of roughly 2-3 nm). It was found that unlike PM6:BTP-BO-4Cl, this electron transport layer needed to be spin-coated prior to thermal annealing to prevent film cracking, see Fig. 3.22.



Fig. 3.22: Cracking effect of PFN-Br/MeOH on the active layer if the electron transport layer is spin coated after thermal annealing.

A more targeted study is necessary to conclusively determine what is behind this cracking behavior after the MeOH spin coat step. In Chapter 2, it was argued that the interaction between methanol and additive remnants in the bulk heterojunction or water in the PEDOT:PSS could induce dewetting effects. It was also mentioned that methanol has been used to separate the PSS polymer from PEDOT and this separation may translate into percolation pathways that further induce dewetting. While in this particular blend no additives were used, another possibility behind the cracking may be due to the phase segregation taking place between ZR1 and BTP-BO-4Cl after annealing. In the untreated state, both donor and acceptor molecules are thought to be uniformly dissolved throughout the film. After thermal annealing, phase segregation occurs, allowing for even more pathways for the methanol to reach the PEDOT layer.

For the purposes of this work, PFN-Br/MeOH was spin coated prior to thermal annealing. No major difference in performance was seen with respect to samples prepared by evaporating the PFN-Br layer on the thermally annealed bulk heterojunction. A note to consider is that if the liquid PFN-Br/MeOH solution was left in contact with the bulk heterojunction for more than a few seconds, cracking would start to happen even in unannealed samples.

Since a considerable number of OPV papers report a thermal annealing step above 100 °C, this work focused on screening a microwave annealing time range roughly centered around this

temperature. From individual solar cell performance results and averaged results (Fig. 3.23 and Fig. 3:24, respectively), it is possible to see that power conversion efficiency increases roughly by 5x when compared to unannealed samples (denoted by a green square in Figs. 3:24-3.25). In particular, 15 s of microwave annealing, corresponding to roughly 112 °C seemed to provide the best improvement. No significant difference was observed with the corresponding hot-plate results, shown in Figs. 3:23-3.25.

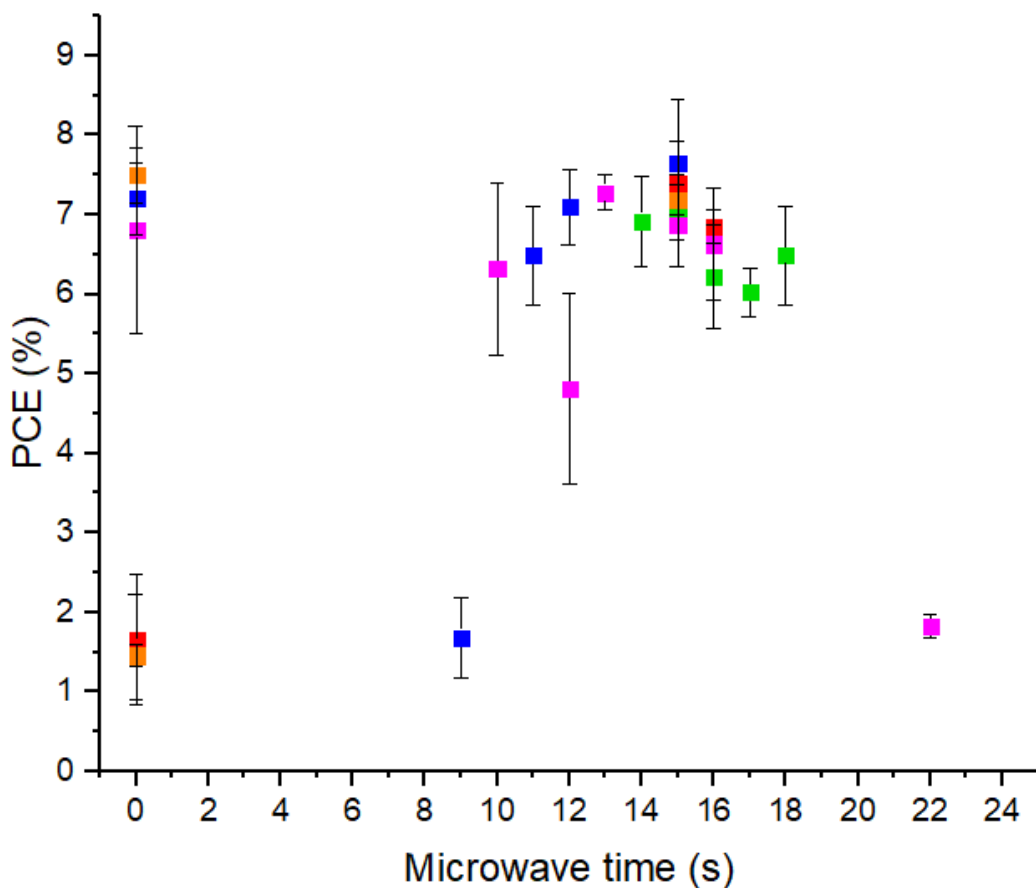


Fig. 3:23: Effect of microwave time on power conversion efficiency for different batches of individual ZR1:BTP-BO-4Cl solar cells (different colors represent different batches). The individual data points in this graph correspond to the averaged PCE of multiple devices in the OPV chip. Error bars correspond to performance values one standard deviation away from the average.

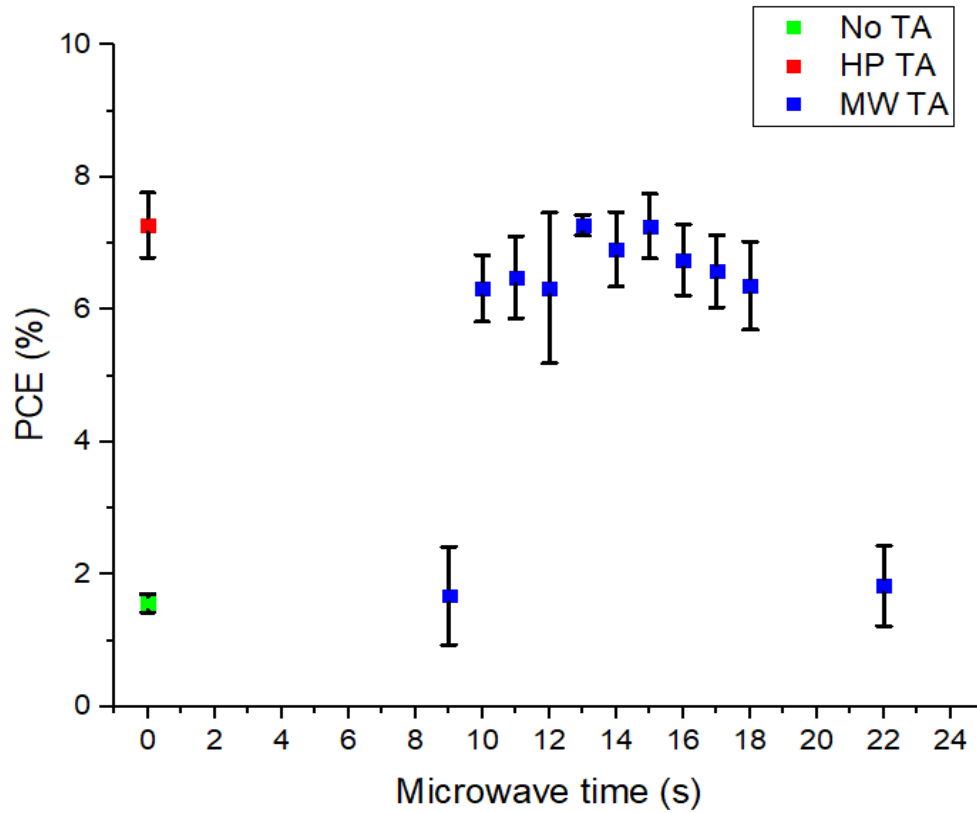


Fig. 3:24: Effect of microwave time on power conversion efficiency for ZR1:BTP-BO-4Cl solar cells. The data points correspond to averaged results of multiple solar cells annealed under the same conditions. Error bars correspond to performance values one standard deviation away from the average.

To better track and identify the source of the performance improvement in this ZR1:BTP-BO-4Cl con, various solar parameters were plotted as a function of microwave time, see Fig. 3.25.

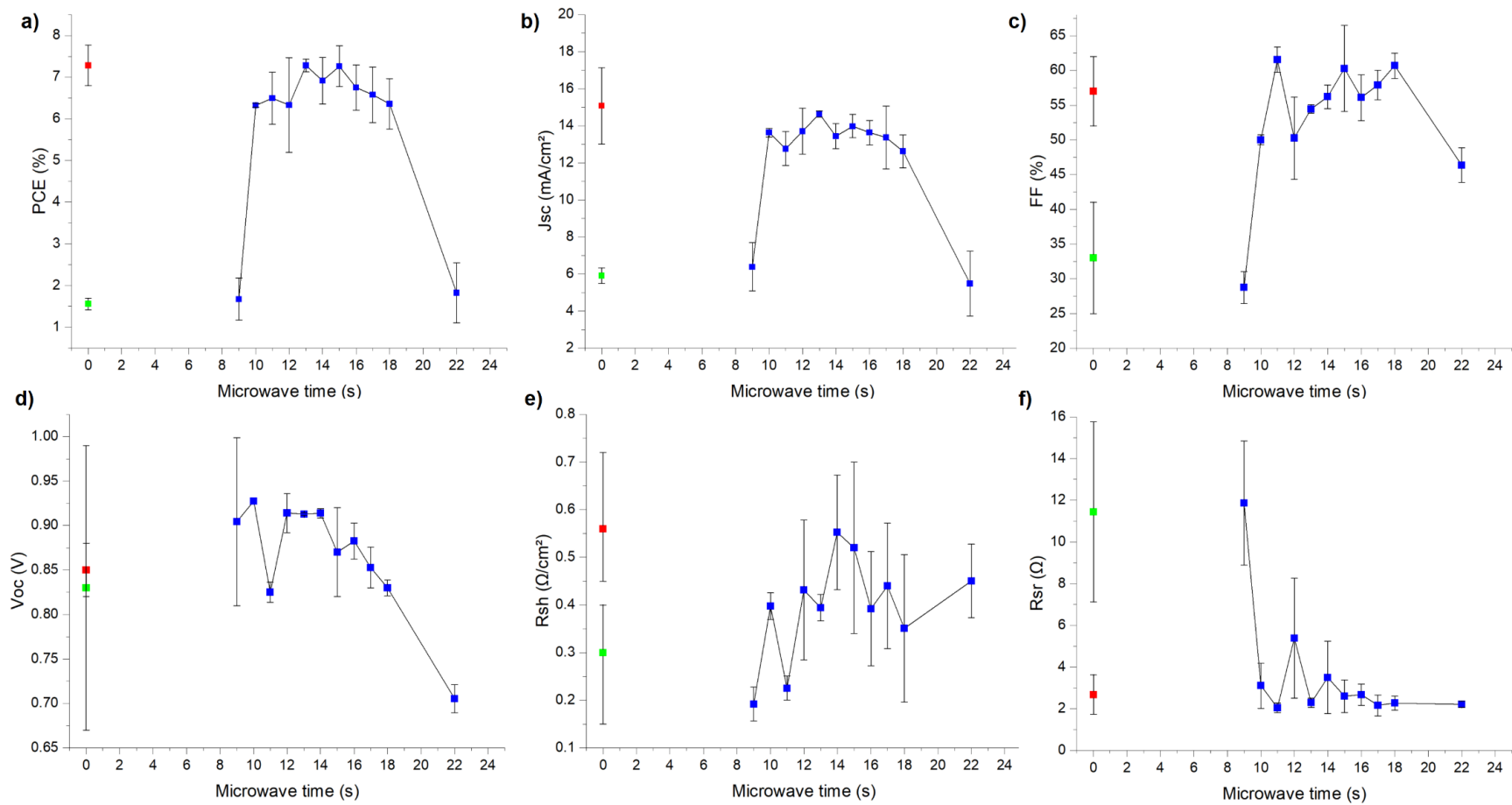
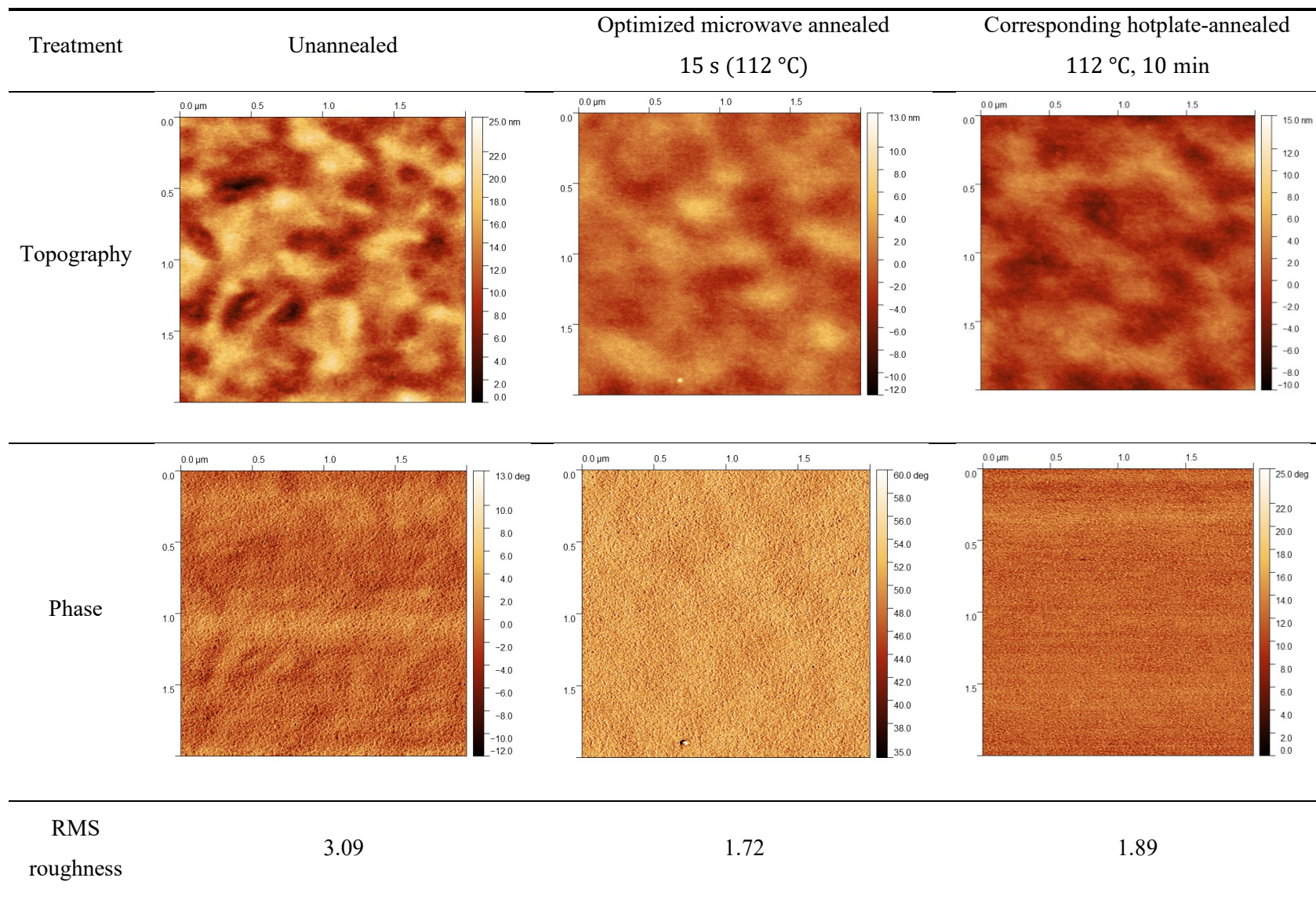


Fig. 3.25: Effect of microwave annealing time on various solar parameters, a) on power conversion efficiency, b) on short-circuit current, c) on fill factor, d) on open-circuit voltage, e) on shunt resistance, f) on series resistance. Blue squares correspond to averaged response of microwaved solar cells, green squares correspond to unannealed cells, and red to hotplate annealed cells. Error bars correspond to performance values one standard deviation away from the average.

Table 3-VII: Atomic force micrographs of unannealed, microwave-annealed, and hotplate-annealed ZR1:BTP-BO-4Cl OPV samples



From the data in Fig 3:25, it can be observed that improved performance after thermal annealing is caused by the collective effects of enhanced short circuit current, fill factor, and series resistance.

A likely reason for this improved current generation, as has been previously discussed, is due to the thermally induced modification of the morphology of the bulk heterojunction. Particularly, a comparison of the height and roughness features of the micrographs in Table 3-VII suggests a smoothening of the surface after annealing, likely caused by improved molecular packing and solvent evaporation. As the molecules are given kinetic energy by the microwaves, they are likely to reposition themselves in more compact and energetically-favorable structures. This might explain the decrease in height difference between the nadirs and zeniths as compared to the unannealed sample. The active film thicknesses for the unannealed OPV, optimized microwave-annealed, and corresponding hotplate-annealed samples was 122 nm, 111 nm, and 113 nm, respectively. Thus, it reasonable to expect that the added kinetic motion and the dehydration of the cells by the evaporation of solvent (water from the PEDOT:PSS and chloroform remnants from the bulk heterojunction) created a structure with fewer defects for charges to become trapped or recombined. This is supported by the increased conductivity manifested as a decrease in series resistance in Fig. 3:26. A thinner layer is expected to be less resistive than a thicker one because the greater the distance a charge carrier must travel, the more possibilities there are for it to collapse and recombine or encounter a trap site, for instance by those created by solvent molecules remaining in the layers. A smoother film may also help to reduce interfacial defects between the different layers that might trap charge carriers. These reasons could explain the improved fill factor and improved conductivity seen in Fig. 3:25b, f.

As was mentioned previously, it is generally accepted that larger donor domains lead to improved exciton generation, thus as more excitons are available for charge extraction, the short circuit current is expected to increase, as is seen in Fig. 3:25b. Additionally, the increase in shunt resistance shown in Fig. 3.25e suggests a decrease in current leakage pathways [155], so more efficient charge transport is taking place. Another contributing factor constant throughout this work was the introduction of PFN-Br as a hole blocking layer, fewer recombination interactions occur at the boundary with the metal contacts, thus, more of the charge carriers can be separated for external work to be carried out.

While ultimate power conversion efficiency achieved with this blend in this chapter is below the high-efficiency PM6:BTP-BO-4Cl system discussed in chapter 2, there is still much left to explore and much optimization potential for the ZR1:BTP-BO-4Cl system. Particularly, this blend exhibits a high V_{oc} of ≈ 0.90 V and for one experimental batch, three distinct solar cells achieved power conversion efficiencies above a symbolic 10% value (parameters were DA ratio of 1:0.5 w/w., tot. conc. 15 mg/mL). However, it is important to note these results could not be reproduced a second time. A more in-depth examination to determine the source of irreproducibility could not be carried out in the available time and with the available amounts of material. Therefore, these results were catalogued as outliers and were not included in this analysis. Subsequent tests with the same 1:0.5 w/w. DA ratio and total concentration of 15 mg/mL led to more consistent $< 8\%$ PCE. A possible explanation for this discrepancy might be that the molecules did not fully dissolve in the 10% PCE batch, hence the ratio and concentration did not match the target values. Additionally, because chloroform rapidly evaporates, it is possible that a faulty seal in the dissolution vial for that batch altered the total concentration of the solution.

It is also important to note that occasional small specks of undissolved molecules could be seen on spin coated films throughout this work but they were minimized by increasing the dissolution time from 3 h to overnight. This solubility variance could be a reason for batch-to-batch variability seen in Fig. 3:23. However, because the same improvement trend remains with the application of microwave annealing, the benefit of the approach itself is not put in doubt.

Table 3-VIII: Individual device performance for an outlier ZR1:BTP-BO-4Cl batch

BHJ Spin speed	PCE (%)	Jsc (mA/cm²)	FF (%)	V_{oc} (V)	R_{sh} (kΩ)	R_{sr} (Ω)
1800	10.01	20.23	56.8	0.87	0.27	2.01
1800	10.43	21.20	56.6	0.87	0.28	1.91
1800	9.83	21.20	52.3	0.89	0.22	1.81
1800	9.67	20.33	53.5	0.89	0.17	2.08
1800	10.06	20.40	55.4	0.89	0.30	2.31
2200	9.60	20.01	55.0	0.87	0.19	1.64
2200	9.57	20.00	54.7	0.87	0.18	1.64
2200	9.52	19.82	55.0	0.87	0.17	1.83

Provided for reference as a cautious potential lead to future works.

The following is a compilation of the averaged results considered reliable in this work.

Table 3-IX: Averaged ZR1:BTP-BO-4Cl performance results as a function of annealing treatment

Treatment	PCE (%)	Jsc (mA/cm²)	FF (%)	V_{oc} (V)	R_{sh} (kΩ)	R_{sr} (Ω)	No. of devices
Unannealed	1.56	5.91	33.3	0.83	0.35	13.29	11
TA 112 °C, 10 min	7.28	15.08	56.9	0.84	0.50	2.85	14
TA 112 °C, 15 s flipped	6.32	13.02	52.9	0.91	0.38	2.56	7
MW 9 s	1.68	6.38	28.7	0.90	0.19	11.87	4
MW 10 s	6.32	13.63	50.0	0.93	0.40	3.11	4
MW 11 s	6.49	12.77	61.5	0.82	0.23	2.05	4
MW 12 s	6.33	13.71	50.2	0.91	0.43	5.39	8
MW 13 s	7.28	14.64	54.4	0.91	0.39	2.29	4
MW 14 s	6.91	13.44	56.2	0.91	0.55	3.50	8
MW 15 s	7.26	13.98	59.9	0.87	0.52	2.71	19
MW 16 s	6.75	13.63	56.0	0.88	0.39	2.68	9
MW 17 s	6.58	13.36	57.9	0.85	0.44	2.17	6
MW 18 s	6.36	12.62	60.6	0.83	0.35	2.27	8
MW 22 s	1.82	5.48	46.3	0.71	0.45	2.21	3

Although the number of devices varied between treatments, when considered in combination with the trends in Fig. 3:23 and Fig. 3:24, it is reasonable to take 15 s as the optimum microwave annealing time.

Table 3-X: Reference unannealed, microwaved, and hotplate annealed ZR1:BTP-BO-4Cl OPV cells with uncertainties

Treatment	PCE (%)	Jsc (mA/cm²)	FF (%)	V_{oc} (V)	R_{sh} (kΩ)	R_{sr} (Ω)
Unannealed	1.56 ± 0.14	5.91 ± 0.42	33.3 ± 7.8	0.83 ± 0.16	0.35 ± 0.15	13.29 ± 4.32
TA 112 °C, 10 min	7.28 ± 0.49	15.08 ± 2.06	56.9 ± 4.8	0.84 ± 0.03	0.50 ± 0.16	2.85 ± 0.94
MW 15 s (112 °C)	7.26 ± 0.49	13.98 ± 0.63	59.9 ± 5.8	0.87 ± 0.05	0.52 ± 0.18	2.71 ± 0.78

These averaged results are highlighted as the core results of this section

Table 3-XI: Maximum device performance achieved for the different reference treatments (ZR1:BTP-BO-4Cl OPV cells)

Treatment	PCE (%)	Jsc (mA/cm²)	FF (%)	V_{oc} (V)	R_{sh} (kΩ)	R_{sr} (Ω)
Unannealed	1.78	6.72	0.47	0.56	0.55	16.23
TA 112 °C, 10 min	7.99	21.97	0.44	0.83	0.11	2.24
MW 15 s	8.09	14.84	0.59	0.92	0.65	2.54

These individual device results are provided as reference; however, conclusions should be based off the average device performances.

One of the main observations from Table 3-IX is that performance is generally high in an annealing time range of 10-18 s (77-133 °C). In other words, although performance experiences a slight peak around 13-15 s (98-112 °C), this improvement is not considerably different from the wider time range. Especially when considering that spin-coating OPVs will inevitably lead to slight variations in performance due to the nature of the deposition technique.

Although additional testing is required to improve the statistical representability, for instance, around 14 s of annealing time, the annealing improvement is highlighted by the bathtub-like curve of efficiency vs microwave time. The sudden drop in efficiency towards higher annealing time in

Fig. 3:24 is due to excessive heating of the Si element after 22 s of microwave irradiation. Despite its good lateral thermal conductivity, the wafer cannot disperse heat fast enough to prevent cell burn out. At the other end of smaller annealing time, the sudden drop could indicate a critical temperature for molecular rearranging. It is known that the boiling point of chloroform is roughly 60 °C, perhaps a reason why efficiency suddenly increases after 9 s (70 °C) is that at higher temperatures, enough solvent is removed for adequate nanomorphologies to form. However, future experiments should be carried out to confirm this hypothesis by testing annealing times below 9 s and to a more complete study. A factor to consider when testing low microwave temperatures is that the temperature of the substrates may increase during the metal evaporation step, so even if a sample is intentionally microwave-annealed at a low temperature, the real device may still anneal at a higher temperature during contact deposition.

An additional test was carried out to compare a microwave and conventional rapid thermal annealing. In this test, a silicon wafer was placed on the hotplate and a thermometer probe was allowed to rest on the surface of the wafer. A temperature of 112 °C was set and a flipped-chip thermal treatment was applied for 15 s. From the solar characterization shown in Table 3-X, it can be seen that little variance occurs between both conditions. However, the slightly lower efficiency with the fast conventional treatment may be due to the additional 30 s of temperature equalization time given to the microwaved samples. During this time, the sample may still be annealing albeit at a lower temperature than the maximum 112 °C which is sustained for roughly 4 s.

This comparability in efficiency was expected, as it is a heating element what provides the energy for modification of the bulk heterojunction. However, microwave annealing still retains an edge as an on-demand solution for fast thermal annealing. A hotplate takes a long time to warm up to the target temperature if turning on from a cold start and it cannot be turned off for on demand heating. However, as this work showed, a microwave approach offers start up times in the order of seconds while consuming less electrical power than the hotplate.

3.6 Chapter summary

This chapter examined existing works on the application of microwave annealing to organic photovoltaic solar cells, identifying that contradictory claims exist with regard to which layer of the OPV absorbs radiation to induce thermal annealing. From the review of existing works, it is believed that although several groups have experimented with microwave annealing of P3HT:PCBM bulk heterojunctions, no group has applied this approach to all small-molecule blends and most recent publications have focused on the optimization of the transport layers. Additionally, few groups provide detailed accounts of their experimental configurations or optimization processes, in many cases, leaving the readers to figure out how to take advantage of microwave annealing and how to set up a microwave experiment.

This chapter examined different microwave annealing configurations to find one that led to uniform heating and reproducible results. A P3HT:PCBM blend was selected as a calibration material due to the dramatic changes in visual appearance observable as a function of annealing temperature. Once an adequate annealing configuration was found, a calibration ramp of microwave time vs temperature was measured to serve as reference during the annealing process.

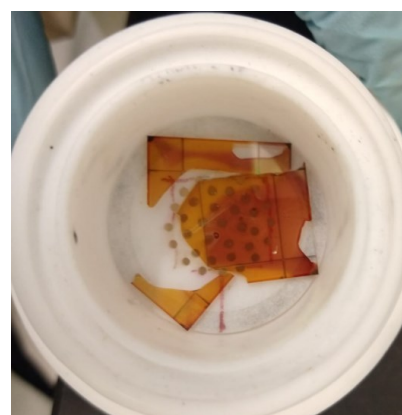
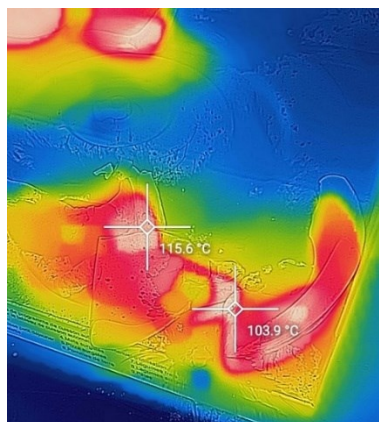
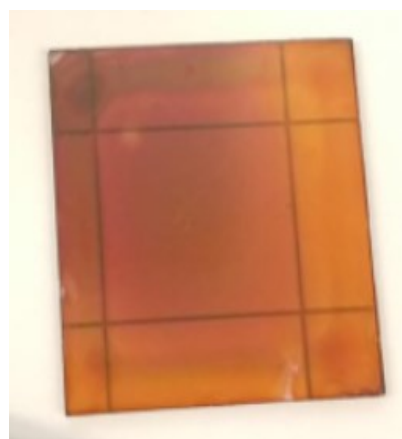
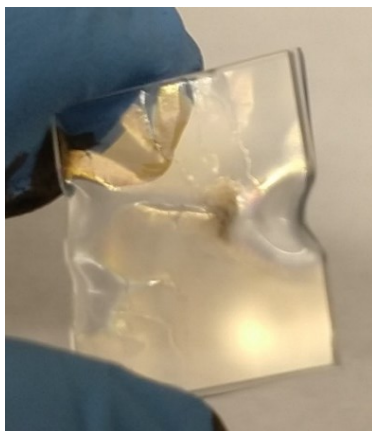
A ZR1:BTP-BO-4Cl blend was selected as an all-small molecule composition for optimization via microwaves. It was found that this bulk heterojunction is highly responsive to microwave annealing. A screening of different microwave times suggested that a microwave annealing time of 15 s (112 °C) led to a 4.6x increase in power conversion efficiency as compared to an unannealed sample. Moreover, little difference was seen between this annealing technique and an equivalent traditional hotplate approach.

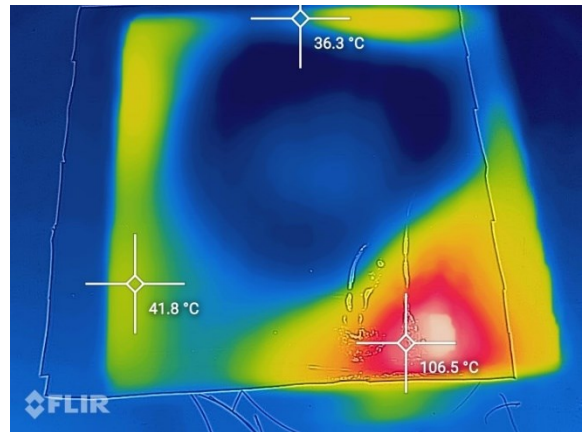
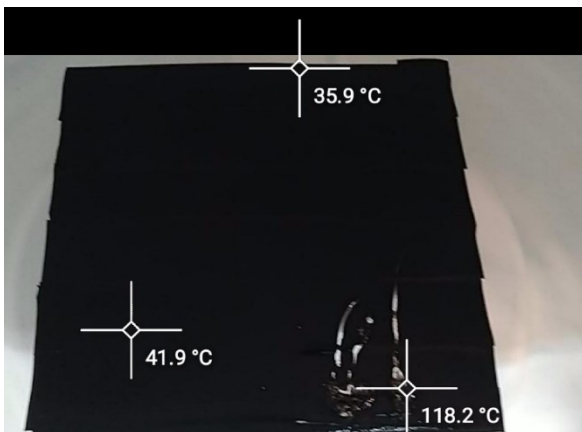
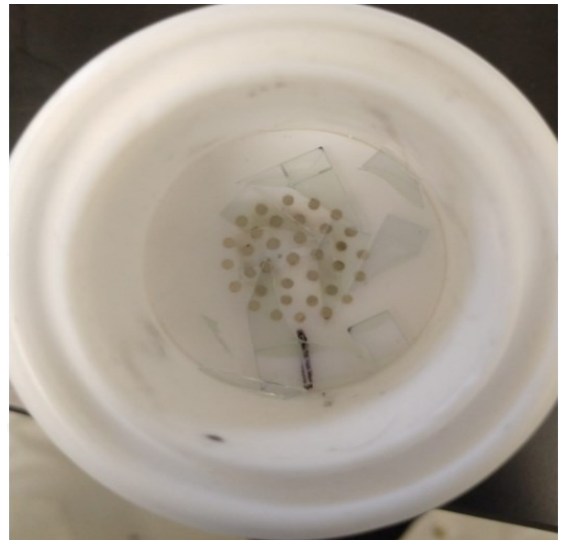
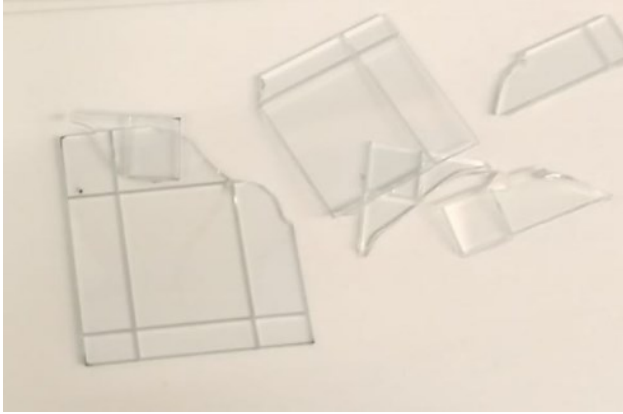
At a time when everyone must do their part to reduce carbon emissions, even small energy savings from multiple laboratory-scale experiments are important. Additionally, whereas a hotplate is a costly and “slow” scientific instrument, savings in the form of time and energy derived from adapting a household microwave for research would add up over the long term. For instance, the half-hour required for a hotplate to reach a target temperature is costly in terms of operator time and salary, and this cost is compounded over the length of a project (e.g. years of graduate research work). Moreover, this cost is multiplied if multiple users require the implementation of thermal annealing to optimize their solar cells. While there is a high initial effort to setup a

microwave annealing system, its advantages make it an attractive approach. In an industrial setting these savings may be even more substantial.

3.7 Gallery of Infamy

Microwave annealing can be a challenging process. Experimentalists should not be discouraged by initial failures. The following “Gallery of Infamy” has been included to motivate fellow scientists interested in the approach to remain persistent despite failure. In the scientific community, behind-the-scenes work often goes unnoticed and unpublished, causing some to believe they are alone in their difficulties or that “optimization” is a trivial process. These pictures are provided encouragement to those who experience failure and to illustrate possible worse-case scenarios that are not uncommon when performing initial calibrations of their microwave setup. With this reference, interested experimentalists will not be caught by surprise if they encounter similar problems during their calibrations.





Materials section

The PM6, BTP-BO-4Cl, PFN-Br materials were purchased from Solarmer Inc. The P3HT donor was purchased from Rieke Materials. The PC₆₁BM and PC₇₁BM acceptors were purchased from American Elements. PEDOT:PSS was purchased from Ossila. The ZR1 donor was purchased from 1-Material. All solvents were purchased from Sigma-Aldrich and Fischer and were used as received without further purification. ITO coated glass substrates were purchased from Delta Technologies (8-12 Ω /sq).

OPV device preparation

ITO-coated glass substrates were subjected to a wash cycle consisting of sequential sonication, as indicated:

- 1) Dichloromethane 10 min
- 2) Deionized water 10 min
- 3) Isopropanol 10 min

Afterwards, the substrates were dried under a nitrogen flow and placed in a Harrick plasma system (18 W) for air plasma cleaning at 1.0 torr for 10 minutes.

An amount of PEDOT:PSS was extracted from a storage bottle under refrigeration with a syringe and allowed to thaw for 15 min prior to spin-casting. The solution was filtered through a cellulose-membrane syringe filter (0.2 μ m pore) and four to five drops were dripped on the glass/ITO substrate for spin coating at 3000 rpm for 1 min (approximate thickness of 30 nm). Afterwards, 100 μ L of a bulk heterojunction ink was taken from a dissolution vial and spin coated to the target thickness.

In the case of the PM6:BTP-BO-4Cl film, the BHJ was allowed to dissolve in chlorobenzene at 120 °C. BHJ solution was prepared by mixing a donor:acceptor ratio of 1:1.2 w/w., tot. conc. of 17.6 mg/mL. A 2 mL, 5% v/v stock solution of DIO:CB was prepared immediately prior to

dissolution and added to the BHJ vial for a 0.5% v/v content of DIO 1-2 hours prior to spin-coating. No filtration was required during spin coating. Optimum spin speed was 800 rpm for 1 min (105-108 nm thick layer).

In the case of the ZR1:BTP-BP-4Cl film, the BHJ was allowed to dissolve in chloroform at 55 °C. BHJ solution was prepared by mixing a donor:acceptor ratio of 1:0.5 w/w., tot. conc. of 15 mg/mL. No additive was used. The BHJ solution was filtered through a PTFE filter (0.2 µm pore) prior to spin coating. Optimum spin speed was 2200 rpm for 30 s (110 nm thick layer).

In both cases, the donor and acceptor materials were sealed in an Ar-filled glove box and allowed to dissolve overnight.

Unless otherwise stated, thermal annealing occurred by placing the OPV substrate on a hotplate inside a nitrogen-filled glovebox for a specific amount of time.

Metal cathode was thermally evaporation onto the OPV chip by depositing a 0.8 nm layer of LiF, followed by a 20 nm layer of Al, and a 60 nm layer of Mg. Evaporation rates were 1.0 Å/s for LiF, and 2.0 Å/s for Al and 2.0 Mg. Solar devices had an approximate area of 10 mm² Note: PM6- and ZR1-based solar cells did not include a LiF layer.

DRCN5T:IT-4F cells were prepared following the same bulk heterojunction recipe reported by Kirkey at el. al. [99] with the difference that a conventional architecture was used: glass/ITO/PEDOT:PSS/DRCN5T:IT-4F. The PEDOT:PSS layer was 30 nm thick.

PPDT2FBT:PCBM cells were prepared according to the recipe reported by Mainville et al. [156]

Microwave section

The microwave Si elements in the Type I configuration were cut for an approximate area of 3 cm x 3 cm from a 1.5-5 Ω, boron-doped, P-type wafer. Heating element thickness was approximately 0.65 mm.

Microwave thermometer probe used was an Osensa 300-GEN controller PRB-G40-02M-ST-HC fiber optic sensor.

Instruments

Solar simulator was a G2V Pico LED instrument from G2V Optics using AM 1.5G light at 100 mW/cm².

The microwave used was a Panasonic NNST651B.

AFM characterization was performed in the tapping mode using a Digital Instruments/ Veeco Multimode unit. Data was processed using the Gwyddion software.

References

- [1] C. Duan and L. Ding, “The new era for organic solar cells: polymer donors,” *Science Bulletin*, vol. 65, no. 17, pp. 1422–1424, Sep. 2020, doi: 10.1016/j.scib.2020.04.044.
- [2] G2V Optics, “Sun Simulators: AM0-AM40 | AM1.5G Standards.” <https://g2voptics.com/solar-simulation/> (accessed Oct. 04, 2021).
- [3] NREL, “Best Research-Cell Efficiency Chart.” <https://www.nrel.gov/pv/cell-efficiency.html> (accessed Oct. 04, 2021).
- [4] H. Jinno *et al.*, “Stretchable and waterproof elastomer-coated organic photovoltaics for washable electronic textile applications,” *Nat Energy*, vol. 2, no. 10, pp. 780–785, Oct. 2017, doi: 10.1038/s41560-017-0001-3.
- [5] M. Riede, D. Spoltore, and K. Leo, “Organic Solar Cells—The Path to Commercial Success,” *Adv. Energy Mater.*, vol. 11, no. 1, p. 2002653, Jan. 2021, doi: 10.1002/aenm.202002653.
- [6] R. Søndergaard, M. Hösel, D. Angmo, T. T. Larsen-Olsen, and F. C. Krebs, “Roll-to-roll fabrication of polymer solar cells,” *Materials Today*, vol. 15, no. 1–2, pp. 36–49, Jan. 2012, doi: 10.1016/S1369-7021(12)70019-6.
- [7] Y. Wang and X. Zhan, “Layer-by-Layer Processed Organic Solar Cells,” *Adv. Energy Mater.*, vol. 6, no. 17, p. 1600414, Sep. 2016, doi: 10.1002/aenm.201600414.
- [8] A. Facchetti, “Polymer donor–polymer acceptor (all-polymer) solar cells,” *Materials Today*, vol. 16, no. 4, pp. 123–132, Apr. 2013, doi: 10.1016/j.mattod.2013.04.005.
- [9] X. Liu, B. P. Rand, and S. R. Forrest, “Engineering Charge-Transfer States for Efficient, Low-Energy-Loss Organic Photovoltaics,” *Trends in Chemistry*, vol. 1, no. 9, pp. 815–829, Dec. 2019, doi: 10.1016/j.trechm.2019.08.001.
- [10] M. Knupfer, “Exciton binding energies in organic semiconductors,” *Appl. Phys. A*, vol. 77, no. 5, pp. 623–626, Oct. 2003, doi: 10.1007/s00339-003-2182-9.
- [11] Y. Yin *et al.*, “Manipulating Polymer Donors Toward a High-Performance Polymer Acceptor Based On a Fused Perylenediimide Building Block With a Built-In Twisting Configuration,” *ACS Appl. Mater. Interfaces*, vol. 11, no. 33, pp. 29765–29772, Aug. 2019, doi: 10.1021/acsami.9b07067.

- [12] D. Xia *et al.*, “Fullerene as an additive for increasing the efficiency of organic solar cells to more than 17%,” *Journal of Colloid and Interface Science*, vol. 601, pp. 70–77, Nov. 2021, doi: 10.1016/j.jcis.2021.05.033.
- [13] R. Zhou *et al.*, “All-small-molecule organic solar cells with over 14% efficiency by optimizing hierarchical morphologies,” *Nat Commun*, vol. 10, no. 1, p. 5393, Dec. 2019, doi: 10.1038/s41467-019-13292-1.
- [14] R. K. Khisamov *et al.*, “Work function of chemical compounds of aluminum-magnesium system,” *IOP Conf. Ser.: Mater. Sci. Eng.*, vol. 1008, p. 012032, Jan. 2021, doi: 10.1088/1757-899X/1008/1/012032.
- [15] K. A. Mazzio and C. K. Luscombe, “The future of organic photovoltaics,” *Chem. Soc. Rev.*, vol. 44, no. 1, pp. 78–90, 2015, doi: 10.1039/C4CS00227J.
- [16] Q. Liu *et al.*, “18% Efficiency organic solar cells,” *Science Bulletin*, vol. 65, no. 4, pp. 272–275, Feb. 2020, doi: 10.1016/j.scib.2020.01.001.
- [17] R. Ma *et al.*, “Improving open-circuit voltage by a chlorinated polymer donor endows binary organic solar cells efficiencies over 17%,” *Sci. China Chem.*, vol. 63, no. 3, pp. 325–330, Mar. 2020, doi: 10.1007/s11426-019-9669-3.
- [18] X. Rodríguez-Martínez, E. Pascual-San-José, and M. Campoy-Quiles, “Accelerating organic solar cell material’s discovery: high-throughput screening and *big data*,” *Energy Environ. Sci.*, vol. 14, no. 6, pp. 3301–3322, 2021, doi: 10.1039/D1EE00559F.
- [19] N. G. An, J. Y. Kim, and D. Vak, “Machine learning-assisted development of organic photovoltaics *via* high-throughput *in situ* formulation,” *Energy Environ. Sci.*, vol. 14, no. 6, pp. 3438–3446, 2021, doi: 10.1039/D1EE00641J.
- [20] Ossila, “Spin Coating: Complete Guide to Theory and Techniques.” <https://www.ossila.com/pages/spin-coating> (accessed Oct. 10, 2021).
- [21] J. Min *et al.*, “Time-Dependent Morphology Evolution of Solution-Processed Small Molecule Solar Cells during Solvent Vapor Annealing,” *Adv. Energy Mater.*, vol. 6, no. 10, p. 1502579, May 2016, doi: 10.1002/aenm.201502579.
- [22] W. Köntges *et al.*, “Visualizing morphological principles for efficient photocurrent generation in organic non-fullerene acceptor blends,” *Energy Environ. Sci.*, vol. 13, no. 4, pp. 1259–1268, 2020, doi: 10.1039/C9EE03535D.

- [23] C. Jin, B. C. Olsen, E. J. Lubber, and J. M. Buriak, “Nanopatterning via Solvent Vapor Annealing of Block Copolymer Thin Films,” *Chem. Mater.*, vol. 29, no. 1, pp. 176–188, Jan. 2017, doi: 10.1021/acs.chemmater.6b02967.
- [24] R. Kroon *et al.*, “Thermoelectric plastics: from design to synthesis, processing and structure–property relationships,” *Chem Soc Rev*, p. 18, 2016, doi: 10.1039/C6CS00149A.
- [25] J. Rivnay *et al.*, “Structural control of mixed ionic and electronic transport in conducting polymers,” *Nat Commun*, vol. 7, no. 1, p. 11287, Sep. 2016, doi: 10.1038/ncomms11287.
- [26] D. Alemu, H.-Y. Wei, K.-C. Ho, and C.-W. Chu, “Highly conductive PEDOT:PSS electrode by simple film treatment with methanol for ITO-free polymer solar cells,” *Energy Environ. Sci.*, vol. 5, no. 11, p. 9662, 2012, doi: 10.1039/c2ee22595f.
- [27] K. Gilissen, W. Moons, J. Manca, and W. Deferme, “Microwave annealing as fast alternative for hotplate annealing of poly(3,4-ethylenedioxythiophene): Poly(styrenesulfonate),” in *2014 29th International Conference on Microelectronics Proceedings - MIEL 2014*, Belgrade, Serbia, May 2014, pp. 219–222. doi: 10.1109/MIEL.2014.6842126.
- [28] F. C. Krebs, T. Tromholt, and M. Jørgensen, “Upscaling of polymer solar cell fabrication using full roll-to-roll processing,” *Nanoscale*, vol. 2, no. 6, p. 873, 2010, doi: 10.1039/b9nr00430k.
- [29] United Nations Department of Economic and Social Affairs, “World Population Prospects 2019,” 2019. <https://population.un.org/wpp/Graphs/Probabilistic/POP/TOT/900> (accessed Oct. 04, 2021).
- [30] International Energy Agency, “World Energy Balances: Overview,” 2019. <https://www.iea.org/reports/world-energy-balances-overview/world> (accessed Oct. 04, 2021).
- [31] M. Höök and X. Tang, “Depletion of fossil fuels and anthropogenic climate change—A review,” *Energy Policy*, vol. 52, pp. 797–809, Jan. 2013, doi: 10.1016/j.enpol.2012.10.046.
- [32] Natural Resources Defense Council, “Fossil Fuels: The Dirty Facts.” <https://www.nrdc.org/stories/fossil-fuels-dirty-facts> (accessed Oct. 04, 2021).
- [33] K. Tam, “There’s more than enough solar power to meet our energy needs: the problem is storing it.” <https://www.ualberta.ca/folio/2018/04/theres-more-than-enough-solar-power-to-meet-our-energy-needs-the-problem-is-storing-it.html> (accessed Oct. 04, 2021).

- [34] C. Battaglia, A. Cuevas, and S. De Wolf, “High-efficiency crystalline silicon solar cells: status and perspectives,” *Energy Environ. Sci.*, vol. 9, no. 5, pp. 1552–1576, 2016, doi: 10.1039/C5EE03380B.
- [35] T. Sinha, D. Lilhare, and A. Khare, “A review on the improvement in performance of CdTe/CdS thin-film solar cells through optimization of structural parameters,” *J Mater Sci*, vol. 54, no. 19, pp. 12189–12205, Oct. 2019, doi: 10.1007/s10853-019-03651-0.
- [36] J. Ramanujam and U. P. Singh, “Copper indium gallium selenide based solar cells – a review,” *Energy Environ. Sci.*, vol. 10, no. 6, pp. 1306–1319, 2017, doi: 10.1039/C7EE00826K.
- [37] J. Y. Kim, J.-W. Lee, H. S. Jung, H. Shin, and N.-G. Park, “High-Efficiency Perovskite Solar Cells,” *Chem. Rev.*, vol. 120, no. 15, pp. 7867–7918, Aug. 2020, doi: 10.1021/acs.chemrev.0c00107.
- [38] M. Kokkonen *et al.*, “Advanced research trends in dye-sensitized solar cells,” *J. Mater. Chem. A*, vol. 9, no. 17, pp. 10527–10545, 2021, doi: 10.1039/D1TA00690H.
- [39] C. Yan *et al.*, “Non-fullerene acceptors for organic solar cells,” *Nat Rev Mater*, vol. 3, no. 3, p. 18003, Mar. 2018, doi: 10.1038/natrevmats.2018.3.
- [40] “Materials Used in Solar Cells,” Dec. 09, 2019. <https://g2voptics.com/photovoltaics-solar-cells/solar-cell-materials/> (accessed Oct. 09, 2021).
- [41] R. Søndergaard, M. Hösel, D. Angmo, T. T. Larsen-Olsen, and F. C. Krebs, “Roll-to-roll fabrication of polymer solar cells,” *Materials Today*, vol. 15, no. 1–2, pp. 36–49, Jan. 2012, doi: 10.1016/S1369-7021(12)70019-6.
- [42] N. Espinosa, M. Hösel, D. Angmo, and F. C. Krebs, “Solar cells with one-day energy payback for the factories of the future,” *Energy Environ. Sci.*, vol. 5, no. 1, pp. 5117–5132, 2012, doi: 10.1039/C1EE02728J.
- [43] Universiteit Hasselt, “Organic photovoltaic devices.” <https://www.uhasselt.be/UH/IMO/Research-domains/Energy/Organic-photovoltaic-devices.html> (accessed Oct. 09, 2021).
- [44] M. Kaltenbrunner *et al.*, “Ultrathin and lightweight organic solar cells with high flexibility,” *Nat Commun*, vol. 3, no. 1, p. 770, Jan. 2012, doi: 10.1038/ncomms1772.

- [45] C. Nocito and V. Koncar, “Flexible photovoltaic cells embedded into textile structures,” in *Smart Textiles and their Applications*, Elsevier, 2016, pp. 401–422. doi: 10.1016/B978-0-08-100574-3.00018-7.
- [46] A. Armin *et al.*, “A History and Perspective of Non-Fullerene Electron Acceptors for Organic Solar Cells,” *Adv. Energy Mater.*, vol. 11, no. 15, p. 2003570, Apr. 2021, doi: 10.1002/aenm.202003570.
- [47] NREL, “New Design Strategy Pushes Organic Photovoltaics Past 18% Efficiency.” <https://www.nrel.gov/news/program/2021/new-design-strategy-increases-organic-pv-efficiency.html> (accessed Oct. 09, 2021).
- [48] F. Liu *et al.*, “Organic Solar Cells with 18% Efficiency Enabled by an Alloy Acceptor: A Two-in-One Strategy,” *Adv. Mater.*, vol. 33, no. 27, p. 2100830, Jul. 2021, doi: 10.1002/adma.202100830.
- [49] Y. Zhou *et al.*, “Recyclable organic solar cells on cellulose nanocrystal substrates,” *Sci Rep*, vol. 3, no. 1, p. 1536, Dec. 2013, doi: 10.1038/srep01536.
- [50] M. Jahandar, S. Kim, and D. C. Lim, “Indoor Organic Photovoltaics for Self-Sustaining IoT Devices: Progress, Challenges and Practicalization,” *ChemSusChem*, vol. 14, no. 17, pp. 3449–3474, Sep. 2021, doi: 10.1002/cssc.202100981.
- [51] S. Lee, Y. Lee, J. Park, and D. Choi, “Stitchable organic photovoltaic cells with textile electrodes,” *Nano Energy*, vol. 9, pp. 88–93, Oct. 2014, doi: 10.1016/j.nanoen.2014.06.017.
- [52] K. Yu, S. Rich, S. Lee, K. Fukuda, T. Yokota, and T. Someya, “Organic Photovoltaics: Toward Self-Powered Wearable Electronics,” *Proc. IEEE*, vol. 107, no. 10, pp. 2137–2154, Oct. 2019, doi: 10.1109/JPROC.2019.2929797.
- [53] K. Forberich, F. Guo, C. Bronnbauer, and C. J. Brabec, “Efficiency Limits and Color of Semitransparent Organic Solar Cells for Application in Building-Integrated Photovoltaics,” *Energy Technology*, vol. 3, no. 10, pp. 1051–1058, Oct. 2015, doi: 10.1002/ente.201500131.
- [54] E. R. Rwenyagila, “A Review of Organic Photovoltaic Energy Source and Its Technological Designs,” *International Journal of Photoenergy*, vol. 2017, pp. 1–12, 2017, doi: 10.1155/2017/1656512.

- [55] R. Meitzner, U. S. Schubert, and H. Hoppe, “Agrivoltaics—The Perfect Fit for the Future of Organic Photovoltaics,” *Adv. Energy Mater.*, vol. 11, no. 1, p. 2002551, Jan. 2021, doi: 10.1002/aenm.202002551.
- [56] HDIAC, “Solar Photovoltaic Considerations for Operational and Warfighter Support Capabilities.” <https://hdiac.org/articles/solar-photovoltaic-considerations-for-operational-and-warfighter-support-capabilities-2/> (accessed Oct. 09, 2021).
- [57] Y. Yang, K. Mielczarek, M. Aryal, A. Zakhidov, and W. Hu, “Nanoimprinted Polymer Solar Cell,” *ACS Nano*, vol. 6, no. 4, pp. 2877–2892, Apr. 2012, doi: 10.1021/nn3001388.
- [58] H. K. Bisoyi and Q. Li, “Stimuli directed alignment of self-organized one-dimensional semiconducting columnar liquid crystal nanostructures for organic electronics,” *Progress in Materials Science*, vol. 104, pp. 1–52, Jul. 2019, doi: 10.1016/j.pmatsci.2019.03.005.
- [59] M. He, F. Qiu, and Z. Lin, “Conjugated rod–coil and rod–rod block copolymers for photovoltaic applications,” *J. Mater. Chem.*, vol. 21, no. 43, p. 17039, 2011, doi: 10.1039/c1jm11518a.
- [60] L. Huang *et al.*, “Unraveling the Morphology in Solution-Processed Pseudo-Bilayer Planar Heterojunction Organic Solar Cells,” *ACS Appl. Mater. Interfaces*, vol. 11, no. 29, pp. 26213–26221, Jul. 2019, doi: 10.1021/acsami.9b10689.
- [61] K. Jiang *et al.*, “Pseudo-bilayer architecture enables high-performance organic solar cells with enhanced exciton diffusion length,” *Nat Commun*, vol. 12, no. 1, p. 468, Dec. 2021, doi: 10.1038/s41467-020-20791-z.
- [62] K. Weng *et al.*, “Optimized active layer morphology toward efficient and polymer batch insensitive organic solar cells,” *Nat Commun*, vol. 11, no. 1, p. 2855, Dec. 2020, doi: 10.1038/s41467-020-16621-x.
- [63] Y. Yang, K. Mielczarek, A. Zakhidov, and W. Hu, “Large Molecular Weight Polymer Solar Cells with Strong Chain Alignment Created by Nanoimprint Lithography,” *ACS Appl. Mater. Interfaces*, vol. 8, no. 11, pp. 7300–7307, Mar. 2016, doi: 10.1021/acsami.6b00192.
- [64] H.-C. Liao, C.-C. Ho, C.-Y. Chang, M.-H. Jao, S. B. Darling, and W.-F. Su, “Additives for morphology control in high-efficiency organic solar cells,” *Materials Today*, vol. 16, no. 9, pp. 326–336, Sep. 2013, doi: 10.1016/j.mattod.2013.08.013.

- [65] C. J. Brabec, M. Heeney, I. McCulloch, and J. Nelson, "Influence of blend microstructure on bulk heterojunction organic photovoltaic performance," *Chem. Soc. Rev.*, vol. 40, no. 3, pp. 1185–1199, 2011, doi: 10.1039/C0CS00045K.
- [66] K. Anagnostou, M. M. Stylianakis, K. Petridis, and E. Kymakis, "Building an Organic Solar Cell: Fundamental Procedures for Device Fabrication," *Energies*, vol. 12, no. 11, p. 2188, Jun. 2019, doi: 10.3390/en12112188.
- [67] D. D. S. Fung and W. C. H. Choy, "Introduction to Organic Solar Cells," in *Organic Solar Cells*, W. C. H. Choy, Ed. London: Springer London, 2013, pp. 1–16. doi: 10.1007/978-1-4471-4823-4_1.
- [68] University of Washington, "Major Processes in Organic Solar Cells." http://depts.washington.edu/cmditr/modules/opv/major_processes_in_organic_solar_cells.html#:~:text=In%20organic%20semiconductors%20the%20%22exciton,for%20exciton%20dissociation%20to%20occur. (accessed Oct. 12, 2021).
- [69] Y. Wang and X. Zhan, "Layer-by-Layer Processed Organic Solar Cells," *Adv. Energy Mater.*, vol. 6, no. 17, p. 1600414, Sep. 2016, doi: 10.1002/aenm.201600414.
- [70] Y. Firdaus *et al.*, "Long-range exciton diffusion in molecular non-fullerene acceptors," *Nat Commun*, vol. 11, no. 1, p. 5220, Dec. 2020, doi: 10.1038/s41467-020-19029-9.
- [71] B. Jung, K. Kim, and W. Kim, "Microwave-assisted solvent vapor annealing to rapidly achieve enhanced performance of organic photovoltaics," *J. Mater. Chem. A*, vol. 2, no. 36, pp. 15175–15180, 2014, doi: 10.1039/C4TA02609H.
- [72] T. Fukuhara, Y. Tamai, and H. Ohkita, "Nongeminate charge recombination in organic photovoltaics," *Sustainable Energy Fuels*, vol. 4, no. 9, pp. 4321–4351, 2020, doi: 10.1039/D0SE00310G.
- [73] M. Rita Narayan and J. Singh, "Study of the mechanism and rate of exciton dissociation at the donor-acceptor interface in bulk-heterojunction organic solar cells," *Journal of Applied Physics*, vol. 114, no. 7, p. 073510, Aug. 2013, doi: 10.1063/1.4818813.
- [74] K. Nakano, K. Suzuki, Y. Chen, and K. Tajima, "Roles of Energy/Charge Cascades and Intermixed Layers at Donor/Acceptor Interfaces in Organic Solar Cells," *Sci Rep*, vol. 6, no. 1, p. 29529, Sep. 2016, doi: 10.1038/srep29529.
- [75] C. Deibel and V. Dyakonov, "Polymer–fullerene bulk heterojunction solar cells," *Rep. Prog. Phys.*, vol. 73, no. 9, p. 096401, Sep. 2010, doi: 10.1088/0034-4885/73/9/096401.

- [76] T. Kirchartz, T. Agostinelli, M. Campoy-Quiles, W. Gong, and J. Nelson, "Understanding the Thickness-Dependent Performance of Organic Bulk Heterojunction Solar Cells: The Influence of Mobility, Lifetime, and Space Charge," *J. Phys. Chem. Lett.*, vol. 3, no. 23, pp. 3470–3475, Dec. 2012, doi: 10.1021/jz301639y.
- [77] C. Groves, J. C. Blakesley, and N. C. Greenham, "Effect of Charge Trapping on Geminate Recombination and Polymer Solar Cell Performance," *Nano Lett.*, vol. 10, no. 3, pp. 1063–1069, Mar. 2010, doi: 10.1021/nl100080r.
- [78] R. Sorrentino, E. Kozma, S. Luzzati, and R. Po, "Interlayers for non-fullerene based polymer solar cells: distinctive features and challenges," *Energy Environ. Sci.*, vol. 14, no. 1, pp. 180–223, 2021, doi: 10.1039/D0EE02503H.
- [79] E. Bundgaard and F. Krebs, "Low band gap polymers for organic photovoltaics," *Solar Energy Materials and Solar Cells*, vol. 91, no. 11, pp. 954–985, Jul. 2007, doi: 10.1016/j.solmat.2007.01.015.
- [80] S. Li, C.-Z. Li, M. Shi, and H. Chen, "New Phase for Organic Solar Cell Research: Emergence of Y-Series Electron Acceptors and Their Perspectives," *ACS Energy Lett.*, vol. 5, no. 5, pp. 1554–1567, May 2020, doi: 10.1021/acseenergylett.0c00537.
- [81] C. Yan *et al.*, "Non-fullerene acceptors for organic solar cells," *Nat Rev Mater*, vol. 3, no. 3, p. 18003, Mar. 2018, doi: 10.1038/natrevmats.2018.3.
- [82] Q. Zhao, J. Qu, and F. He, "Chlorination: An Effective Strategy for High-Performance Organic Solar Cells," *Adv. Sci.*, vol. 7, no. 14, p. 2000509, Jul. 2020, doi: 10.1002/advs.202000509.
- [83] B. Lu *et al.*, "Recent progress of Y-series electron acceptors for organic solar cells," *Nano Select*, p. nano.202100036, May 2021, doi: 10.1002/nano.202100036.
- [84] B. Zheng, L. Huo, and Y. Li, "Benzodithiophenedione-based polymers: recent advances in organic photovoltaics," *NPG Asia Mater*, vol. 12, no. 1, p. 3, Dec. 2020, doi: 10.1038/s41427-019-0163-5.
- [85] S. Li *et al.*, "Unveiling structure-performance relationships from multi-scales in non-fullerene organic photovoltaics," *Nat Commun*, vol. 12, no. 1, p. 4627, Dec. 2021, doi: 10.1038/s41467-021-24937-5.

- [86] Y. Cui *et al.*, “Single-Junction Organic Photovoltaic Cells with Approaching 18% Efficiency,” *Adv. Mater.*, vol. 32, no. 19, p. 1908205, May 2020, doi: 10.1002/adma.201908205.
- [87] Technical University of Denmark, “Synthesis - Materials in Solar Cells,” *Coursera*. <https://www.coursera.org/lecture/solar-cell/synthesis-U9Ht2> (accessed Oct. 10, 2021).
- [88] X. Xu, L. Yu, H. Yan, R. Li, and Q. Peng, “Highly efficient non-fullerene organic solar cells enabled by a delayed processing method using a non-halogenated solvent,” *Energy Environ. Sci.*, vol. 13, no. 11, pp. 4381–4388, 2020, doi: 10.1039/D0EE02034F.
- [89] P. Chao *et al.*, “A Benzo[1,2-*b*:4,5-*c'*]Dithiophene-4,8-Dione-Based Polymer Donor Achieving an Efficiency Over 16%,” *Adv. Mater.*, vol. 32, no. 10, p. 1907059, Mar. 2020, doi: 10.1002/adma.201907059.
- [90] H. Sun *et al.*, “A monothiophene unit incorporating both fluoro and ester substitution enabling high-performance donor polymers for non-fullerene solar cells with 16.4% efficiency,” *Energy Environ. Sci.*, vol. 12, no. 11, pp. 3328–3337, 2019, doi: 10.1039/C9EE01890E.
- [91] L. Hong *et al.*, “Eco-Compatible Solvent-Processed Organic Photovoltaic Cells with Over 16% Efficiency,” *Adv. Mater.*, vol. 31, no. 39, p. 1903441, Sep. 2019, doi: 10.1002/adma.201903441.
- [92] B. Fan *et al.*, “Achieving over 16% efficiency for single-junction organic solar cells,” *Sci. China Chem.*, vol. 62, no. 6, pp. 746–752, Jun. 2019, doi: 10.1007/s11426-019-9457-5.
- [93] J. Xiong *et al.*, “Thiolactone copolymer donor gifts organic solar cells a 16.72% efficiency,” *Science Bulletin*, vol. 64, no. 21, pp. 1573–1576, Nov. 2019, doi: 10.1016/j.scib.2019.10.002.
- [94] Y. Wu *et al.*, “Rationally pairing photoactive materials for high-performance polymer solar cells with efficiency of 16.53%,” *Sci. China Chem.*, vol. 63, no. 2, pp. 265–271, Feb. 2020, doi: 10.1007/s11426-019-9599-1.
- [95] C. Sun *et al.*, “High Efficiency Polymer Solar Cells with Efficient Hole Transfer at Zero Highest Occupied Molecular Orbital Offset between Methylated Polymer Donor and Brominated Acceptor,” *J. Am. Chem. Soc.*, vol. 142, no. 3, pp. 1465–1474, Jan. 2020, doi: 10.1021/jacs.9b09939.

- [96] M. Lee, “Insights from Machine Learning Techniques for Predicting the Efficiency of Fullerene Derivatives-Based Ternary Organic Solar Cells at Ternary Blend Design,” *Adv. Energy Mater.*, p. 1900891, Jun. 2019, doi: 10.1002/aenm.201900891.
- [97] W. Sun *et al.*, “Machine learning–assisted molecular design and efficiency prediction for high-performance organic photovoltaic materials,” *Sci Adv*, vol. 5, no. 11, p. eaay4275, Nov. 2019, doi: 10.1126/sciadv.aay4275.
- [98] B. P. MacLeod *et al.*, “Self-driving laboratory for accelerated discovery of thin-film materials,” *Sci. Adv.*, vol. 6, no. 20, p. eaaz8867, May 2020, doi: 10.1126/sciadv.aaz8867.
- [99] A. Kirkey, E. J. Lubber, B. Cao, B. C. Olsen, and J. M. Buriak, “Optimization of the Bulk Heterojunction of All-Small-Molecule Organic Photovoltaics Using Design of Experiment and Machine Learning Approaches,” *ACS Appl. Mater. Interfaces*, vol. 12, no. 49, pp. 54596–54607, Dec. 2020, doi: 10.1021/acsami.0c14922.
- [100] B. Cao *et al.*, “How To Optimize Materials and Devices *via* Design of Experiments and Machine Learning: Demonstration Using Organic Photovoltaics,” *ACS Nano*, vol. 12, no. 8, pp. 7434–7444, Aug. 2018, doi: 10.1021/acsnano.8b04726.
- [101] Y. Mouhamad, P. Mokarian-Tabari, N. Clarke, R. A. L. Jones, and M. Geoghegan, “Dynamics of polymer film formation during spin coating,” *Journal of Applied Physics*, vol. 116, no. 12, p. 123513, Sep. 2014, doi: 10.1063/1.4896674.
- [102] D. K. Mohamad, J. Griffin, C. Bracher, A. T. Barrows, and D. G. Lidzey, “Spray-Cast Multilayer Organometal Perovskite Solar Cells Fabricated in Air,” *Adv. Energy Mater.*, vol. 6, no. 22, p. 1600994, Nov. 2016, doi: 10.1002/aenm.201600994.
- [103] Y. Cui *et al.*, “Over 16% efficiency organic photovoltaic cells enabled by a chlorinated acceptor with increased open-circuit voltages,” *Nat Commun*, vol. 10, no. 1, p. 2515, Dec. 2019, doi: 10.1038/s41467-019-10351-5.
- [104] A. J. Pearson *et al.*, “Rationalizing Phase Transitions with Thermal Annealing Temperatures for P3HT:PCBM Organic Photovoltaic Devices,” *Macromolecules*, vol. 45, no. 3, pp. 1499–1508, Feb. 2012, doi: 10.1021/ma202063k.
- [105] H. Zhang, Y. Li, X. Zhang, Y. Zhang, and H. Zhou, “Role of interface properties in organic solar cells: from substrate engineering to bulk-heterojunction interfacial morphology,” *Mater. Chem. Front.*, vol. 4, no. 10, pp. 2863–2880, 2020, doi: 10.1039/D0QM00398K.

- [106] S. Lan, X. Wu, G. Zhang, G. Chen, H. Chen, and T. Guo, “Improvement of Device Performance of Organic Photovoltaics via Laser Irradiation,” *J. Phys. Chem. C*, vol. 123, no. 36, pp. 22058–22065, Sep. 2019, doi: 10.1021/acs.jpcc.9b06707.
- [107] A. Solanki *et al.*, “Effectiveness of External Electric Field Treatment of Conjugated Polymers in Bulk-Heterojunction Solar Cells,” *ACS Appl. Mater. Interfaces*, vol. 8, no. 47, pp. 32282–32291, Nov. 2016, doi: 10.1021/acsami.6b08012.
- [108] H. K. Bisoyi and Q. Li, “Stimuli directed alignment of self-organized one-dimensional semiconducting columnar liquid crystal nanostructures for organic electronics,” *Progress in Materials Science*, vol. 104, pp. 1–52, Jul. 2019, doi: 10.1016/j.pmatsci.2019.03.005.
- [109] S. Park, Y.-S. Seo, W. S. Shin, S.-J. Moon, and J. Hwang, “Rapid and Checkable Electrical Post-Treatment Method for Organic Photovoltaic Devices,” *Sci Rep*, vol. 6, no. 1, p. 22604, Mar. 2016, doi: 10.1038/srep22604.
- [110] D. Zomerman, J. Kong, S. M. McAfee, G. C. Welch, and T. L. Kelly, “Control and Characterization of Organic Solar Cell Morphology Through Variable-Pressure Solvent Vapor Annealing,” *ACS Appl. Energy Mater.*, p. aesaem.8b01214, Sep. 2018, doi: 10.1021/acsaelm.8b01214.
- [111] H. Flügge *et al.*, “Microwave annealing of polymer solar cells with various transparent anode materials,” *Appl. Phys. Lett.*, vol. 97, no. 12, p. 123306, Sep. 2010, doi: 10.1063/1.3491213.
- [112] Y. Yan, J. Huang, and B. Z. Tang, “Kinetic trapping – a strategy for directing the self-assembly of unique functional nanostructures,” *Chem. Commun.*, vol. 52, no. 80, pp. 11870–11884, 2016, doi: 10.1039/C6CC03620A.
- [113] Z. Wang *et al.*, “The coupling and competition of crystallization and phase separation, correlating thermodynamics and kinetics in OPV morphology and performances,” *Nat Commun*, vol. 12, no. 1, p. 332, Dec. 2021, doi: 10.1038/s41467-020-20515-3.
- [114] J. Min *et al.*, “Time-Dependent Morphology Evolution of Solution-Processed Small Molecule Solar Cells during Solvent Vapor Annealing,” *Adv. Energy Mater.*, vol. 6, no. 10, p. 1502579, May 2016, doi: 10.1002/aenm.201502579.
- [115] J. Zhao, C. Yao, M. U. Ali, J. Miao, and H. Meng, “Recent advances in high-performance organic solar cells enabled by acceptor–donor–acceptor–donor–acceptor (A–DA'D–A) type

- acceptors,” *Mater. Chem. Front.*, vol. 4, no. 12, pp. 3487–3504, 2020, doi: 10.1039/D0QM00305K.
- [116] L. Ye *et al.*, “Ferrocene as a highly volatile solid additive in non-fullerene organic solar cells with enhanced photovoltaic performance,” *Energy Environ. Sci.*, vol. 13, no. 12, pp. 5117–5125, 2020, doi: 10.1039/D0EE02426K.
- [117] M.-A. Pan *et al.*, “16.7%-efficiency ternary blended organic photovoltaic cells with PCBM as the acceptor additive to increase the open-circuit voltage and phase purity,” *J. Mater. Chem. A*, vol. 7, no. 36, pp. 20713–20722, 2019, doi: 10.1039/C9TA06929A.
- [118] X. Wang *et al.*, “Recent Progress of Organic Photovoltaics with Efficiency over 17%,” *Energies*, vol. 14, no. 14, p. 4200, Jul. 2021, doi: 10.3390/en14144200.
- [119] L. Ma *et al.*, “High-Efficiency Nonfullerene Organic Solar Cells Enabled by 1000 nm Thick Active Layers with a Low Trap-State Density,” *ACS Appl. Mater. Interfaces*, vol. 12, no. 16, pp. 18777–18784, Apr. 2020, doi: 10.1021/acsami.0c05172.
- [120] N. K. Elumalai and A. Uddin, “Open circuit voltage of organic solar cells: an in-depth review,” *Energy Environ. Sci.*, vol. 9, no. 2, pp. 391–410, 2016, doi: 10.1039/C5EE02871J.
- [121] T. Agostinelli *et al.*, “Real-Time Investigation of Crystallization and Phase-Segregation Dynamics in P3HT:PCBM Solar Cells During Thermal Annealing,” *Adv. Funct. Mater.*, vol. 21, no. 9, pp. 1701–1708, May 2011, doi: 10.1002/adfm.201002076.
- [122] P. G. Karagiannidis, D. Georgiou, C. Pitsalidis, A. Laskarakis, and S. Logothetidis, “Evolution of vertical phase separation in P3HT:PCBM thin films induced by thermal annealing,” *Materials Chemistry and Physics*, vol. 129, no. 3, pp. 1207–1213, Oct. 2011, doi: 10.1016/j.matchemphys.2011.06.007.
- [123] S. Zhang, L. Ye, H. Zhang, and J. Hou, “Green-solvent-processable organic solar cells,” *Materials Today*, vol. 19, no. 9, pp. 533–543, Nov. 2016, doi: 10.1016/j.mattod.2016.02.019.
- [124] P.-K. Shin, P. Kumar, A. Kumar, S. Kannappan, and S. Ochiai, “Effects of Organic Solvents for Composite Active Layer of PCDTBT/PC₇₁BM on Characteristics of Organic Solar Cell Devices,” *International Journal of Photoenergy*, vol. 2014, pp. 1–8, 2014, doi: 10.1155/2014/786468.

- [125] N. C. S. Vieira, E. G. R. Fernandes, A. A. A. de Queiroz, F. E. G. Guimarães, and V. Zucolotto, “Indium tin oxide synthesized by a low cost route as SEG-FET pH sensor,” *Mat. Res.*, vol. 16, no. 5, pp. 1156–1160, Jul. 2013, doi: 10.1590/S1516-14392013005000101.
- [126] B. W. N. H. Hemasiri, J.-K. Kim, and J.-M. Lee, “Fabrication of highly conductive graphene/ITO transparent bi-film through CVD and organic additives-free sol-gel techniques,” *Sci Rep*, vol. 7, no. 1, p. 17868, Dec. 2017, doi: 10.1038/s41598-017-18063-w.
- [127] J. H. Yeom, S. Park, J. Kim, S. Rhee, and J.-W. Yu, “Rapid processing for organic photovoltaic devices,” *Macromol. Res.*, vol. 24, no. 10, pp. 881–886, Oct. 2016, doi: 10.1007/s13233-016-4123-4.
- [128] K. Zhang, Z. Hu, C. Duan, L. Ying, F. Huang, and Y. Cao, “The effect of methanol treatment on the performance of polymer solar cells,” *Nanotechnology*, vol. 24, no. 48, p. 484003, Dec. 2013, doi: 10.1088/0957-4484/24/48/484003.
- [129] C. Song *et al.*, “The effect of solvent treatment on the buried PEDOT:PSS layer,” *Organic Electronics*, vol. 43, pp. 9–14, Apr. 2017, doi: 10.1016/j.orgel.2016.12.057.
- [130] A. Aghassi and C. D. Fay, “Effects of IPA treatment on the photovoltaic performance of bulk heterojunction organic solar cells,” *Journal of Physics and Chemistry of Solids*, vol. 130, pp. 136–143, Jul. 2019, doi: 10.1016/j.jpics.2019.02.025.
- [131] D. Adam, “Out of the kitchen,” *Nature*, vol. 421, no. 6923, pp. 571–572, Feb. 2003, doi: 10.1038/421571a.
- [132] J. Sun, W. Wang, and Q. Yue, “Review on Microwave-Matter Interaction Fundamentals and Efficient Microwave-Associated Heating Strategies,” *Materials*, vol. 9, no. 4, p. 231, Mar. 2016, doi: 10.3390/ma9040231.
- [133] A. Kumar, Y. Kuang, Z. Liang, and X. Sun, “Microwave chemistry, recent advancements, and eco-friendly microwave-assisted synthesis of nanoarchitectures and their applications: a review,” *Materials Today Nano*, vol. 11, p. 100076, Aug. 2020, doi: 10.1016/j.mtnano.2020.100076.
- [134] K. Gilissen, J. Stryckers, W. Moons, J. Manca, and W. Deferme, “Microwave annealing, a promising step in the roll-to-roll processing of organic electronics,” *Facta Univ Electron Energ*, vol. 28, no. 1, pp. 143–151, 2015, doi: 10.2298/FUEE1501143G.

- [135] C. Jin, J. N. Murphy, K. D. Harris, and J. M. Buriak, “Deconvoluting the Mechanism of Microwave Annealing of Block Copolymer Thin Films,” *ACS Nano*, vol. 8, no. 4, pp. 3979–3991, Apr. 2014, doi: 10.1021/nm5009098.
- [136] P. Zhao *et al.*, “Effect of Temperature and Microwave Power Levels on Microwave Drying Kinetics of Zhaotong Lignite,” *Processes*, vol. 7, no. 2, p. 74, Feb. 2019, doi: 10.3390/pr7020074.
- [137] M. Vollmer, “Physics of the microwave oven,” *Phys. Educ.*, vol. 39, no. 1, pp. 74–81, Jan. 2004, doi: 10.1088/0031-9120/39/1/006.
- [138] CEM Corporation, “Introduction to Microwave Heating.” Accessed: Oct. 10, 2021. [Online]. Available: http://cem.com/media/contenttype/media/literature/525_ApNote_Disc_Teach_GEN1.pdf
- [139] Q. Cao *et al.*, “Fast and Controllable Crystallization of Perovskite Films by Microwave Irradiation Process,” *ACS Appl. Mater. Interfaces*, vol. 8, no. 12, pp. 7854–7861, Mar. 2016, doi: 10.1021/acsami.6b01558.
- [140] C.-J. Ko, Y.-K. Lin, and F.-C. Chen, “Microwave Annealing of Polymer Photovoltaic Devices,” *Adv. Mater.*, vol. 19, no. 21, pp. 3520–3523, Nov. 2007, doi: 10.1002/adma.200700741.
- [141] O. Yoshikawa, T. Sonobe, T. Sagawa, and S. Yoshikawa, “Single mode microwave irradiation to improve the efficiency of polymer solar cell based on poly(3-hexylthiophene) and fullerene derivative,” *Appl. Phys. Lett.*, vol. 94, no. 8, p. 083301, Feb. 2009, doi: 10.1063/1.3077612.
- [142] B. Kim, K. K. Lee, S. K. Lee, and E. H. Lim, “Improved Photovoltaic Efficiency of Polymer Photovoltaic Cells by Microwave Irradiation,” *MSF*, vol. 663–665, pp. 819–822, Nov. 2010, doi: 10.4028/www.scientific.net/MSF.663-665.819.
- [143] Z. Li *et al.*, “Performance enhancement of fullerene-based solar cells by light processing,” *Nat Commun*, vol. 4, no. 1, p. 2227, Oct. 2013, doi: 10.1038/ncomms3227.
- [144] P. G. Karagiannidis, D. Georgiou, C. Pitsalidis, A. Laskarakis, and S. Logothetidis, “Evolution of vertical phase separation in P3HT:PCBM thin films induced by thermal annealing,” *Materials Chemistry and Physics*, vol. 129, no. 3, pp. 1207–1213, Oct. 2011, doi: 10.1016/j.matchemphys.2011.06.007.

- [145] J. H. Yeom, M. Kim, S. Rhee, and J.-W. Yu, “A study of the effects of drying and sintering on the performance of organic photovoltaic devices,” *Solar Energy Materials and Solar Cells*, vol. 125, pp. 72–77, Jun. 2014, doi: 10.1016/j.solmat.2014.02.030.
- [146] M. Vasilopoulou, A. Soultati, P. Argitis, T. Stergiopoulos, and D. Davazoglou, “Fast Recovery of the High Work Function of Tungsten and Molybdenum Oxides via Microwave Exposure for Efficient Organic Photovoltaics,” *J. Phys. Chem. Lett.*, vol. 5, no. 11, pp. 1871–1879, Jun. 2014, doi: 10.1021/jz500612p.
- [147] A. Soultati, E. Polydorou, L. C. Palilis, P. Argitis, and M. Vasilopoulou, “Influence of microwave exposure of tungsten oxide hole extraction layers on nanomorphology, optical and electrical properties of organic photovoltaics,” in *2015 17th International Conference on Transparent Optical Networks (ICTON)*, Budapest, Jul. 2015, pp. 1–4. doi: 10.1109/ICTON.2015.7193674.
- [148] A. Soultati *et al.*, “Dehydration of molybdenum oxide hole extraction layers via microwave annealing for the improvement of efficiency and lifetime in organic solar cells,” *J. Mater. Chem. C*, vol. 4, no. 32, pp. 7683–7694, 2016, doi: 10.1039/C6TC02259F.
- [149] A. Soultati *et al.*, “Microwave exposure as a fast and cost-effective alternative of oxygen plasma treatment of indium-tin oxide electrode for application in organic solar cells,” *J. Phys. D: Appl. Phys.*, vol. 50, no. 50, p. 505105, Dec. 2017, doi: 10.1088/1361-6463/aa946c.
- [150] J.-W. Shin and W.-J. Cho, “Microwave Annealing Effects of Indium-Tin-Oxide Thin Films: Comparison with Conventional Annealing Methods,” *Phys. Status Solidi A*, vol. 215, no. 20, p. 1700975, Oct. 2018, doi: 10.1002/pssa.201700975.
- [151] X. Huang, L. Lv, Y. Hu, Z. Lou, Y. Hou, and F. Teng, “Enhanced performance in inverted polymer solar cells employing microwave-annealed sol-gel ZnO as electron transport layers,” *Organic Electronics*, vol. 42, pp. 107–114, Mar. 2017, doi: 10.1016/j.orgel.2016.12.031.
- [152] L. Duan and A. Uddin, “Progress in Stability of Organic Solar Cells,” *Adv. Sci.*, vol. 7, no. 11, p. 1903259, Jun. 2020, doi: 10.1002/advs.201903259.
- [153] Q. Burlingame, M. Ball, and Y.-L. Loo, “It’s time to focus on organic solar cell stability,” *Nat Energy*, vol. 5, no. 12, pp. 947–949, Dec. 2020, doi: 10.1038/s41560-020-00732-2.

- [154] S. Li *et al.*, “Unveiling structure-performance relationships from multi-scales in non-fullerene organic photovoltaics,” *Nat Commun*, vol. 12, no. 1, p. 4627, Dec. 2021, doi: 10.1038/s41467-021-24937-5.
- [155] PV Education, “Shunt Resistance.” <https://www.pveducation.org/pvcdrom/solar-cell-operation/shunt-resistance> (accessed Oct. 11, 2021).
- [156] M. Mainville *et al.*, “Water Compatible Direct (Hetero)arylation Polymerization of PPDT2FBT: A Pathway Towards Large-Scale Production of Organic Solar Cells,” *Asian J. Org. Chem.*, vol. 9, no. 9, pp. 1318–1325, Sep. 2020, doi: 10.1002/ajoc.202000231.